Check for updates

steel research international

steel research international

RESEARCH ARTICLE OPEN ACCESS

Influences of Cleanliness, Carbide Size, Hardness, and Residual Stresses on Long-Life Fatigue Strength and Crack-Initiation Mechanisms in Carbide-Rich Cold-Work Tool Steels Using Normalized S–N Curves and Database-Driven Validation of Murakami's √Area Model

Lennart Mirko Scholl | Frederik Tegeder | Dhirendar Chauhan | Bengt Hallstedt | Tobias Hajeck | Alexander Bezold | Christoph Broeckmann

Chair and Institute for Materials Applications in Mechanical Engineering (IWM), RWTH Aachen University, Aachen, Germany

Correspondence: Lennart Mirko Scholl (L.Scholl@iwm.rwth-aachen.de)

Received: 22 September 2025 | **Revised:** 11 June 2026 | **Accepted:** 23 June 2026

Keywords: √area fatigue-limit model | carbide-rich cold-work tool steels | fabrication- and finishing-induced residual stresses | long-life fatigue and crack-initiation mechanisms | normalized S–N curves | statistical fracture-surface analysis | steel cleanliness and hardness

ABSTRACT

Wear-resistant, carbide-rich cold-work tool steels are widely used in massive cold-forming, where tool life is limited by wear and fatigue. Yet the coupled influences of steelmaking route (cleanliness/carbide structure), heat treatment (hardness), and surface integrity on long-life fatigue (LLF) strength at $N_G = 10^7$ cycles remain insufficiently quantified for conventionally manufactured (non-AM) grades. Rotating-bending tests ($R = -1$) were performed at four to five application-relevant hardness levels on AISI D2 and AISI A11 (V10) produced by ingot casting + hot working (IC + HW) or gas-atomized powder metallurgy consolidated by hot isostatic pressing + hot working (PM-HIP + HW). For AISI A11, process cleanliness was systematically varied, yielding three different microstructural conditions with increasing cleanliness: V10 PM-L[1], V10 PM-L[2], and V10 PM-L[3]. Statistical fracture-surface analysis links fatigue strength to intrinsic defects (carbides, nonmetallic inclusions, and agglomerates) via extreme-value √area statistics and enables database-driven assessment of Murakami's √area framework using normalized S–N curves. Fatigue strength increases with hardness only when defect extremes are sufficiently small; strengths ≥ 1,000 MPa under rotating-bending require $\sqrt{area}_{max} \leq 60\,\mu m$, and further gains require $\sqrt{area}_{max} \leq 20\,\mu m$. Fabrication- and finishing-induced compressive residual stresses produce surface-shielding effects that shift normalized run-out data upward and can attenuate or mask the reverse hardness effect (RHE). Conversely, downward shifts for some fractures are consistent with defect-size-controlled RHE behavior that is intentionally not captured by the basic √area model.

1 | Introduction and Literature Review

Extending tool life and increasing output per tool—while minimizing changeover and maintenance time—are central to resource- and energy-efficient part production and high operational reliability [1, 2]. Low-emission, resource-efficient manufacturing chains are essential for reducing industrial carbon footprints [1, 2]. Accordingly, improving productivity in forming processes such as massive cold-forming, which can compete with advanced machining operations, is advantageous for both industry and society from economic and ecological perspectives. Carbide-rich, high-alloy cold-work tool steels (CWS) are

This is an open access article under the terms of the Creative Commons Attribution License, which permits use, distribution and reproduction in any medium, provided the original work is properly cited.

© 2026 The Author(s). *steel research international* published by Wiley-VCH GmbH.

widely used in massive cold-forming as pressing, stamping, rolling, deep drawing, cutting, and extrusion tools.

Tool performance and service life are primarily governed by wear resistance and fatigue strength [2–14]. Wear-induced loss of dimensional accuracy can often be mitigated by several regrinding/overhaul steps, whereas macroscopic fatigue fractures frequently preclude economical tool refurbishment and require replacement with new tools. In industrial tooling practice, unexpected fatigue-related failures interrupt production, cause machine downtime, increase costs, and reduce operational reliability [2, 3, 6–14]. As reported by Jung [11], Reiss [12], and Jesner [14], cold-work tooling typically contributes ∼5%–20% of part costs, depending on the process, tool geometry, and material. Consequently, high and unpredictable scatter in service life and limited production reliability under cost pressure remain major concerns—particularly where tool failure is governed by fatigue rather than gradual wear alone [2, 3, 6–14]. For example, Krishnadev et al. [3] concluded that the higher price of premium CWS can be justified by superior microstructure and service performance; moreover, it has been suggested that doubling the tool-material cost can be compensated by a mere 10% increase in production, whereas a 40% increase in tool life is sufficient to justify a higher-performance material with fivefold initial cost [3].

In addition to conventional cold-work toolmaking, additive manufacturing (AM) and hybrid manufacturing (HM) approaches—including AM with powder additivation—are increasingly used for several cold- and hot-work tooling applications (e.g., tool repair/overhaul, performance enhancement via increased carbide content, optimized geometries, and/or improvements of internal cooling), as well as to improve process productivity, reliability, and sustainability [1, 15–26]. HM combines conventional toolmaking, modern machining, and AM toolmaking, for example, by using conventionally manufactured base bodies onto which additively manufactured functional zones are built and finish-machined [1, 15–18, 25]. In this way, key advantages of AM (e.g., design freedom, tailored powder blends, and in-process alloying) can be leveraged without additively manufacturing the entire tool volume, thereby reducing costs and lead time [1, 15–18, 25].

These AM/HM routes are of growing interest not only for hot-work tool steels, but also for carbide-rich CWS and abrasive-wear-dominated applications; however, as reported by several authors [1, 15–41], they still face major challenges in processability (cold- and hot-cracking tendencies), AM-induced defect populations, thermal gradients, distortion and residual stresses (RS), mechanical strength level, microstructural and property homogeneity, as-built surface condition, and overall process costs.

In recent years, accelerated and cost-efficient experimental fatigue testing approaches, which are based on calorimetric methods, electrical resistance or acoustic emission measurements as damage indicators, have been proposed, applied to several metallic materials and are under further development by several authors [42–56]. These accelerated methods quantify changes in temperature, electrical resistance, or strain response during fatigue testing in order to detect damage evolution in real time and predict linear or nonlinear damage accumulation. As a long-term goal in cold-work tooling, such approaches may enable in situ tracking of tool damage states via in-process monitoring of damage accumulation under cyclic service loading, thereby supporting intervention before macroscopic fatigue failure occurs. For example, Gertlowski et al. [56] have recently developed and successfully applied an accelerated testing approach for carbide-rich, high-alloy high-speed steels (HSS) in the high-cycle fatigue (HCF) regime.

However, factors influencing fatigue and crack-initiating mechanisms remain insufficiently understood even for conventionally fabricated carbide-rich CWS. From a scientific perspective, two key limitations currently constrain both fatigue-oriented design of conventionally manufactured and/or AM/HM cold-work tools and further development of reliable in situ monitoring concepts in the high-hardness range of ∼55–70 HRC:

1. **Mechanistic understanding**: How manufacturing-related microstructural features—especially critical defect populations—govern statistical fatigue properties and crack-initiation mechanisms in carbide-rich CWS as a function of additional relevant influencing factors, e.g., matrix hardness and RS.
2. **Experimental baseline**: Statistically robust fatigue–strength and defect–property databases to quantify and model coupled influences of steelmaking route (cleanliness, carbide structure, extreme-value distributions of intrinsic defects), heat treatment (HT; hardness, retained austenite (RA), toughness), and surface finishing (surface roughness (SR), RS) in hardened and multistage tempered conditions.

The present work starts with an in-depth literature review and then focuses on AISI D2 and AISI A11 as two technologically relevant and microstructurally distinct representatives of carbide-rich CWS. D2 represents a less costly, Cr-rich ledeburitic CWS containing eutectic M_7C_3 carbides and is by far the most widely used carbide-rich CWS in industrial applications with severe abrasive wear. A11 follows a similar alloying concept, but represents a more costly, V-rich ledeburitic grade dominated by primary MC-type carbides.

Together with systematic variation of steelmaking route, process cleanliness, and HT, these two grades span a practically relevant range of carbide types/morphologies and other intrinsic defects encountered in cold-work tooling. Accordingly, conclusions are drawn with respect to defect-based fatigue mechanisms and process–microstructure–strength relationships in the high-hardness range, in particular for conventional (non-AM) carbide-rich CWS, rather than claiming universal generalization across all possible tool steel classes.

Compared with carbide-free and softer steels, carbide-rich CWS contain high fractions of hard phases (typically ∼10–30 vol.% carbides) embedded in a hardened and at least triple-tempered, fully martensitic matrix [14]. Together with spring and bearing steels, they belong to the broader class of hard, (ultra-)high-strength steels; however, spring steels contain no hard phases and bearing steels typically contain only smaller amounts (≪10 vol.%). Consequently, their microstructures differ fundamentally, and

1869344x, 2026, 10, Downloaded from https://onlinelibrary.wiley.com/doi/10.1002/srin.202501039 by Universitatsbibliothek RWTH Aachen University, Wiley Online Library on [05/11/2026]. See the Terms and Conditions (https://onlinelibrary.wiley.com/terms-and-conditions) on Wiley Online Library for rules of use; OA articles are governed by the applicable Creative Commons License

carbide-rich CWS can achieve higher macrohardness. Carbide-rich CWS—predominantly highly Cr- and/or V-alloyed grades (with Mo additions)—reach macrohardness values up to ∼65–66 HRC. By contrast, carbide-rich HSS are typically highly W- and/or Mo-alloyed and sometimes Co-alloyed grades (usually also containing Cr and V) and can reach ∼66–72 HRC. Achieving macrohardness above ∼66 HRC generally requires sufficiently high Co contents (enhanced solid-solution hardening) as well as elevated levels of carbon and carbide-forming elements such as W, Mo, Cr, and V (solid-solution and precipitation hardening, including secondary precipitation hardening during multistage tempering).

Because of their distinct alloying concepts, carbide-rich CWS and HSS can precipitate different special carbide types (M_xC_y) such as M_7C_3 and MC [13, 14, 57–70]. Carbide stoichiometry, crystal structure, bonding characteristics, and elemental solubilities govern key carbide properties (e.g., microhardness and fracture toughness). In-depth reviews and analytical studies on carbide structures and microstructural features in carbide-rich tool steels, and on properties of hard phases—including special carbides, nitrides and/or borides—are provided, for example, by Marsoner [13], Jesner [14], Karagöz [60, 61], Theisen [62], Kleff et al. [63], Broeckmann [64], Lentz [65], and Beiss [66–70], among others.

Carbide-rich CWS are typically not Co-alloyed (or contain only minor Co) because cold-forming process temperatures are generally below 200 °C by definition; therefore, pronounced tempering/heat resistance is usually not required. Nevertheless, both carbide-rich CWS and HSS are used in cold-work tooling, and practical application boundaries depend on required tool properties, effective process temperatures, and cost considerations.

Beyond high carbide contents, carbide-rich high-alloy tool steels differ from low-alloy and carbide-free cold- and hot-work tool steels by their pronounced secondary-hardening behavior, which depends on alloying additions (high contents of carbon and carbide-forming elements). During multistage tempering at elevated temperatures (typically ∼500–600 °C)—also required to transform RA remaining after austenitizing and quenching into martensite—additional nanometer-scale special carbides precipitate within the martensitic matrix, increasing hardness via (secondary) precipitation hardening.

The largest primary and eutectic carbides typically reach ∼1–3 µm [13, 14, 60–80] and are near-spherical in powder metallurgy (PM) steels produced by hot isostatic pressing (HIP) of gas-atomized powders. In steels manufactured by ingot casting (IC), these largest carbides can reach ∼100–500 µm [60–80], typically exhibit blocky, highly angular morphologies, and may be arranged into carbide bands during hot working (HW). Primary and eutectic carbides are readily resolved by light optical microscopy (LOM). In contrast, secondary-hardening carbides precipitated during multistage tempering typically measure ∼1–30 nm [59] (nanoparticles; ∼100 nm is often used as an upper-size threshold) and therefore require higher-resolution methods, such as scanning or transmission electron microscopy (S/TEM), for direct observation.

Compared with harder, highly wear-resistant materials such as solid cemented carbides (SCC), polycrystalline cubic boron nitride (PCBN), or diamond, carbide-rich tool steels combine high quasi-static strength with greater ductility, larger plastic deformation capacity, higher (notch) impact energy, improved fracture toughness, and favorable fatigue resistance. This property profile makes them the preferred material class for cold-work tools exposed to combinations of severe abrasive/adhesive wear and high mechanical loading (impact, quasi-static, uni- and multiaxial cyclic loading). However, these same applications render fatigue performance highly sensitive to manufacturing- and process-related microstructural features (e.g., defect populations such as carbides, inclusions, clusters, and agglomerates), HT (hardness), and surface integrity effects such as fabrication- and finishing-induced residual stresses (fiRS)—factors that must be quantified statistically to enable reliable fatigue-oriented tool design.

Depending on the specific application, tool failure may result from multiple interacting mechanisms, including impact-related damage. From a practical viewpoint, failures can be classified as predominantly wear-driven, wear–fatigue interactions in the low-cycle fatigue (LCF) regime, or wear–fatigue interactions in the HCF regime. Under LCF loading (i.e., at substantially higher stress amplitudes than in the HCF/long-life fatigue (LLF) regime), cold-work tools undergo plastic deformation in each stroke and typically reach service lives on the order of 10^2–10^4 cycles, and in some cases up to $\sim10^5$ cycles. By contrast, under LLF loading the deformation per stroke remains essentially elastic, and service lives of carbide-rich tool steels commonly extend to $\sim10^5$–10^7 cycles/strokes. The present work focuses exclusively on the latter, i.e., fatigue-controlled failures in the HCF/LLF regime.

Several authors [2–4, 6–14] showed that cold-work tools and carbide-rich tool steels frequently fail by fatigue fracture. Jung [11] and Reiss [12] demonstrated that selecting an application-optimized hardness while minimizing external and internal notch effects (e.g., via improved steelmaking routes, geometric tool optimization, and tailored HT parameters) significantly improves tool service life. An embossing stamp made of K390, a slightly modified AISI A11 grade manufactured via PM-HIP with subsequent HW, achieved an approx. eightfold higher output than a conventional D2 stamp with non-optimized geometry produced via IC + HW at a comparable macrohardness of ∼60 HRC [11].

Reiss [12] also reported for full-forward extrusion that the output per tool set (extrusion dies) made of conventional D2 can be increased by tailored HT—here, reduced macrohardness through elevated tempering—by a factor of ∼9.5–13.5, while simultaneously reducing the service life scatter within the tool set [12]. Consequently, optimizing both wear resistance and fatigue strength from a process perspective (steelmaking and microstructure) and developing robust strength/lifetime estimation methods from a design perspective (upstream fatigue-oriented tool construction) are essential for increasing productivity and reliability in high-volume metal cold-forming operations.

Regarding robust strength/lifetime estimation methods, quantitative LLF data and process–microstructure–strength relationships must be critically reviewed. At present, DIN EN ISO 4957:2018-11 [81], the FKM [82–84] guidelines, and ASTM

1869344x, 2026, 10, Downloaded from https://onlinelibrary.wiley.com/doi/10.1002/srin.202501039 by Universitatsbibliothek RWTH Aachen University, Wiley Online Library on [05/11/2026]. See the Terms and Conditions (https://onlinelibrary.wiley.com/terms-and-conditions) on Wiley Online Library for rules of use; OA articles are governed by the applicable Creative Commons License

A681-24 [85] provide neither statistical fatigue–strength data nor quantitative correlations (e.g., hardness or defect-size dependencies) for carbide-rich CWS; consequently, no uniform cyclic design standard is currently available for this steel class. This gap substantially complicates fatigue-oriented design and cyclic assessment of cold-work tools and wear-resistant components.

In the late 1980s, Berns et al. [86, 87] were among the first to show that tool steel manufacturing—including HW degree φ and HT parameters—governs carbide structures and microstructural features (carbide sizes, steel cleanliness, clustering phenomena, intrinsic defect populations) in carbide-rich CWS and HSS, and thereby controls fatigue performance.

The only HCF/LLF dataset for D2 that systematically varies both manufacturing route and HT—i.e., IC versus spray compacting (SPC), each in the soft-annealed condition (∼31 HRC) and in the hardened and triple-stage tempered condition (∼62 HRC)—was reported by Broeckmann et al. [88]. Bergström et al. [89] found a strong linear correlation ($R^2 \approx 0.91$) between macrohardness and very-high-cycle fatigue (VHCF) strength for carbide-rich PM-HIP + HW tool steels in the range of ∼58–64 HRC. In the present work, this relationship is reproduced in Figure 1 as a replot derived from the previous replot by Beiss [66], which was based on the original experimental (exp.) fatigue data.

Nevertheless, hardness alone cannot explain the fatigue behavior of CWS; additional—and potentially more relevant—fatigue-influencing factors (FIFs) must be considered. These FIFs likely interact with matrix hardness and jointly govern the fatigue limit σ_w in a more complex manner. Beiss [66–70] provided an extensive state-of-the-art review and concluded that neither toughness nor hardness constitutes the dominant FIF for hard, carbide-rich steels. However, as Beiss [66] concluded, a substantial knowledge gap persists because statistically robust, manufacturing-resolved fatigue datasets and quantitative correlations for carbide-rich CWS remain too limited to provide conclusive guidance for fatigue-oriented tool design. Further detailed reviews on available fatigue data were reported by Scholl et al. [90, 91] and Javadzadeh Kalahroudi et al. [92, 93]. Besides establishing statistical process–structure–property–performance (PSPP) correlations [94, 95] and fatigue databases, practical design frameworks require a clear identification of the most relevant FIFs and how they should be incorporated or modeled.

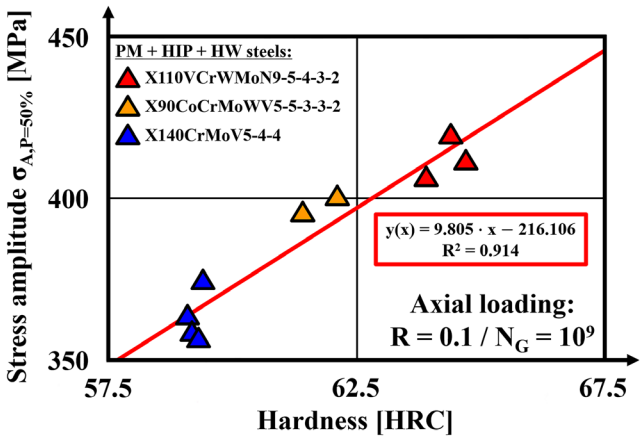

FIGURE 1 | Empirical correlation between VHCF strength at $N_G = 10^9$ cycles ($\sigma_{A,P=50\%}$ (MPa) for 50% survival probability) and macrohardness (HRC) under axial loading ($R = 0.1$; transverse orientation relative to HW direction) for three carbide-rich, hot-worked PM-HIP tool steels, based on the exp. data of Bergström et al. [89] as replotted by Beiss [66]. The present work provides a modified, colored replot including steel compositions and a linear regression (red line) with fit equation and $R^2 \approx 0.91$. Reprinted with permission [66]. Copyright 2015, ASM International.

To substantiate this need and consolidate the available fatigue data, an extended literature review was conducted here for both AISI D2 and AISI A11 steels under rotating-bending testing (RBT) at $R = -1$ (Figure 2a), as well as under axial loading at $R = -1$ and $R = 0/0.1$, the latter with superimposed quasi-static mean stresses σ_m (Figure 2b).

A summary of all abbreviations, symbols, and units used in this work is provided in Tables S1 and S2. The complete HCF/LLF dataset from the literature review shown in Figure 2, including original and re-evaluated fatigue results reported by several authors [71, 72, 88, 91, 92, 97–112], is compiled in Table S3.

Despite the strong correlation reported by Bergström et al. [89] between macrohardness and VHCF strength (Figure 1), the broader hardness ranges in Figure 2a,b demonstrate that simple linear relationships are generally inadequate, as substantial scatter is observed for both cyclic loading modes when all datapoints are included in the linear regression. Figure 2a,b also include the empirical correlation between macrohardness and fatigue limit σ_w for low-alloyed, carbide-free steels proposed by Garwood et al. [96] in the early 1950s (black dotted lines), together with the proposed applicability limit, and the validity limit of the DIN EN ISO 18265:2014-02 [113] correlation between macrohardness and quasi-static tensile strength R_m (red dotted lines in Figure 2).

Table 1 summarizes these two established literature correlations for metals: the hardness–R_m relation in Equation (1) according to DIN EN ISO 18265:2014-02 [113] is generally applicable only up to about $R_m \leq 2{,}000$ MPa (∼600 HV), and the hardness–σ_w correlation in Equation (2) according to Garwood et al. [96] holds only up to roughly 400 HV. Luke et al. [114, 115] and Scholl et al. [117] showed that for several hard steels (with $R_m \approx 2{,}000$–$3{,}000$ MPa), the hardness–R_m correlation as proposed by DIN EN ISO 18265:2014-02 [113]—which is also used in the FKM [82–84] guidelines (which are restricted in general to carbide-free, structural steels within $R_m \leq 1{,}000$–$1{,}600$ MPa or hard spring steels within $R_m \leq 2{,}500$ MPa)—is not applicable; the data fall markedly below the regression curve and exhibit wide scatter.

In Figure 2a,b, only selected literature series—data for D2 steels produced via IC or SPC according to Broeckmann et al. [88] or data from Sohar et al. [71–73] and Scholl et al. [91, 97–100, 108]—align with the empirical correlation proposed by Garwood et al. [96]. Overall, fitting literature data implies that $\sigma_{A,P=50\%}$ increases with hardness for RBT at $R = -1$ and axial loading at $R = 0/0.1$ (Figure 2a,b), but decreases for axial loading at $R = -1$ (Figure 2b). Again, accessible data and hardness ranges remain limited,

1869344x, 2026, 10, Downloaded from https://onlinelibrary.wiley.com/doi/10.1002/srin.202501039 by Universitatsbibliothek RWTH Aachen University, Wiley Online Library on [05/11/2026]. See the Terms and Conditions (https://onlinelibrary.wiley.com/terms-and-conditions) on Wiley Online Library for rules of use; OA articles are governed by the applicable Creative Commons License

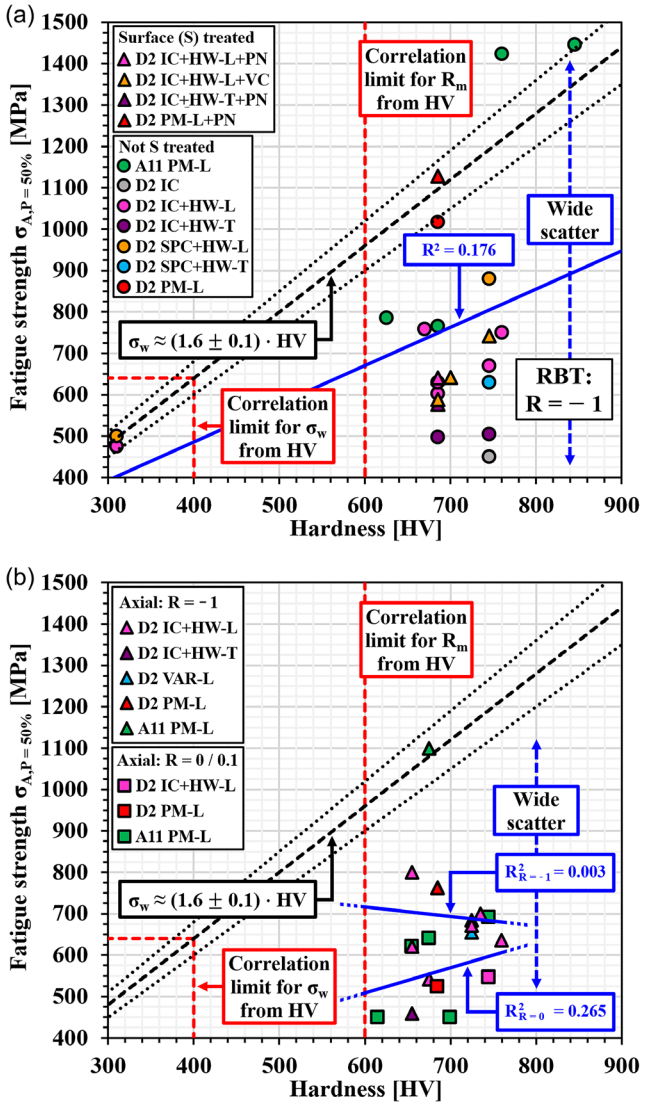

FIGURE 2 | Relationship between HCF/LLF strength at $N_G = 10^7$ ($\sigma_{A,P=50\%}$ (MPa) for 50% survival probability) and macrohardness (HV) for hot-worked (forged/rolled) D2 and A11 steels produced by different steelmaking routes under (a) RBT and (b) axial loading. The datasets are compared with the empirical hardness–σ_w correlation proposed by Garwood et al. [96] for low-alloyed, carbide-free steels. Original fatigue data were compiled from several sources [71, 72, 88, 91, 92, 97–112]. Linear-regression fit accuracies are $R^2 \approx 0.18$ for RBT and $R^2 \approx 0.003$ ($R = -1$) or $R^2 \approx 0.27$ ($R = 0/0.1$) for axial loading.

confirming the critique by Beiss [66]. Linear regressions of the compiled datapoints in Figure 2 yield low coefficients of determination R^2 (–) and only limited explanatory power ($R^2 \approx 0.18$ for RBT; $R^2 \approx 0.003$ for axial loading at $R = -1$; and $R^2 \approx 0.27$ for axial loading at $R = 0/0.1$).

These contradictions indicate further relevant FIFs acting in concert with the matrix hardness in more complex ways. Hence, classical relationships derived for low-alloyed, carbide-free, and carbon steels (macrohardness < ~400 HV) are largely unsuitable for high-alloy, carbide-rich CWS and their typical hardness ranges in industrial cold-work tooling practice.

The exp. fatigue dataset from which Garwood et al. [96] derived their empirical correlation is illustrated in Figure 3a. They showed that a so-called reverse hardness effect (RHE) generally emerges in steels above a hardness of ~400 HV; beyond this threshold, the hardness–σ_w relationship inverts and the fatigue limit σ_w decreases with further increases in hardness.

The hardness at which this inversion occurs varies among steels and correlates with critical defects, i.e., it appears to depend on intrinsic defect size (Figure 3a). This indicates a coupled (at least two-dimensional) dependence of the RHE onset in low-alloyed, carbide-free, and carbon steels (hardness > ~400 HV) on both steel cleanliness and hardness.

These findings were investigated in more detail by Murakami & Endo [116, 118, 119] at tool-relevant hardness levels (~50–58 HRC), as shown in Figure 3b. Murakami & Endo [116, 118, 119] introduced artificial defects (drilled surface holes) of controlled diameter into hardened and tempered, carbide-free carbon steel to isolate the role of crack-initiating defect size while keeping defect morphology and location constant, as a function of hardness set by HT (Figure 3b). They demonstrated that hardness effects on the fatigue limit σ_w are defect-size-dependent: in the defect-free condition ($d = 0$ µm) and for very small defects (shallow notch, $d \approx 40$ µm), σ_w increases approximately linearly with hardness (Figure 3b). With increasing defect size (medium defects, $d \approx 80$–150 µm), the hardness–σ_w slope progressively flattens, and for large artificial defects ($d \approx 260$ µm) the trend reverses such that further hardness increases reduce σ_w, i.e., the RHE becomes dominant (Figure 3b).

In contrast to carbon steels containing only artificially introduced surface holes as critical defects, carbide-rich CWS and real cold-work tools contain randomly distributed, heterogeneous defect populations that are commonly classified as intrinsic/endogenous (inherently originating from the material itself) and extrinsic/exogenous (introduced from external sources). Detailed studies and overviews on classifications, types, and origins of microstructural defects including their influences on fatigue life and performance were provided, among others, by Sohar [71], Murakami [116, 118], Picas [2, 120], Zerbst et al. [121–124], Mayerhofer [125], Kazymyrovych [126], and Chantziara et al. [127, 128].

From a strictly metallurgical and reaction-based perspective, typical intrinsic/endogenous defects in CWS include single carbides,

TABLE 1 | Widely used empirical correlations for quasi-static tensile strength and fatigue limit (for HCF/LLF) of metals/steels, including proposed validity ranges and sources.

Material	Correlation equation	No.	Validity range	Source
Metals and steels	R_m (MPa) = (3.2 ± 0.1) · hardness (HV)	**(1)**	$R_m \leq$ ca. 2,000 MPa	[113–115]
	σ_w (MPa) = (1.6 ± 0.1) · hardness (HV)	**(2)**	hardness ≤ ca. 400 HV	[96, 116]

18693044x, 2026, 10, Downloaded from https://onlinelibrary.wiley.com/doi/10.1002/srin.202501039 by Universitatsbibliothek RWTH Aachen University, Wiley Online Library on [05/11/2026]. See the Terms and Conditions (https://onlinelibrary.wiley.com/terms-and-conditions) on Wiley Online Library for rules of use; OA articles are governed by the applicable Creative Commons License

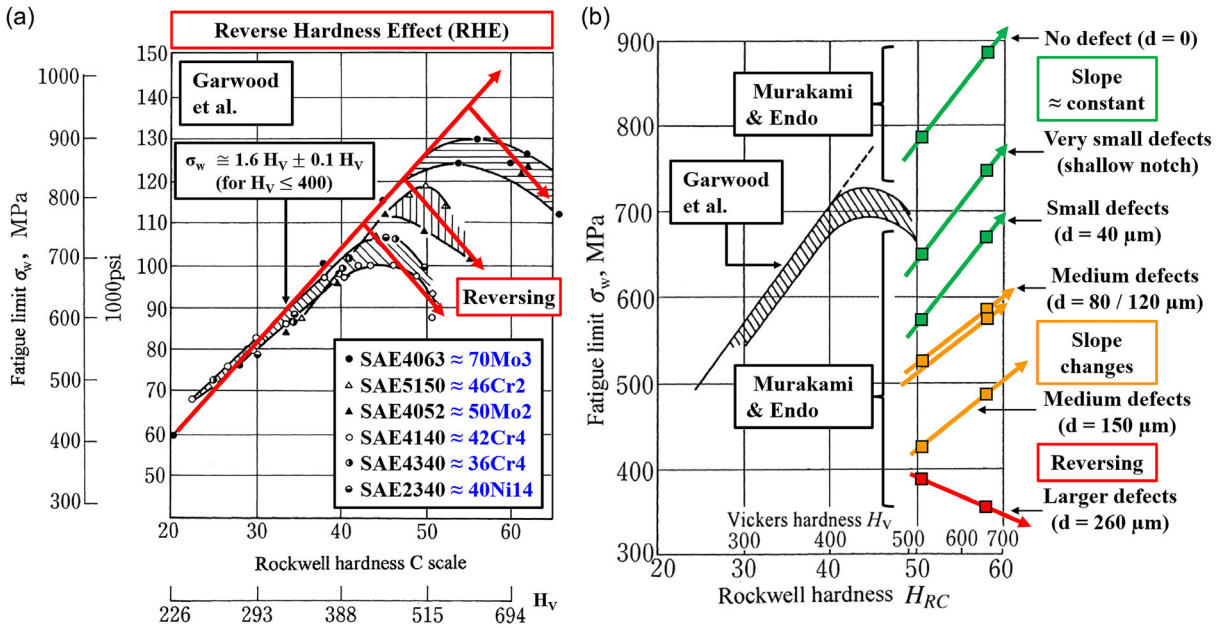

FIGURE 3 | Fatigue limit σ_w (MPa) versus macrohardness (HV/HRC) for carbide-free, low-alloyed, and carbon steels according to Murakami [116, 118]: (a) reverse hardness effect (RHE) reported by Garwood et al. [96] and reproduced here as a modified, colored replot with additional steel designations; reprinted with permission [96]. Copyright 1951, ASM International; and (b) defect-size dependence of hardness influence and RHE onset for drilled surface holes (diameter d) at ~50–58 HRC reported by Murakami & Endo [116, 118, 119]; reproduced as a modified, colored replot with defect-size groupings. Reprinted with permission [116]. Copyright 2019, Elsevier Limited.

carbide clusters/bands/networks, pores/voids, shrinkage or microcavities, segregations, and nonmetallic inclusions (NMI) precipitating from the melt during solidification or cooling (e.g., sulfides such as manganese sulfide (MnS) and, potentially, phosphides, nitrides, or borides), as well as small deoxidation products (microscopic oxides, typically with sizes < ~10–20 µm). Typical extrinsic/exogenous defects comprise macroinclusions and other impurities—particularly larger oxides (typically with sizes > ~10–20 µm) and phosphide–oxide containing particles—introduced during steelmaking and secondary metallurgy (e.g., slag entrainment, eroded refractory-lining particles, foreign contaminant particles, or hard particles originating from coated scrap), as well as surface imperfections introduced during subsequent processing and HT (e.g., scratches, machining, forming, or handling marks, as well as surface or near-surface decarburization and oxidation).

In practice, these defect classification boundaries are not always clear-cut. For example, in PM-HIP and PM-AM steelmaking, powder additivation is used to tailor wear resistance and microstructure by blending high-alloy steel powders (master-alloy powders) and/or carbide powders (e.g., Cr_3C_2, TiC, VC, or NbC) with the base steel powder prior to consolidation (e.g., carbide additivation of AISI H13 or AISI A11). Corresponding studies have been reported by Scheck/Köhler et al. [129–133], Meyer et al. [134], and Bürgi et al. [135]. An in-depth study of fatigue strength and mechanisms in PM-AM carbide-rich CWS compared to the conventional PM-HIP route was recently reported by Tegeder et al. [30, 31].

In such PM-HIP or PM-AM-HIP microstructures, fatigue performance can be governed by larger, isolated TiC carbides or coarsened VC and/or Cr_3C_2 carbides [30, 31, 130–132, 135]. From a chemical-origin perspective, these particles are extrinsic because they are externally added rather than precipitated in situ during cooling. However, they are often still treated as intrinsic defects in fatigue analysis because they are intentionally introduced constituents of the bulk microstructure. Accordingly, the pragmatic classification used here distinguishes intrinsic defects as all defects inherently present in the volume or near-surface region as a result of material production (all types of inclusions, voids, segregation products, and carbide populations), whereas extrinsic defects are only those introduced at, or originating from, the surface after basic material production, for example by forming, machining, handling (scratches), polishing, or HT.

As opposed to artificially introduced defects with precisely controlled properties, real intrinsic defects are manufacturing- and process-dependent constituents of the steel microstructure. Consequently, their geometric (and chemical) characteristics—size (including the extreme-value distribution), shape, location, clustering/agglomeration tendency, and spatial distribution—are largely uncontrolled and therefore inherently statistical [2, 30, 31, 71, 116, 118, 120–128]. Fatigue behavior in hard, defect-containing steels is thus a multidimensional, probabilistic problem and is far less clear-cut than the idealized experiments shown in Figure 3b.

Consistent with the RHE reported by Garwood et al. [96] and Murakami & Endo [116, 118, 119], Parrish [136–138] observed analogous behavior in bending fatigue of case-carburized steels as a function of core hardness. In non-carburized conditions, σ_w increases approximately linearly over ~12/25–52 HRC, whereas in case-carburized conditions σ_w begins to decrease once the core hardness exceeds about 38–40 HRC. Decarburizing specimens with case hardness of ~59–60 HRC reduces σ_w by about 50%

1869344x, 2026, 10, Downloaded from https://onlinelibrary.wiley.com/doi/10.1002/srin.202501039 by Universitatsbibliothek RWTH Aachen University , Wiley Online Library on [05/11/2026]. See the Terms and Conditions (https://onlinelibrary.wiley.com/terms-and-conditions) on Wiley Online Library for rules of use; OA articles are governed by the applicable Creative Commons License

[136]. For case-carburized as well as through-hardened and tempered (non-carburized) alloy steels, Parrish [136] reported a knee point of σ_w at ~450–500 HV; moreover, cleaner steelmaking, segregation control, or special remelting processes such as electroslag remelting (ESR) or vacuum arc remelting (VAR) can increase σ_w by up to ~25% relative to IC steels, which was confirmed for carbide-rich HSS by Randak et al. [139].

Explicit negative hardness effects were reported by Marsoner et al. [140] for several carbide-rich PM-HIP + HW tool steels with different carbide contents tested under cyclic four-point flat bending at two different austenitizing temperatures and four different macrohardness levels per grade. In the present work, their original data were replotted and assessed by linear regression of σ_w versus macrohardness to quantify slopes and trends (replots are given for K190, V10, V4, and S690 tool steels in Figure S1 together with corresponding slope evaluations in Table S4).

All series show negative slopes, although the fit quality varies markedly between the four different steel batches ($R^2 \approx 0.46$–0.88 for some batches, but $R^2 < 0.1$ for others), plausibly reflecting limited batch statistics (approx. 10 specimens per batch for the staircase regime; raw material dimensions and HW type/degree φ not reported) and the narrow hardness ranges investigated. These exp. fatigue results from Marsoner et al. [140] support the critique and knowledge gap mentioned by Beiss [66].

Some defect-size-based approaches have been proposed to estimate the quasi-static bending strength σ_B (MPa). Sohar [71] described σ_B for carbide-rich HSS at a fixed hardness of ~65 HRC by a power-law dependence on the defect diameter d (µm), representing the relevant intrinsic defect size (a modified replot is given in Figure S2). This power-law approach is given in Equation (3), which depends on the matrix fracture toughness $K_{I,crit}$ (MPa·$\sqrt{m}$), $\sqrt{d}$ ($\sqrt{\mu m}$), and a constant C (–) including $\sqrt{\pi}$ and the geometry factor Y (–). Following Murakami [116, 118], small cracks and small microstructural defects can be treated as mechanically equivalent in the linear-elastic fracture mechanics (LEFM) framework, i.e., crack length a (µm) can be substituted with defect size d (Equation (4), Figures S2 and 4). Equations (3) and (4) assume LEFM and a penny-shaped Griffith long crack (LC) in an infinite body.

$$\sigma_B = C \cdot \frac{K_{I,crit}}{\sqrt{d}} \text{ or } \sigma_B \sim \frac{K_{I,crit}}{\sqrt{\pi \cdot d}} \quad (3)$$

$$K_I = \sigma_\infty \cdot \sqrt{\pi \cdot a}\,(\cdot Y) \quad (4)$$

Much earlier, Berns [141] proposed an extension of this LEFM-based approach in Equation (3) toward a 3D mapping (σ_B–d–HV relationship), presented here in Figure 4 as a modified replot, predicting an RHE for σ_B in hard, defective steels that depends jointly on intrinsic defect size d and matrix hardness. For a given defect size d_1 smaller than the tolerable defect size d_t at a given matrix hardness, σ_B increases with hardness until a peak value (reversal point) and then decreases with further hardness increase for d_1. The critical defect size d_c is defined as the intrinsic defect size beyond which σ_B decreases with increasing d following a power-law-type behavior (analogous to Sohar [71] in

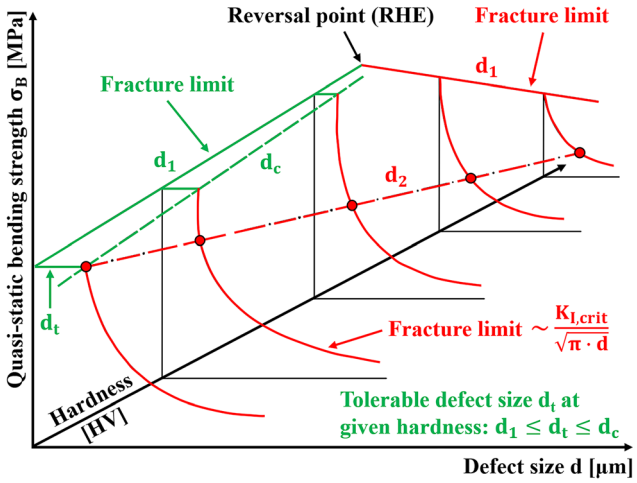

FIGURE 4 | Schematic three-dimensional representation of the defect-size- and hardness-dependent fracture–strength limit of hard, defect-containing steels, based on Berns [141]. The quasi-static bending strength, σ_B (MPa), is shown as a function of defect size, d (µm), and hardness (HV), including an RHE-type reversal of the fracture–strength limit at $d_1 = d_t = d_c$. Here, d_1 denotes a given defect size, d_c the critical defect size governing the power-law-type dependence, and d_t the tolerable defect size, with $d_1 \le d_t \le d_c$. For a larger defect, $d_2 > d_1$, the reversal shifts toward lower hardness and occurs at $d_2 = d_t = d_c$. The present modified replot additionally introduces d_t. Redrawn and adapted with permission from a previous schematic by the original author H. Berns [141]. Copyright 2026, Ruhr-Universität Bochum.

Figure S2). With increasing hardness, d_t decreases until the reversal point, where d_1, d_t, and d_c coincide ($d_1 = d_t = d_c$).

Beyond this reversal point, $d_{c/t} < d_1$, and further hardness increases necessarily decrease σ_B for a matrix containing d_1 (Figure 4). For a larger defect size, $d_2 > d_1$, the reversal point shifts to a lower hardness where $d_2 = d_t = d_c$; consequently, any further increase in hardness decreases σ_B for defect size d_2 (i.e., the RHE for d_2 is at lower hardness than for d_1). This defect-size-dependent reversal behavior is consistent with Garwood et al. [96] in Figure 3a. Since $K_{I,crit}$ in Equation (3) decreases with increasing hardness, the corresponding power-law borders shift with hardness, leading to compression/stretching of the fracture limits along the σ_B-axis (Figure 4). Besides the fatigue results for artificial defects reported by Murakami [116, 118], further exp. data reported by Tegeder et al. [30, 31] and Scholl et al. [90, 91, 97, 98, 108] show that similar power-law frameworks can describe σ_w for carbide-rich IC, PM-HIP, and PM-AM/-HIP steels at a given macrohardness, suggesting combined defect-size- and hardness-controlled fatigue mechanisms consistent with Murakami's [116, 118] $\sqrt{area}$ model.

Overall, numerous studies [1–4, 6–8, 10–14, 30–41, 56, 62–64, 66, 71–80, 86–93, 96–102, 104–112, 114–124, 126–128, 136–140] published over the past 40 years have highlighted the detrimental effects of manufacturing-related defect populations on fatigue performance and cyclic assessment of carbide-rich IC, remelted, PM-HIP, and PM-AM/-HIP tool steels. However, statistically robust, manufacturing-resolved datasets and experimentally derived correlations linking fatigue limit σ_w, hardness, and relevant defect sizes (including the RHE) remain scarce in the

1869344x, 2026, 10, Downloaded from https://onlinelibrary.wiley.com/doi/10.1002/srin.202501039 by Universitatsbibliothek RWTH Aachen University, Wiley Online Library on [05/11/2026]. See the Terms and Conditions (https://onlinelibrary.wiley.com/terms-and-conditions) on Wiley Online Library for rules of use; OA articles are governed by the applicable Creative Commons License

high-hardness regime of ∼55–70 HRC; moreover, standards and guidelines still provide no statistically validated fatigue correlations for carbide-rich CWS. Consequently, the coupled roles of cleanliness, intrinsic defect populations (including carbide structure), HT (hardness), and surface integrity (SR, RS) on HCF/LLF strength and crack-initiation mechanisms cannot yet be assessed with sufficient confidence for suitable fatigue-oriented cold-work tool design.

To address this knowledge gap, the present work combines systematic variation of steelmaking route/cleanliness and HT with LLF testing and statistical fracture-surface analysis (SFSA) to establish a manufacturing- and HT-resolved fatigue–defect database. Based on this database, PSPP correlations are derived, defect-size-controlled fatigue mechanisms are quantified, and the predictive capability of Murakami's [116, 118] $\sqrt{\text{area}}$ framework is assessed via normalized S–N curves and database-driven validation for carbide-rich CWS in the high-hardness regime.

The following research objectives are addressed:

1. **Close experimental data gap**: Derive quantitative, statistically robust PSPP databases through experimental LLF testing with systematic variation of steelmaking route, HT, microstructure, and critical defect characteristics.
2. **Close mechanistic knowledge gap**: Establish fundamental relationships between steelmaking route, HT, carbide structure/content, cleanliness, critical defect characteristics, fiRS, and LLF mechanisms/strength within the PSPP chain.
3. **RHE and defects in high-hardness regime**: Clarify and demonstrate that the classical RHE proposed by Garwood et al. [96] and Murakami [116, 118] also occurs within the hardness range of ∼55–70 HRC, and that Murakami's [116, 118] defect-size thresholds and fit-slope data from artificial defects can be transferred to real intrinsic defects originating from steelmaking.
4. **Transfer of schematic 3D framework**: Clarify and demonstrate that the 3D correlation approach in Figure 4 proposed by Berns [141] can be justifiably transferred to the LLF strength σ_w (e.g., for cyclic bending) using power-law functions at each specific hardness.
5. **Theoretical fatigue strength prediction**: Assess whether Murakami's [116, 118] $\sqrt{\text{area}}$ model is well-suited for fatigue-oriented design concepts of highly wear-resistant, cold-work tools based on normalized S–N curves and a broad statistical error and suitability validation.

Consistent with Garwood et al. [96], Murakami [116, 118], and Parrish [136], the RHE is expected in steels above ∼400–500 HV, with the critical hardness (reversal point) governed by the extreme-value distribution of intrinsic defects. The present work evaluates RHE-type behavior for carbide-rich CWS containing manufacturing-related defects and further examines how fabrication- and finishing-induced compressive residual stresses (fiCRS) can mask the apparent RHE in fatigue testing, including the conditions under which such obscuring effects occur.

2 | Materials, Methods, and Experimental Procedures

In this work, the carbide-rich, high-alloy CWS AISI D2 and AISI A11 are investigated with respect to their statistical LLF strength in the longitudinal (L) direction after systematic variation of steelmaking route and HT. In addition, D2 IC with subsequent HW was tested in the transverse (T) direction to quantify microstructural/mechanical anisotropy (anisotropy index). For consistent terminology, specimens from PM-HIP materials with specimen axis parallel to the material-flow direction during HW are designated "PM-L". Specimens from IC material are designated "HW-L" or "HW-T", depending on whether the specimen axis is aligned with the L or T direction relative to the material-flow direction during HW. This nomenclature therefore specifies both steelmaking route and specimen orientation. Common designations of the studied steels and available quasi-static properties are summarized in Table 2. Hereinafter, AISI A11 is referred to as "V10" steel, consistent with German industrial usage.

2.1 | Raw Materials and Steelmaking

Raw materials were supplied in hot-worked and soft-annealed condition as pre-peeled round bars and pre-milled blocks/plates by industrial manufacturers. D2 was provided as both IC + HW

TABLE 2 | Common designations of the studied steels and available quasi-static properties.

Steel	Tensile strength R_m (MPa)/at hardness (HRC)	Designation according to		
		DIN EN ISO 4957:2018-11 [81]	Chemical composition	AISI
D2 IC	≈1,800/59–60	1.2379	X153CrMoV12	D2
D2 PM	≈2,100/59–60			
V10 PM[1]	≈2,000/59–60	Not standardized	X245VCrMo10-5-1	A11
V10 PM[2]	n.a.			
V10 PM[3]				

Note: V10 PM-L[1]: Targeted PM-HIP + HW condition with intentionally elevated S (additional sulfurization), reduced process cleanliness during powder atomization/handling, and a low hot-working degree ($\varphi \approx 0.7$). V10 PM-L[2]: Standard PM-HIP + HW condition with baseline S level (no additional sulfurization), typical process cleanliness during powder atomization/handling, and a typical hot-working degree ($\varphi \approx 2.0$). V10 PM-L[3]: Enhanced PM-HIP + HW condition with intentionally very high process cleanliness during powder atomization/handling and a very high hot-working degree ($\varphi \approx 6.0$).
Abbreviation: n.a. = not available.

1869344x, 2026, 10, Downloaded from https://onlinelibrary.wiley.com/doi/10.1002/srin.202501039 by Universitatsbibliothek RWTH Aachen University, Wiley Online Library on [05/11/2026]. See the Terms and Conditions (https://onlinelibrary.wiley.com/terms-and-conditions) on Wiley Online Library for rules of use; OA articles are governed by the applicable Creative Commons License

and PM-HIP + HW material, whereas V10 was provided only as PM-HIP + HW material because pronounced coarsening and segregation of V-rich MC carbides during ingot solidification would promote cracking and fracture during subsequent HW. The supplied material batches and key delivery information are listed in Table 3.

The grades D2 IC, D2 PM, and V10 PM[2] represent standard industrial production with typical cleanliness and HW levels (depending on plant-specific processing). In contrast, V10 PM[1] and V10 PM[3] were intentionally manufactured with defined process variations (see footnotes for the V10 grades). V10 PM[3] was produced with high melt/process cleanliness during powder atomization, controlled powder handling, and increased HW degree ($\varphi \approx 6.0$). V10 PM[1] was produced (as part of the experimental concept) with reduced atomization/process cleanliness, uncontrolled powder handling, strongly reduced HW degree ($\varphi \approx 0.7$), and additional melt sulfurization using ferrosulfur (FeS). Increasing the sulfur content is commonly applied in industrial/large-scale steelmaking to promote sulfide precipitation (e.g., MnS), thereby improving machinability and reducing downstream machining costs. Key information on manufacturing and HW parameters as well as qualitative carbide-structure characteristics of the studied carbide-rich, high-alloy CWS are summarized in Table 4.

Bulk chemical compositions determined by optical emission spectroscopy (OES) are given in Table 5. Compared with wet-chemical analysis, OES may exhibit uncertainty for light

TABLE 3 | Overview of the supplied raw-material batches (delivery form, steelmaking route, and processing state) for the investigated carbide-rich, high-alloy CWS.

Steel	Supplier	Producer	Form (–)	Dimensions (mm)	Orientation (–)
D2 IC	DEW GmbH (Witten)		Plate	≈1200 × 500 × 45	L and T
D2 PM	Dörrenberg Edelstahl GmbH		Rods	Ø ≈ 35.5	Only L
V10 PM[1]	DEW GmbH (Krefeld)		Blocks	≈700 × 320 × 320	
V10 PM[2]	ZAPP Precision Metals GmbH	Erasteel SAS	Rods	Ø ≈ 58.0	
V10 PM[3]		voestalpine Böhler Edelstahl GmbH		Ø ≈ 13.1	

Note: V10 PM-L[1]: Targeted PM-HIP + HW condition with intentionally elevated S (additional sulfurization), reduced process cleanliness during powder atomization/handling, and a low hot-working degree ($\varphi \approx 0.7$). V10 PM-L[2]: Standard PM-HIP + HW condition with baseline S level (no additional sulfurization), typical process cleanliness during powder atomization/handling, and a typical hot-working degree ($\varphi \approx 2.0$). V10 PM-L[3]: Enhanced PM-HIP + HW condition with intentionally very high process cleanliness during powder atomization/handling and a very high hot-working degree ($\varphi \approx 6.0$).

TABLE 4 | Steelmaking route, HW information (including HW degree φ), and qualitative microstructural features (carbide structure including carbide content, type, and shape) of the raw materials.

		Hot working		Carbides		
Steel	Manufacturing (–)	Type (–)	Degree φ (–)	Content (vol.%)	Type (–)	Shape (–)
D2 HW-L/-T	IC + HW	Open-die/Rolling	≈2.5	≈12–14	M_7C_3	Large, blocky
D2 PM-L	PM-HIP + HW	Round/Long	≈5.1			Small, spheroidal, fine-disperse distribution
V10 PM-L[1]		Open-die	≈0.7	≈20–22	MC	
V10 PM-L[2]		Round/Long	≈2.0			
V10 PM-L[3]			≈6.0			

TABLE 5 | Bulk chemical compositions of the studied tool steel grades (wt.%).

	Chemical composition (wt.%) obtained by OES (average values)											
Steel	C	V	Cr	Mo	W	Si	Al	P	S	Co	Mn	Ni
D2 HW-L/-T	1.52	0.70	11.94	0.77	0.06	0.32	0.004	0.017	0.001	0.02	0.44	0.20
D2 PM-L	1.55	0.71	11.41	0.82	0.04	0.22	0.003	0.016	0.006	0.01	0.25	0.20
V10 PM-L[1]	2.52	9.39	5.59	1.29	0.06	1.06	0.005	0.035	0.098	0.06	0.53	0.08
V10 PM-L[2]	2.56	10.18	5.52	1.14	0.19	0.75	0.005	0.029	0.071	0.06	0.50	0.08
V10 PM-L[3]	2.50	9.40	5.38	1.06	0.09	0.72	0.003	0.026	0.082	0.04	0.45	0.15

Note: For each tool steel alloy, three to four OES measurements were performed; values are averages; balance Fe.

1869344x, 2026, 10, Downloaded from https://onlinelibrary.wiley.com/doi/10.1002/srin.202501039 by Universitatsbibliothek RWTH Aachen University, Wiley Online Library on [05/11/2026]. See the Terms and Conditions (https://onlinelibrary.wiley.com/terms-and-conditions) on Wiley Online Library for rules of use; OA articles are governed by the applicable Creative Commons License

elements (e.g., C, N, O) and can be sensitive to local segregation (notably S and P), because each measurement represents a local spot analysis. OES was performed using a SPECTROMAXx MLX07 Arc/Spark OES Analyzer (2019, SPECTRO Analytical Instruments GmbH) with SPECTRO Spark Analyzer Pro MAXx software and an internal database linked to the German steel-key. Calibration was carried out using the intelligent Calibration (iCal) routine based on certified standards and calibration curves; curves were updated as needed by remeasuring an iCal reference. Before each measurement series, a certified control specimen was analyzed to confirm instrument stability and exclude signal drift or systematic deviations.

The D2 and V10 steels differ primarily in carbon content and in the levels of carbide-forming elements (notably V and Cr), resulting in different special carbide types and carbide volume fractions (Tables 4 and 5). For the PM-HIP grades, the primary/eutectic carbide size scale and morphology are expected to be broadly comparable because they are governed mainly by the high cooling rates during powder atomization, which are substantially higher than in IC and typically also higher than in remelting routes such as ESR or VAR.

By contrast, D2 IC (D2 HW-L/-T) is expected to contain markedly larger, irregular/blocky carbides that are rearranged into carbide bands during HW, contributing to microstructural anisotropy. Owing to the higher C and V contents, the V10 grades exhibit higher carbide contents and can achieve higher maximum hardness levels after hardening and multistage tempering (∼65–66 HRC) than D2 (∼62–63 HRC).

2.2 | Sample Fabrication, Heat Treatments, Microstructures, and Cleanliness Analysis

Fatigue specimens were extracted from the as-received materials (blocks by sawing; rods by sawing and wire EDM) and soft-turned to oversize (Ø ≈ nominal + 1.0–1.5 mm) on a high-speed CNC lathe (Traub Drehmaschinen GmbH) using SCC cutting tool inserts. All oversized specimens were systematically heat-treated at Dörrenberg Edelstahl GmbH or Bodycote Heat Treatment GmbH in industrial vacuum furnaces using the HT schedules summarized in Tables 6 and 7 for each grade/batch. For vacuum hardening, high austenitizing temperatures T_A (°C) with corresponding holding times t_A (min) were selected for D2 and V10 to enable the maximum hardness levels of ∼62–63 HRC and ∼65–66 HRC, respectively.

To ensure comparable solution states prior to high-pressure nitrogen-gas quenching, T_A and t_A were kept constant within each steel grade, thereby providing consistent as-quenched conditions across batches. Different macrohardness levels were then obtained solely by varying the tempering temperatures T_T (°C) at constant tempering time t_T (h), as shown in Tables 6 and 7. Multistage tempering was performed at least three times per batch to reach the target hardness and to transform RA from gas-quenching into martensite. The achieved macrohardness values are summarized in Table 8 as mean values with standard deviation (SD).

Because tempering response can vary between batches, some batches required a fourth or fifth tempering cycle to reach the defined target hardness (particularly in the lower hardness range). This HT strategy enables hardness variation primarily through changes in martensitic carbon content and the amount/size distribution of nanometer-scale secondary-hardening carbides, while maintaining comparable austenitizing conditions and primary/eutectic special carbide structures for a given alloy and steelmaking route.

Final machining to the geometry shown in Figure 5 was performed by hard-turning using PCBN inserts (TiN-coated CBN20RC, Rinaldi-Tools; KBN25M, Kyocera). Surface finishing was performed either manually by (i) longitudinal polishing (LP) using SiC abrasive paper with stepwise decreasing grit size (all D2

TABLE 6 | HT schedules and target hardness levels (HRC) for RBT fatigue specimens of the D2 steels (vacuum hardening/furnace and high-pressure nitrogen-gas (N) quenching at $p_N \approx$ 5–8 bar).

Steel	Target hardness (HRC)	Austenitizing ($T_A \approx$/$t_A \approx$)	Tempering ($T_T \approx$/$t_T \approx$)	Tempering repeats
D2 IC/PM-L	53–54	1050–1060 °C/ 30 min	580 °C/2–3 h	3–5 ×
	56–57		550 °C/2–3 h	
	59–60		530 °C/2–3 h	
	62–63		510 °C/2–3 h	

TABLE 7 | HT schedules and target hardness levels (HRC) for RBT fatigue specimens of the V10 steels (vacuum hardening/furnace and high-pressure nitrogen-gas (N) quenching at $p_N \approx$ 5–8 bar).

Steel	Target hardness (HRC)	Austenitizing ($T_A \approx$/$t_A \approx$)	Tempering ($T_T \approx$/$t_T \approx$)	Tempering repeats
V10 PM-L[2]	45–46	1180–1190 °C/ 15–20 min	670 °C/2–3 h	3–5 ×
V10 PM-L[1/2/3]	56–57		590 °C/2–3 h	
	59–60		570 °C/2–3 h	
	62–63		540 °C/2–3 h	
	65–66		510 °C/2–3 h	

1869344x, 2026, 10, Downloaded from https://onlinelibrary.wiley.com/doi/10.1002/srin.202501039 by Universitatsbibliothek RWTH Aachen University, Wiley Online Library on [05/11/2026]. See the Terms and Conditions (https://onlinelibrary.wiley.com/terms-and-conditions) on Wiley Online Library for rules of use; OA articles are governed by the applicable Creative Commons License

TABLE 8 | Achieved macrohardness values (HRC) of RBT fatigue specimens after systematic HT (mean value ± standard deviation (SD), based on four to five fatigue specimens per steel batch).

Steel	Target hardness (HRC)	Achieved hardness (HRC)		
		D2 HW-L	D2 HW-T	D2 PM-L
D2 IC/PM-L	53–54	53.3 ± 0.6	53.4 ± 0.6	53.8 ± 0.5
	56–57	56.4 ± 0.4	56.8 ± 0.4	56.3 ± 0.5
	59–60	59.6 ± 0.5	59.6 ± 0.5	59.7 ± 0.6
	62–63	62.4 ± 0.5	62.6 ± 0.6	62.2 ± 0.6
		V10 PM-L[1]	**V10 PM-L[2]**	**V10 PM-L[3]**
V10 PM-L[1/2/3]	45–46	—	45.6 ± 0.6	—
	56–57	56.6 ± 0.5	56.7 ± 0.6	56.3 ± 0.5
	59–60	59.3 ± 0.6	59.8 ± 0.6	59.4 ± 0.6
	62–63	62.5 ± 0.7	62.4 ± 0.7	62.6 ± 0.7
	65–66	65.8 ± 0.7	65.6 ± 0.7	65.7 ± 0.5

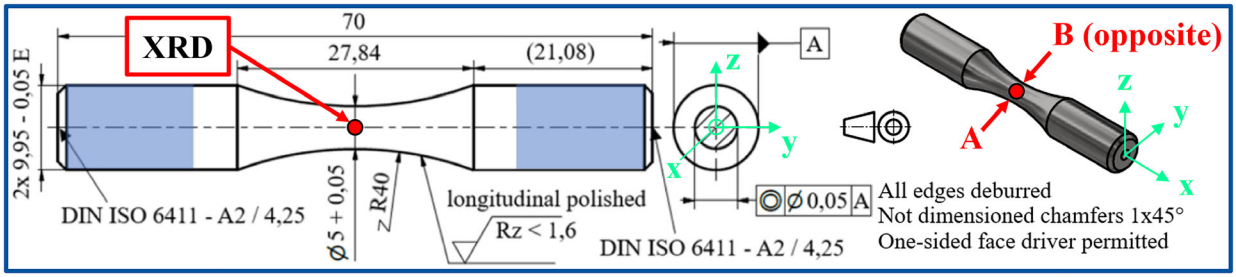

FIGURE 5 | Final specimen geometry for fatigue testing after HT, hard-turning with PCBN inserts on a high-speed CNC lathe and surface finishing. Marked regions: light blue = metallographic sampling locations for LOM; red = XRD measurement locations for surface measurements/depth profiles (spot B opposite spot A); light green = coordinate system for fatigue stresses and fiRS.

and V10 PM-L[1] batches) or mechanically by (ii) automated polishing (AP) at OTEC Präzisionsfinish GmbH using dry drag finishing (DF-3/4 Tools; microfinishing granulate) for V10 PM-L[2/3] batches. Both finishing routes produced mirror-like surfaces with low SR across all batches (final SR about $R_Z \ll 1.0\,\mu m$).

Representative microstructures/carbide structures are shown in Figure 6 as light optical micrographs after area etching using either 3% Nital (HNO_3 + C_2H_5OH; room temperature (RT); ~5–10 s) or V2A etchant (HNO_3 + C_2H_5OH + $HCl \cdot H_2O$; about 60 °C; 6–12 s). Metallographic samples were extracted from the specimen heads (Figure 5) and analyzed by LOM using microscopes from Leica Microsystems GmbH and Carl Zeiss Microscopy GmbH. For D2 HW-T and D2 PM-L, representative micrographs are shown for all four investigated hardness levels in Figure 6a–h (additional carbide-color-etched micrographs of the D2 steels are provided in Figure S3).

All investigated batches exhibit a fully martensitic matrix after HT. D2 IC contains large, sharp-edged blocky carbides (Figure 6a–d for D2 HW-T; Figure 6i for D2 HW-L). Due to subsequent HW, eutectic carbides are rearranged into bands in L direction; consequently, carbide sizes, shapes, and spatial distributions differ between D2 HW-T and D2 HW-L (cf. Figure 6a–d vs. Figure 6i). D2 PM-L (Figure 6e–h) and V10 PM-L[1/2/3] (Figure 6j–l) show comparatively homogeneous dispersions of fine, near-spherical carbides. The D2 batches contain about 12–14 vol.% carbides and the V10 batches about 20–22 vol.% (Table 4).

In D2 steels, special carbides are eutectic Cr-based M_7C_3 (D2 HW-L/-T exhibit the same type and content as D2 PM-L but differ in carbide size and morphology), whereas V10 steels contain primary V-based MC monocarbides. Although chemistry, stoichiometry, crystallography and hardness of the special carbides differ, their size scale in D2 PM-L is comparable to that in the V10 grades. At first glance, the V10 PM-L[1/2/3] microstructures in Figure 6j–l appear similar (carbide sizes, shapes, spatial distributions, carbide coarsening phenomena, visible NMI sizes and amounts; cf. Figure 6j–l), which might suggest similar LLF properties; however, this is not the case, and their microstructures differ significantly (the relevant differences are addressed and compared in detail later). For instance, metallographic samples from V10 PM-L[1] frequently contain regions with large macroinclusions and/or (strongly) coarsened single MC carbides or MC carbide clusters (examples in Figures S4 and S5).

To determine steel cleanliness, several standards are available (e.g., DIN EN 10247:2017-09 [142], JIS G 0555:2023-08-21 [143], ASTM E45-25 [144], ASTM E2142-08R23 [145], and ASTM E2283-08R19 [146], among others). These approaches typically rely on measuring and/or counting NMIs via plane-by-plane observations over defined inspection areas. To compare

1869344x, 2026, 10, Downloaded from https://onlinelibrary.wiley.com/doi/10.1002/srin.202501039 by Universitatsbibliothek RWTH Aachen University, Wiley Online Library on [05/11/2026]. See the Terms and Conditions (https://onlinelibrary.wiley.com/terms-and-conditions) on Wiley Online Library for rules of use; OA articles are governed by the applicable Creative Commons License

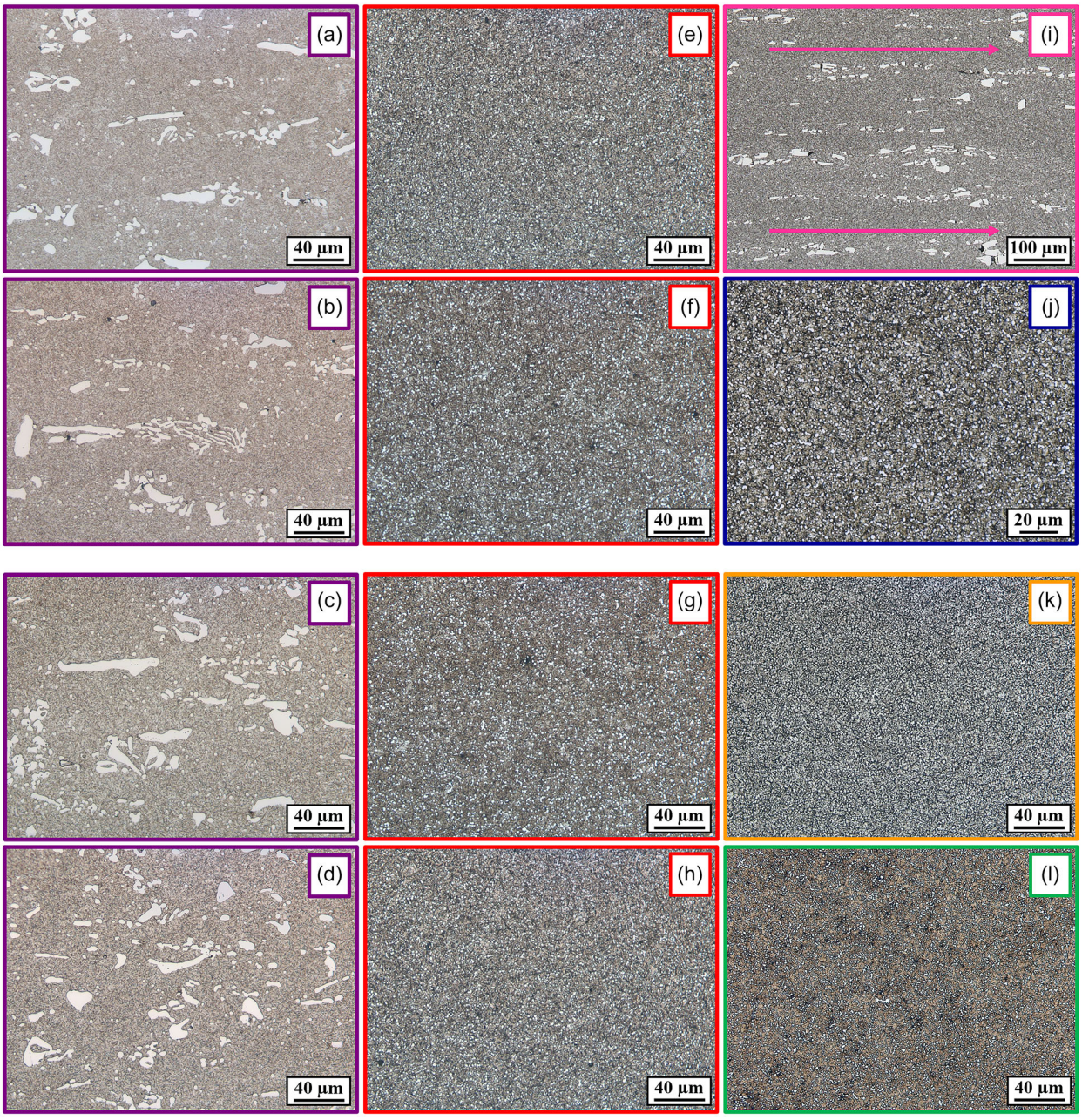

FIGURE 6 | Representative etched microstructures after HT. Nital-etched D2: HW-T at (a) 53–54 HRC, (b) 56–57 HRC, (c) 59–60 HRC, (d) 62–63 HRC; PM-L at (e) 53–54 HRC, (f) 56–57 HRC, (g) 59–60 HRC, (h) 62–63 HRC; and HW-L at (i) 59–60 HRC (arrows indicate HW material-flow direction; M_7C_3 carbides are crushed/rearranged into bands). V2A-etched V10 at 59–60 HRC: (j) PM-L^1, (k) PM-L^2, and (l) PM-L^3.

manufacturing-related critical microstructural constituents (referred to here as defects) in IC and PM-HIP microstructures, cleanliness grade analysis (CGA) according to ASTM E2283-08R19 [146] was performed for V10 PM-L^1, D2 HW-L, and D2 PM-L (examples in Figures S4–S7). The CGA procedure applied here was as follows:

1. Metallographic samples were extracted from specimen heads after RBT fracture (Figure 5), yielding at least six specimens per steel grade with sufficient inspection areas.
2. After metallographic preparation, each specimen surface plane was systematically scanned by LOM, and high-magnification images of the largest NMIs were acquired (typically 5–10 extremes per inspected plane and specimen).
3. Specimens were then ground and polished again to remove material and generate the next inspection plane at least ~100 µm (or more) below the previous plane, thereby avoiding repeated evaluation of the same largest NMIs (or portions thereof).
4. This procedure was repeated until images of extreme NMIs from at least four inspection planes per specimen were obtained. NMI boundaries were segmented on LOM images using image-processing software, and geometric parameters—e.g., area A (µm^2), circularity (–), perimeter (µm)—were calculated for each NMI and stored in a CGA database.
5. Finally, the defect size $\sqrt{\text{area}}$ according to Murakami [116, 118] was computed and stored for each extreme

1869344x, 2026, 10, Downloaded from https://onlinelibrary.wiley.com/doi/10.1002/srin.202501039 by Universitatsbibliothek RWTH Aachen University, Wiley Online Library on [05/11/2026]. See the Terms and Conditions (https://onlinelibrary.wiley.com/terms-and-conditions) on Wiley Online Library for rules of use; OA articles are governed by the applicable Creative Commons License

NMI. The extreme-value data from all inspection planes were ranked from smallest to largest for each grade, and the overall 24 largest values were used, following ASTM E2283-08R19 [146], to estimate the underlying extreme-value distribution and to enable comparison with critical-defect data obtained from fracture-surfaces after RBT.

6. In addition, for V10 PM-L[1], this CGA procedure was also applied (besides NMIs) to conspicuously large/coarsened MC carbide clusters observed in the inspection planes.

The extreme-value analysis according to ASTM E2283-08R19 [146] uses a two-parameter Gumbel extreme-value distribution (double-exponential function) as shown in Equations (5) and (6), with λ (–) as the location parameter and δ (–) as the scale parameter. The parameters λ and δ were first estimated using the method of moments (MOM) according to ASTM E2283-08R19 [146], yielding λ_{MOM} and δ_{MOM} from the 24 collected extremes. These initial estimates were then refined by maximum likelihood (ML) using numerical optimization (GRG-Nonlinear solver). The refined parameters λ_{ML} and δ_{ML} were obtained by maximizing the likelihood of the observed extreme-value dataset. The final λ_{ML} and δ_{ML} values were used to plot the extreme-value distribution in the form of the reduced variate y (–), as defined in Equation (7), as a function of defect size $\sqrt{\text{area}}$ (µm).

Probability density function for continuous random variable x (µm):

$$f(x) = \frac{1}{\delta} \cdot \left[e^{-\frac{x-\lambda}{\delta}} \right] \cdot e^{\left[-e^{-\frac{x-\lambda}{\delta}} \right]} \tag{5}$$

Cumulative distribution for continuous random variable x (µm):

$$F(x) = e^{\left[-e^{-\frac{x-\lambda}{\delta}} \right]} \tag{6}$$

Reduced variate y (–) related to the probability density function:

$$y = F(P) = -\ln[-\ln[F(y)]] = -\ln[-\ln(P)] \tag{7}$$

The same procedure was applied to extreme-defect datasets collected from fracture-surfaces after RBT. In this case, the extreme-value analysis was consistently performed according to ASTM E2283-08R19 [146] using the 24 largest critical defect sizes $\sqrt{\text{area}}$ from each S–N curve and/or steel batch obtained via the SFSA workflow; smaller defects contained in the database were excluded from this extreme-value analysis and the corresponding plots. Quantitative comparisons between CGA-derived extreme-value statistics (metallographic observations using LOM) and SFSA-based critical-defect data after RBT (fracture-surface observations using SEM) are presented in Figure 13a–f (Section 3.3) and Tables S5 and S6.

2.3 | Fabrication- and Finishing-Induced Residual Stresses and Related XRD Measurements

As previously emphasized by Sohar [71, 72], Parrish [136, 138], Marsoner et al. [147], Caruso et al. [148], and Jomaa et al. [149], specimen fabrication/machining and finishing/polishing (e.g., soft- and hard-machining, manual and automated surface polishing) can introduce surface-near tensile or compressive residual stresses (T/CRS) in metallic fatigue specimens. Outeiro [150] gives a detailed overview of machining-induced RS, including their mechanistic origin and the influence of process parameters on magnitude, sign, and depth progression. fiRS, including machining-induced RS, are multiaxial, quasi-static, metastable stress states that are in mechanical equilibrium (self-equilibrated) and exist in an isolated component without externally applied forces or moments [150]. They are commonly classified by the length scale over which they equilibrate (types A–C), following Outeiro [150]:

- **Type A**: Macro RS equilibrated on macroscopic length scales (e.g., several grains to the full component or structure size).
- **Type B**: Micro RS equilibrated on microscopic length scales (e.g., typically the grain scale).
- **Type C**: Micro RS equilibrated on smaller microscopic length scales (e.g., crystallographic unit-cell/atomic scale).

Primarily two coupled mechanisms lead to the generation of fiRS: (i) A mechanical contribution associated with strong, heterogeneous plastic deformation and deformation gradients extending from the machined surface into the bulk, which generate heterogeneous strain/stress fields and (ii) a thermal contribution caused by heat generation from plastic deformation as well as friction at the tool-chip and tool-workpiece interfaces—in particular along the tool flank contact [150]. Thermal expansion/contraction—often promoting rather TRS than CRS—and, in some cases, phase transformations in the machining-affected layers may further contribute to near-surface plasticity and the generation of fiRS.

The final surface integrity state, including fiRS, is dominated by the last cutting operation(s) and these stresses arise from the energy input required for plastic deformation and chip formation. Rapid cooling with metal-working fluid can superimpose additional thermal stresses [150]. The fiRS generated by hard-machining and/or surface polishing of fatigue specimens are predominantly macroscopic type-A stresses. Following Parrish [136, 138], these type-A fiRS can be further subdivided into three characteristic macroscopic depth-profile types, schematically illustrated in Figure 7 (example: hard grinding):

- **Type A-I**: High surface TRS decreasing gradually into the bulk (approaching slight CRS at depth).
- **Type A-II**: High surface CRS transitioning rapidly into high TRS in the subsurface (then decaying toward slight CRS at depth).
- **Type A-III**: High surface CRS decreasing (rapidly or more gradually) into the bulk (approaching slight TRS at depth).

For fatigue specimens made of carbide-rich, high-alloy CWS, hard-machining prior to polishing and RBT is essential to eliminate HT-induced geometric distortions (e.g., volume expansion during martensite formation under rapid cooling/high hardening). Accordingly, in addition to X-ray diffraction (XRD) phase analysis for possible RA remaining from gas-quenching in the

1869344x, 2026, 10, Downloaded from https://onlinelibrary.wiley.com/doi/10.1002/srin.202501039 by Universitatsbibliothek RWTH Aachen University, Wiley Online Library on [05/11/2026]. See the Terms and Conditions (https://onlinelibrary.wiley.com/terms-and-conditions) on Wiley Online Library for rules of use; OA articles are governed by the applicable Creative Commons License

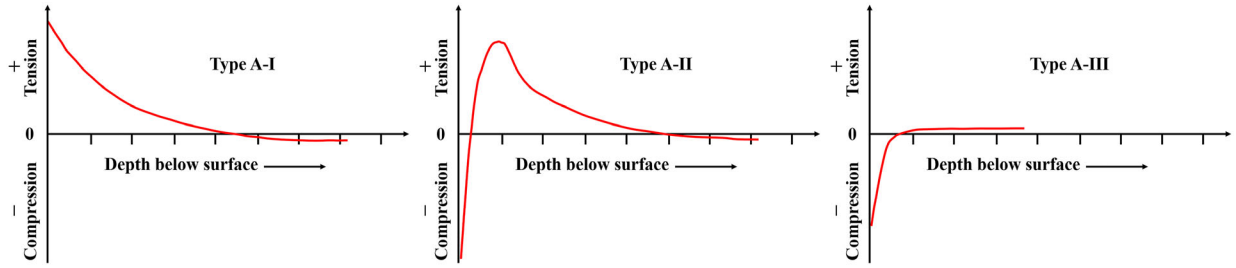

FIGURE 7 | Schematic illustration of three different type-A macro fiRS depth profiles generated by hard grinding according to Parrish [136, 138]. Type A-I: abusive grinding with high heat and heterogeneous plastic deformation, resulting in high TRS (surfaces may be thermally damaged/cracked). Type A-II: typical grinding with lower heat; near-surface plastic deformation partly balances the tensile peak yielding both CRS and TRS. Type A-III: optimal grinding with low heat, producing pronounced CRS balanced by deeper, smoother counterbalancing tensile stresses. Redrawn and adapted with permission [138]. Copyright 1999, ASM International.

microstructures after HT, axial and tangential (circumferential) RS were measured at the surfaces of the narrowest specimen sections (Figure 5) for selected D2 and V10 PM-L[1] batches after hard-turning with PCBN inserts and surface polishing. RS were evaluated by XRD and the classical $\sin^2\Psi$-method as per DIN EN 15305:2009-01 [151] using the following settings: X-ray tube Cr-K_α; lattice plane Fe {211}; Young's modulus $E = 210$ GPa; Poisson's ratio $\nu = 0.3$; Bragg angle $2\theta = 156.4°$; φ angles = 0°, 45°, and 90°; Ψ angles = nine angles. An elliptical fit approach was used to evaluate the shear stresses as well; smoothing and a Lorentzian function were applied for peak evaluation. Surface RS measurements were carried out on an XRD 3003 PTS diffractometer system (Seifert Analytical X-Ray; scintillation detector). Evaluation was performed using Seifert XRD analysis software (version 6). RS depth profiles were measured in defined incremental steps from the surface into the volume using an Xstress DR45 diffractometer system (Stresstech GmbH Germany) equipped with two symmetrically arranged metal oxide semiconductor (MOS) linear detectors; evaluation and calculation of the RS tensor σ_{ij} as shown in Equation (8) were performed using Xstress Studio software.

Here σ_{11}, σ_{22}, and σ_{33} (MPa) are the normal stresses and τ_{12}, τ_{13}, and τ_{23} (MPa) are the shear stresses acting on an infinitesimal cube element. The first index denotes the plane-normal direction and the second index the stress direction. According to the coordinate system defined here in Figure 5 for the RBT specimens (also see Figure S8 for further explanation), σ_{11} denotes the normal stress along the x-axis (axial RS, parallel to the fatigue test stress direction), σ_{22} along the y-axis (tangential RS, perpendicular to the fatigue test stress direction), and σ_{33} along the z-axis (radial RS). At free surfaces, $\sigma_{33} = 0$ (plane-stress condition). Because σ_{ij} is symmetric ($\tau_{12} = \tau_{21}$, $\tau_{13} = \tau_{31}$, $\tau_{23} = \tau_{32}$) and $\sigma_{33} = 0$ at the surface, the RS tensor reduces to five independent stress components (σ_{11}, σ_{22}, τ_{12}, τ_{13}, and τ_{23}), as indicated on the right-hand side of Equation (8).

$$\sigma_{ij} = \begin{pmatrix} \sigma_{xx} & \tau_{xy} & \tau_{xz} \\ \tau_{yx} & \sigma_{yy} & \tau_{yz} \\ \tau_{zx} & \tau_{zy} & \sigma_{zz} \end{pmatrix} = \begin{pmatrix} \sigma_{11} & \tau_{12} & \tau_{13} \\ \tau_{21} & \sigma_{22} & \tau_{23} \\ \tau_{31} & \tau_{32} & \sigma_{33} \end{pmatrix} \widehat{=} \begin{pmatrix} \sigma_{11} & \tau_{12} & \tau_{13} \\ \tau_{12} & \sigma_{22} & \tau_{23} \\ \tau_{13} & \tau_{23} & 0 \end{pmatrix} \quad (8)$$

Surface material was removed at a fixed location in the minimum-diameter section by electrolytic ablation. The removal depth after each step was measured using a fine steel probe needle mounted on a cantilever (the ablation-depth measurement accuracy is ~1–2 µm for this needle–cantilever setup). RS depth profiles were then obtained as a function of distance from the original surface, d_S (µm).

2.4 | Statistical Fatigue Testing, Fracture-Surface Analysis, Data Collection, and Sorting

To establish a manufacturing- and hardness-resolved database linking statistical fatigue strengths to crack-initiating (critical) defect characteristics, a four-step procedure was applied:

- **Statistical rotating-bending fatigue testing** (including consistent handling and documentation of fatigue specimens and fracture surfaces).
- **SFSA** to quantify geometric and chemical properties of critical defects and defect populations.
- **Data collection, sorting, and preparation** (including implementation of selected model equations for subsequent accuracy/error validations).
- **Compilation of a statistical fatigue–strength and defect–property database** (used subsequently to derive PSPP correlations and validate fatigue models).

Statistical fatigue testing was performed using the specimen geometry shown in Figure 5 under RBT on Rapid PUNZ four-point bending machines (Carl Schenck AG) at a stress ratio $R = -1$ and test frequencies $f_{Testing} \approx 100$–115 Hz, in accordance with DIN 50113:2018-12 [152]. The four-point configuration produces a trapezoidal bending-moment distribution with a constant bending moment across the central test section (head-to-head) for a given diameter.

The bending moment was applied mechanically using one or two calibrated standard weights mounted on a lever arm at adjustable distances from the support point; the selected weight configuration defines the target bending moment (and corresponding test stress level for the given diameter) and remains constant throughout the test. The machine failure criterion was complete specimen fracture (testing was not stopped at crack initiation or

1869344x, 2026, 10, Downloaded from https://onlinelibrary.wiley.com/doi/10.1002/srin.202501039 by Universitatsbibliothek RWTH Aachen University, Wiley Online Library on [05/11/2026]. See the Terms and Conditions (https://onlinelibrary.wiley.com/terms-and-conditions) on Wiley Online Library for rules of use; OA articles are governed by the applicable Creative Commons License

visible surface cracking). For each batch, the LLF regime was determined according to DIN 50100:2022-12 [153] using the staircase method, and the short-life fatigue (SLF) regime using the horizon method. Statistical evaluation was performed with the in-house software SAFD 5 ("Statistical Analysis of Fatigue Data – Version 5"; Figure 8) following Klubberg et al. [154] and DIN 50100:2022-12 [153]. For the LLF regime, in SAFD 5, a simple-logarithmic Gaussian distribution in S–log N space was assumed, using the Rossow [155] estimator given in Equation (9), including sample weighting (to account for unequal sample numbers per staircase level) and the combination method according to Klubberg et al. [154]. In Equation (9), P (%) is the estimated failure probability at a given staircase stress level σ_a (MPa) with i (–) fractures and n (–) run-outs recorded at that stress level.

$$P\,(\%) = \frac{3 \cdot i - 1}{3 \cdot n + 1} \tag{9}$$

In SAFD 5, the P values of the individual staircase levels are evaluated jointly to obtain the statistical fatigue–strength distribution $\sigma_{A,P}$ (MPa). The absolute (abs.) LLF scatter band (MPa) is defined here as the difference between $\sigma_{A,P=99\%}$ and $\sigma_{A,P=50\%}$ (upper band) or between $\sigma_{A,P=1\%}$ and $\sigma_{A,P=50\%}$ (lower band). The relative (rel.) LLF scatter band (%) is calculated by normalizing the respective abs. LLF scatter band (MPa) by $\sigma_{A,P=50\%}$ (MPa), enabling comparison across S–N curves with different statistical mean values and band sizes.

For the SLF regime, the S–N curve was determined using the pearl-string method (linear regression of fracture data up to the LLF transition). The SLF scatter band was normalized to the mean cycles to failure, $\overline{N}_{Fracture}$, such that regressions for different failure probabilities share a common slope. Staircase run-outs were reused via the horizon method at elevated stress levels (upstairing), together with additional specimens, to establish the SLF slopes. The applied SAFD 5 settings are summarized in Figure 8.

Staircase testing requires a defined stress increment δ (stair-step size), either constant δ_C or logarithmic δ_{Log} (scatter-dependent). Selecting δ is critical to obtain an adequate number of mixed staircase levels (stress levels containing both fractures and run-outs), which dominate the statistical evaluation. DIN 50100:2022-12 [153] recommends achieving ~1–3 mixed levels and, where feasible, using δ_{Log}; in practice, ~2–4 well-populated mixed staircase levels are often targeted for robust statistical assessment. Because the scatter of the investigated carbide-rich CWS was not known a priori, a constant increment $\delta_C =$ 50 MPa was selected for all staircase tests. Initial staircase levels, specimen numbers, and the post hoc relative increment δ_C (%)—defined as δ_C (MPa) normalized by the evaluated $\sigma_{A,P=50\%}$ (MPa) of the staircase regime—are reported for each S–N curve in Tables S7 (D2 steels) and S8 (V10 steels) of the Supporting Information (SI). Across all batches, the chosen stair-step size $\delta_C =$ 50 MPa corresponded to $\delta_C \approx$ 4%–11%, i.e., within the recommended range (minimum $\delta_C \approx$ 5%–10% of the expected $\sigma_{A,P=50\%}$) for materials with pronounced fatigue scatter.

The SFSA workflow proposed by Scholl et al. [90, 91, 97–100] was applied using a scanning electron microscope (SEM) and energy-dispersive X-ray spectroscopy (EDS) to determine geometric and chemical properties of critical intrinsic defects. A detailed step-by-step SFSA flowchart is provided in Figure S9. Representative critical defects and associated geometric measurements at selected hardness levels are illustrated for D2 in Figure 9 and for V10 in Figure 10. For V10 PM-L[1], Figure 11 illustrates the EDS-based chemical defect classification at selected hardness levels; further examples are given for V10 PM-L[2] in Figure S10 and for V10 PM-L[3] in Figure S11.

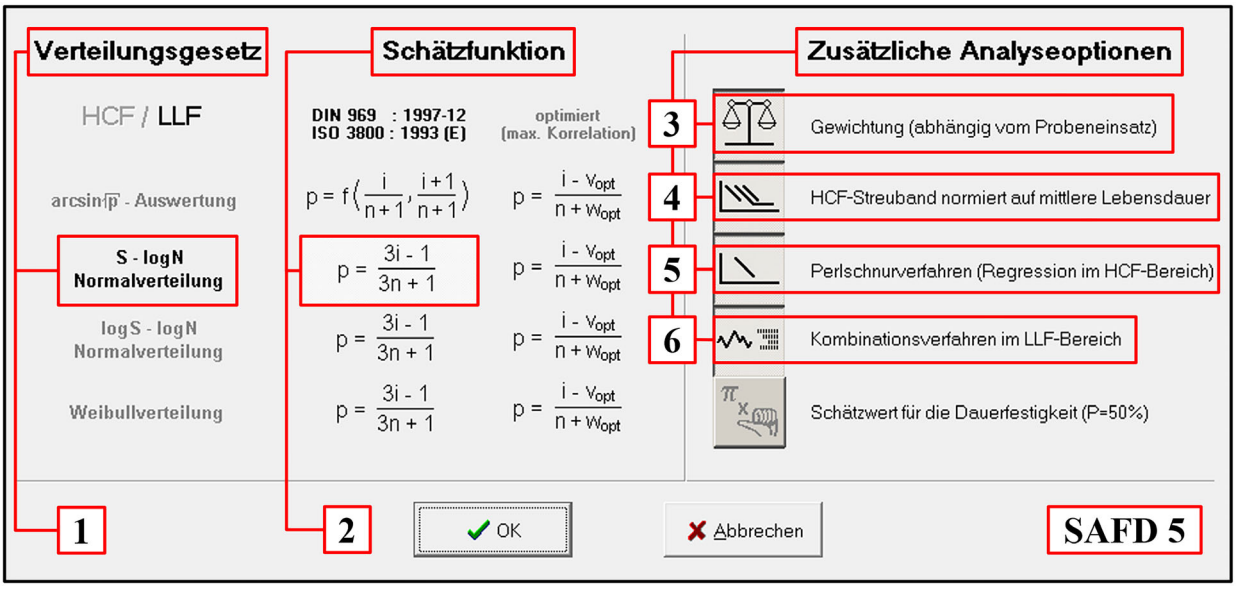

FIGURE 8 | SAFD 5 settings used for statistical evaluation of fatigue data following Klubberg et al. [154] and DIN 50100:2022-12 [153]. Key selections: (1) distribution law—simple Gaussian distribution in S–log N; (2) estimator—Rossow [155] (no optimization/max. correlation); for LLF—(3) weighting and (6) combination method according to Klubberg et al. [154]; for SLF—(4) scatter band normalized to $\overline{N}_{Fracture}$ and (5) pearl-string method (linear regression).

1869344x, 2026, 10, Downloaded from https://onlinelibrary.wiley.com/doi/10.1002/srin.202501039 by Universitatsbibliothek RWTH Aachen University, Wiley Online Library on [05/11/2026]. See the Terms and Conditions (https://onlinelibrary.wiley.com/terms-and-conditions) on Wiley Online Library for rules of use; OA articles are governed by the applicable Creative Commons License

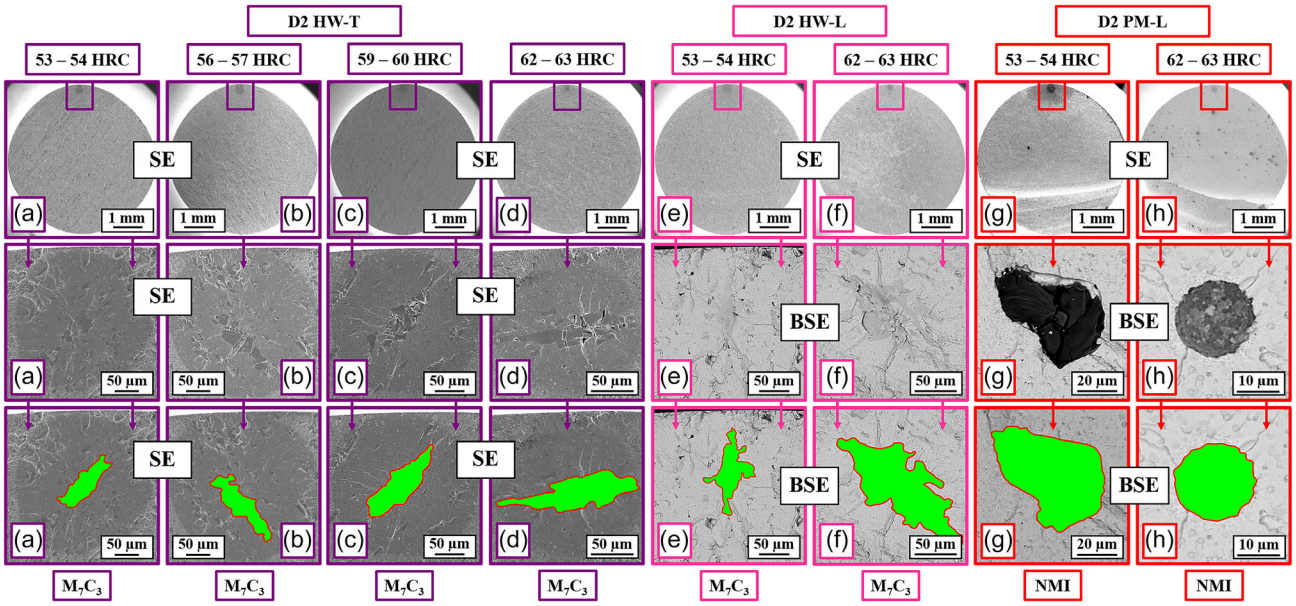

FIGURE 9 | Statistical fracture-surface analysis (SFSA) workflow for acquiring geometric properties of crack-initiating defects from SEM images, following Scholl et al. [90, 91, 97–100]. Representative critical defects are shown for D2 HW-T (M_7C_3 carbides) at (a) 53–54 HRC, (b) 56–57 HRC, (c) 59–60 HRC, and (d) 62–63 HRC; for D2 HW-L (M_7C_3 carbides) at (e) 53–54 HRC and (f) 62–63 HRC; and for D2 PM-L (NMI) at (g) 53–54 HRC and (h) 62–63 HRC. The last image row illustrates the image-processing–based measurements of defect geometry parameters (e.g., area A to calculate $\sqrt{}$area) used to develop the statistical defect–property database.

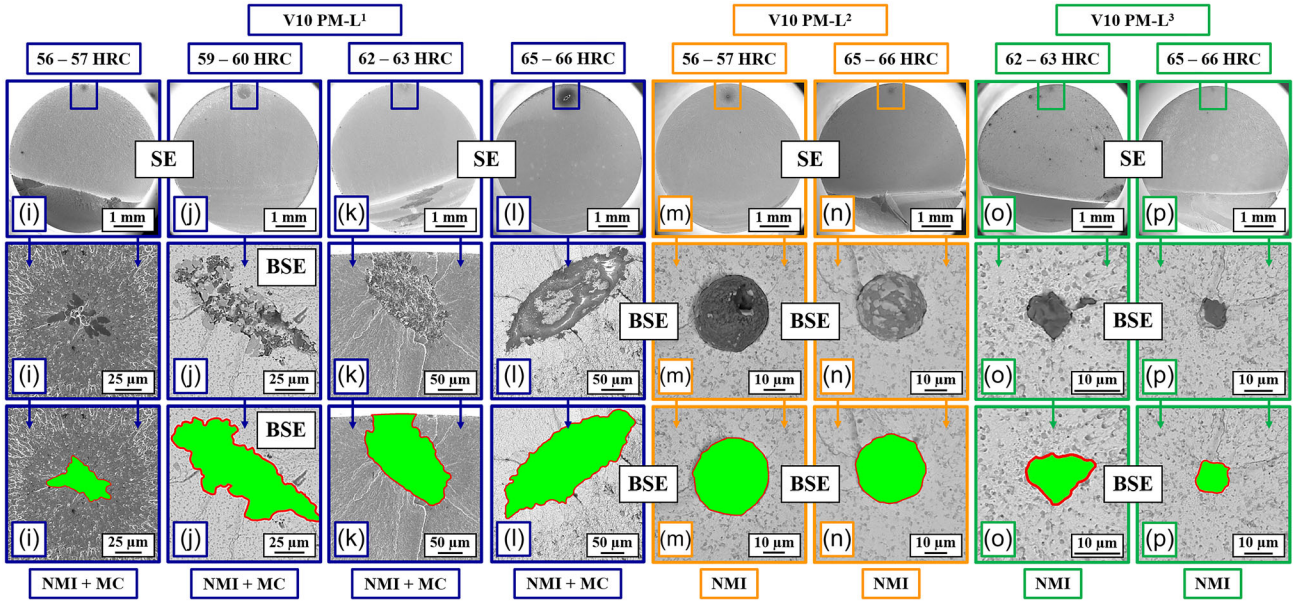

FIGURE 10 | Statistical fracture-surface analysis (SFSA) workflow for acquiring geometric properties of crack-initiating defects from SEM images, following Scholl et al. [90, 91, 97–100]. Representative critical defects are shown for V10 PM-L^1 (agglomerates of NMI + MC carbides) at (i) 56–57 HRC, (j) 59–60 HRC, (k) 62–63 HRC, and (l) 65–66 HRC; for V10 PM-L^2 (NMI) at (m) 56–57 HRC and (n) 65–66 HRC; and for V10 PM-L^3 (NMI) at (o) 62–63 HRC and (p) 65–66 HRC. The last image row illustrates the image-processing–based measurements of defect geometry parameters (e.g., area A to calculate $\sqrt{}$area) used to develop the statistical defect–property database.

SFSA was performed as follows: After fracture, fatigue specimens were removed from the machines and stored in plastic bags with volatile corrosion inhibitor (VCI) to protect fracture surfaces from corrosion and humidity prior to analysis. For analysis, both halves of each fractured fatigue specimen were cut ~10 mm below the fracture-surface and cleaned with alcohol using a fine brush similar to a toothbrush to remove remaining dust or other particles. Fracture surfaces were examined using a JEOL-JSM-6500 SEM equipped with an EDS detector to identify crack initiation sites and characterize each individual crack initiator (Figures 9–11). Defect boundaries were manually segmented on SEM images using image-processing

1869344x, 2026, 10, Downloaded from https://onlinelibrary.wiley.com/doi/10.1002/srin.202501039 by Universitatsbibliothek RWTH Aachen University, Wiley Online Library on [05/11/2026]. See the Terms and Conditions (https://onlinelibrary.wiley.com/terms-and-conditions) on Wiley Online Library for rules of use; OA articles are governed by the applicable Creative Commons License

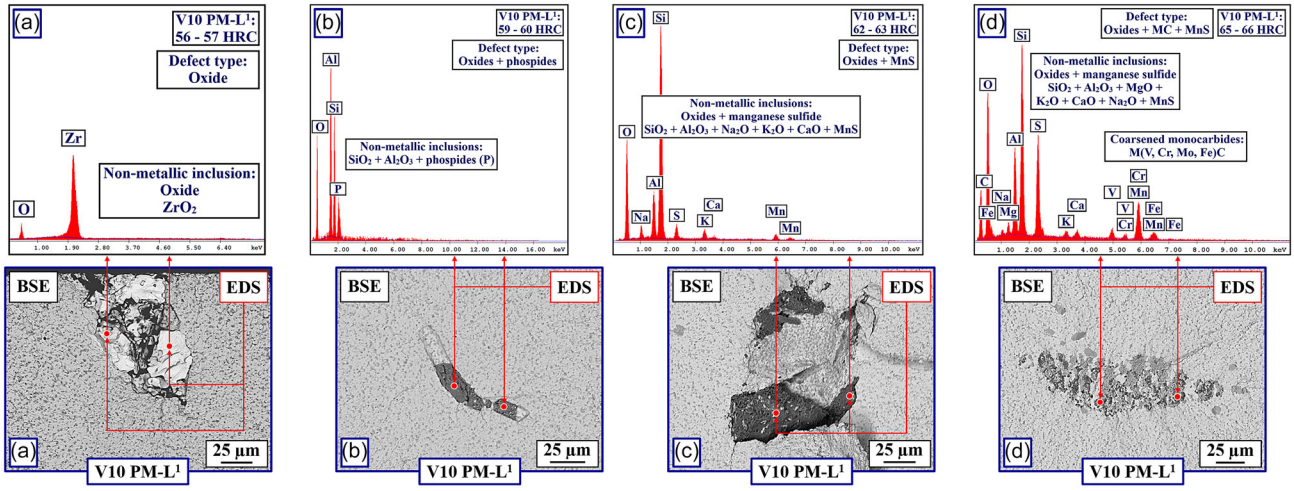

FIGURE 11 | EDS-based chemical classification within the SFSA workflow for V10 PM-L[1]. SEM images with EDS spectra acquired at marked locations are shown for representative crack-initiating defects at (a) 56–57 HRC: ZrO_2 inclusion; (b) 59–60 HRC: multiphase oxide with P-containing constituents (e.g., phosphides and/or phosphates); (c) 62–63 HRC: multiphase oxide–MnS agglomerate; and (d) 65–66 HRC: multiphase oxide–MnS–MC agglomerate containing strongly coarsened MC carbide clusters.

software (Figures 9 and 10), and the numerical values of each geometric parameter were calculated and transferred to the database. The most relevant geometric parameter was the defect area A (µm^2) obtained by projecting the defect onto the plane vertical to the maximum principal normal stress, which is the fracture-surface plane; $\sqrt{\text{area}}$ (µm) was then calculated according to Murakami [116, 118]. In addition, the 2D shape factors circularity (Cir) and roundness (Ro), the perimeter (Per), the Feret diameter (Fer), the defect position (surface, contact or volume), and the distance d_S (µm) from the surface edge fiber were determined.

Chemical composition was determined by systematic EDS point measurements as exemplarily shown in Figure 11 (see also Figures S10 and S11); up to approx. ten main constituent elements were recorded per defect based on indexed EDS peaks. The resulting datasets were merged and sorted across all specimens, batches, fatigue results, and defect characteristics to build the manufacturing- and hardness-resolved database for carbide-rich, high-alloy CWS.

2.5 | Statistical Fatigue–Strength and Defect–Property Database for Systematic Validations

Using statistical fatigue testing, the SFSA workflow, and systematic data collection and preprocessing, a fatigue–strength and defect–property database was established for six carbide-rich CWS configurations at four to five application-relevant macrohardness levels. This database provides the experimental baseline for the main objectives of this study. The database contains, for each individual specimen, the fatigue-test outcome and the associated critical-defect information, including geometric parameters, chemical classification, and defect location. In total, >1,200 specimens from six CWS batches were fatigue-tested across the selected hardness levels, yielding >51,000 individual data entries from RBT, SFSA (including EDS), and subsequent model-validation results. To evaluate Murakami's [116, 118] mechanics-of-small-cracks approach, the $\sqrt{\text{area}}$ model was applied to the statistical database and normalized S–N curves were derived over a broad range of macrohardness, defect sizes/types, and carbide contents. The implementation used here follows Equations (10)–(13) and enables direct, specimen-wise application to the database.

Murakami's [116, 118] semi-empirical, fracture-mechanics-based formulation relates σ_w (MPa) to defect size $\sqrt{\text{area}}$, hardness, and defect location via the stress intensity factor (SIF) threshold range $\Delta K_{th,Murakami}$ (MPa·$\sqrt{\text{m}}$) and the SIF range $\Delta K_{I,Murakami}$ (MPa·$\sqrt{\text{m}}$) under LEFM and mode I (stage II) fatigue crack growth. In Equations (10) and (11), the fatigue limit $\sigma_{w,Murakami}$ (MPa) is expressed as a function of $\sqrt{\text{area}}$ (µm), the stress ratio R (–), the Vickers hardness H_V, and a location-dependent factor K (–). The hardness-dependent exponent $\alpha_{Murakami}$ (–), required for the mean stress sensitivity ($R \neq -1$), is calculated according to Equation (12); however, because all fatigue tests and accuracy evaluations were performed at $R = -1$ in this work, $\alpha_{Murakami}$ can be omitted here. Normalized S–N curves are obtained from the exp. data using Equation (13), where the normalized stress $\sigma_{Normalized}$ or σ_N (–) is defined relative to the applied (nominal) test stress amplitude $\sigma_{a,Testing}$ (MPa).

For surface (S) or contact (C) defects (defect location factor $K_S = 1.43$, $K_C = 1.41$):

$$\sigma_{w,Murakami}\,(\text{MPa}) = \frac{K_{S/C} \cdot (H_V + 120)}{\left(\sqrt{\text{area}_{S/C}}\right)^{\frac{1}{6}}} \cdot \left[\frac{1-R}{2}\right]^{\alpha} \qquad (10)$$

For internal volume (V) defects (defect location factor $K_V = 1.56$):

$$\sigma_{w,Murakami}\,(\text{MPa}) = \frac{K_V \cdot (H_V + 120)}{\sqrt{\text{area}_V}^{\frac{1}{6}}} \cdot \left[\frac{1-R}{2}\right]^{\alpha} \qquad (11)$$

1869344x, 2026, 10, Downloaded from https://onlinelibrary.wiley.com/doi/10.1002/srin.202501039 by Universitatsbibliothek RWTH Aachen University, Wiley Online Library on [05/11/2026]. See the Terms and Conditions (https://onlinelibrary.wiley.com/terms-and-conditions) on Wiley Online Library for rules of use; OA articles are governed by the applicable Creative Commons License

For $R \neq -1$ (consideration of hardness-dependent mean stress influences on the fatigue limit):

$$\alpha_{\text{Murakami}}\,(-) = 0.226 + H_V \cdot 10^{-4} \tag{12}$$

For S–N curve normalization (for fractures it should apply $\sigma_N \geq 1 \pm 0.1$ for the $\pm 10\%$ model accuracy):

$$\sigma_{\text{Normalized}}\,(-) = \frac{\sigma_{a,\text{Testing}}}{\sigma_{w,\text{Murakami}}} \left(\text{here: } \sigma_N\,(-) = \frac{\sigma_{\text{Local}}}{\sigma_{w,\text{Murakami}}} \right) \tag{13}$$

The local stress σ_{Local} or σ_L (MPa) at a critical (volume) defect under RBT, for which location holds $z_{\text{defect}} < z_{\max}$, is calculated using a rule-of-three relationship (the surface edge fiber is defined as $z_{\max}$ (µm) = $d_{\text{cross-section}}/2$ with corresponding $\sigma_{a,\text{Testing}}$ = fatigue test stress at $z_{\max}$; for the critical volume defect is defined d_S (µm) = distance to the surface edge fiber):

$$\sigma_{\text{Local}}\,(\text{MPa}) = f(z) = \frac{\sigma_{a,\text{Testing}}}{z_{\max}} \cdot (z_{\max} - d_S) \tag{14}$$

Under axial loading, the nominal stress amplitude $\sigma_{a,\text{Testing}}$ is essentially uniform across the specimen cross-section and therefore equals the local stress amplitude σ_L at a critical defect. This equivalence does not hold for non-uniform stress fields such as rotating-/flat-bending or torsion. For RBT, σ_L was therefore determined specimen-wise from $\sigma_{a,\text{Testing}}$ and the measured defect depth parameter d_S following Equation (14) by using the linear stress gradient across the cross-section (rule-of-three relationship). For deriving normalized S–N curves and PSPP correlations in the following, σ_L was used for each specimen and its critical defect instead of $\sigma_{a,\text{Testing}}$ to improve accuracy for near-surface and internal defects.

3 | Results

This section presents the exp. and database-derived results of this study. Statistically evaluated LLF strengths, $\sigma_{A,P=1\%-99\%}$ (MPa), are reported for all investigated carbide-rich CWS across 45/53/56–66 HRC, together with the associated LLF scatter bands and normalized S–N curves. The result section is organized as follows:

First, the exp. fatigue data, statistically evaluated LLF strengths, and the resulting conventional and normalized S–N curves are presented. Next, the statistical evaluation of geometric and chemical characteristics of crack-initiating defects from SFSA is summarized and compared with CGA results (metallographic plane-by-plane inspections) according to ASTM E2283-08R19 [146]. Subsequently, PSPP correlations (including defect-size-controlled hardness effects) are derived by linking the critical-defect and fatigue–strength databases. Representative fiRS measurement results (surface values and depth profiles) are then presented and discussed to quantify their influence on fatigue strength and the observed hardness trends. Finally, database-driven accuracy validations of Murakami's [116, 118] fatigue model are reported. Together with the normalized S–N curves, these results are used to assess the derived PSPP correlations and apparent hardness trends by comparison with classical reference data for artificial surface defects from Murakami and Endo [116, 118, 119].

For all evaluated S–N curves (type I evaluation with SAFD 5), the corresponding normalized S–N curves, and the database-derived PSPP correlations, filled circles denote run-outs (survivors), open circles denote direct fractures, and open triangles denote upstaired fractures. In the conventional S–N plots, small colored numbers next to run-outs indicate their count at the corresponding staircase stress level (see Section 2.4). When comparing fatigue test batches, the most robust and least error-prone metric is the staircase mean $\sigma_{A,P=50\%}$, because, according to DIN 50100:2022-12 [153], statistical evaluation uncertainties are small for the mean (about $\pm 3\%$–4% for batch sizes of ~30–66 specimens used here, assuming the SD is ~0.05) but much larger for the distribution tails (about +40%–80% and −30%–45% error for the estimated scatter bounds at $P = 1\%$–10% and 90%–99%, respectively). Therefore, direct batch comparisons are primarily based here on $\sigma_{A,P=50\%}$ rather than on $\sigma_{A,P=1\%-10\%}$ or $\sigma_{A,P=90\%-99\%}$.

3.1 | Statistically Evaluated LLF Strengths and Derived S–N Curves

The exp. fatigue results are presented as statistically evaluated conventional S–N curves (median fit only) in Figure 12a–d for the D2 steels and Figure 13a–d for the V10 steels. For each condition, the corresponding database-derived normalized S–N curve is shown on the right-hand side (D2: Figure 12e–h; V10: Figure 13e–h). The underlying LLF strength distributions $\sigma_{A,P=1\%-99\%}$ and the associated abs./rel. LLF scatter band sizes are compiled for the D2 steels in Table 9 and for the V10 steels in Table 10.

The corresponding distributions of $\sigma_{A,P}$ versus failure probability P are compared at each hardness level in Figure S12a–f. Relative differences (percentage) in the median LLF strength $\sigma_{A,P=50\%}$ between materials at a given hardness are summarized in Table S9. For D2, the results show strong effects of steelmaking route and pronounced anisotropy for the IC material. Across all investigated hardness levels, D2 PM-L exhibits markedly higher LLF strength than the IC configurations D2 HW-L/-T (Figures 12a–d and S12a–d; Tables 9 and S9). Specifically, D2 PM-L achieves about 55%–69% higher $\sigma_{A,P=50\%}$ than D2 HW-L and about 86%–115% higher $\sigma_{A,P=50\%}$ than D2 HW-T (Tables 9 and S9). The IC steel D2 exhibits pronounced mechanical anisotropy, quantified here as the anisotropy index/indices (AI) according to Equation (15). For D2 IC, the resulting AI (–) values increase strongly with hardness: $AI_{53-54\text{HRC}} \approx 15.6\%$, $AI_{56-57\text{HRC}} \approx 14.3\%$, $AI_{59-60\text{HRC}} \approx 21.1\%$, and $AI_{62-63\text{HRC}} \approx 38.6\%$. This behavior is consistent with an RHE-type reversal in D2 HW-T that is not observed for D2 HW-L and D2 PM-L. As outlined in Section 1 (cf. Figures 2–4), this reversal is defect-size-controlled, i.e., governed by the extreme-value distribution of intrinsic defects, and is analyzed in detail later using the database-derived PSPP correlations (Sections 3.4, 4.1, and 4.3).

$$AI\,(-) = \frac{\sigma_{A,P=50\%,\text{HW-L}}}{\sigma_{A,P=50\%,\text{HW-T}}} - 1 \tag{15}$$

Significant LLF strength differences also occur among the V10 PM-L grades (Figure 13a–d; Tables 10 and S9). The highest LLF performance is consistently obtained for the very clean

1869344x, 2026, 10, Downloaded from https://onlinelibrary.wiley.com/doi/10.1002/srin.202501039 by Universitatsbibliothek RWTH Aachen University, Wiley Online Library on [05/11/2026]. See the Terms and Conditions (https://onlinelibrary.wiley.com/terms-and-conditions) on Wiley Online Library for rules of use; OA articles are governed by the applicable Creative Commons License

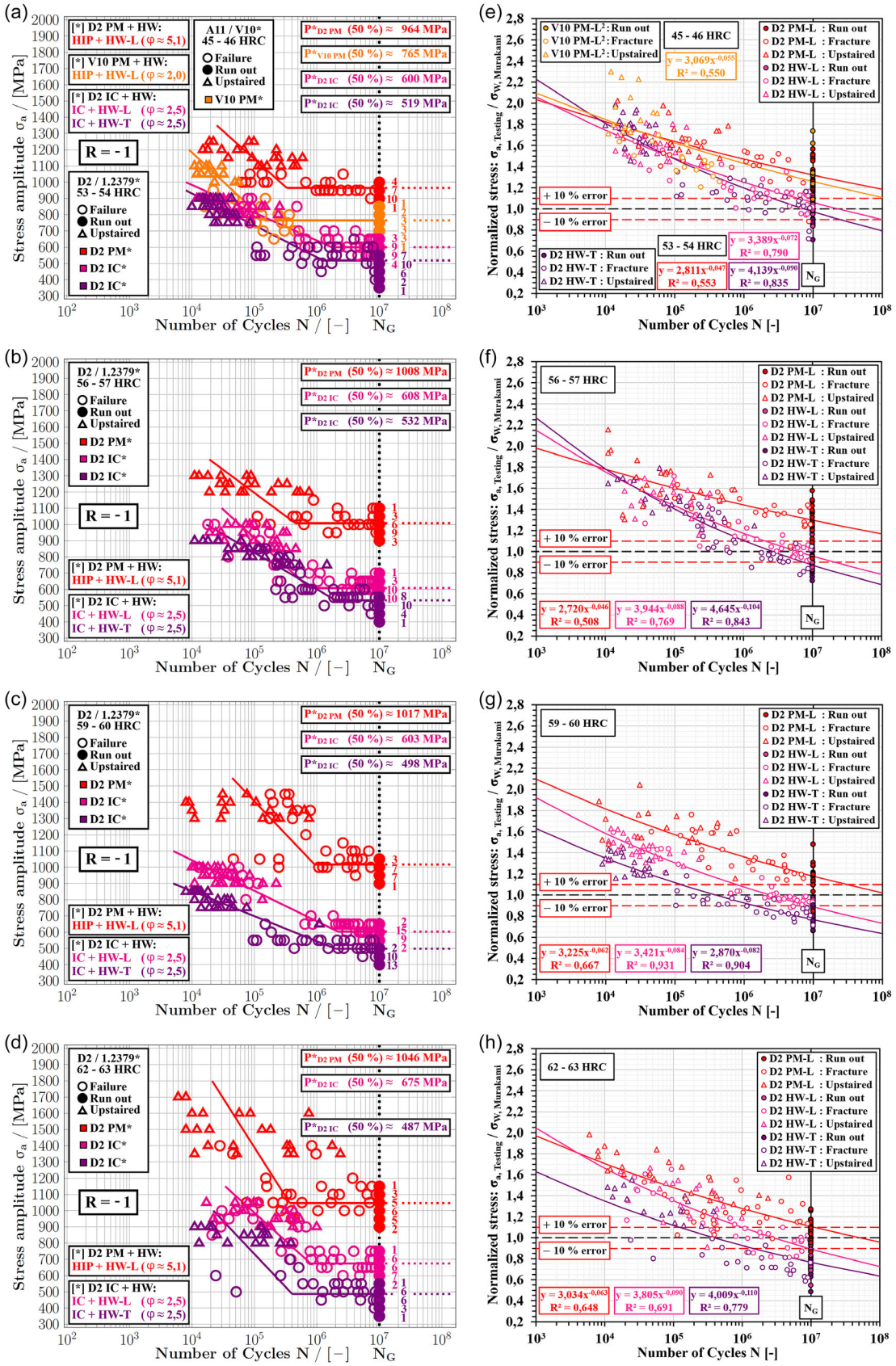

FIGURE 12 | Exp. fatigue data for D2 PM-L, D2 HW-L, D2 HW-T (53–63 HRC), and V10 PM-L^2 (45–46 HRC). The left panels show conventional S–N curves evaluated with SAFD 5, including the median fit line for $\sigma_{A,P=50\%}$. Conditions: (a) 53–54 HRC (D2)/45–46 HRC (V10 PM-L^2); (b) 56–57 HRC (D2); (c) 59–60 HRC (D2); and (d) 62–63 HRC (D2). The right panels show the corresponding normalized S–N curves derived from Equations (10)–(14) according to Murakami [116, 118], with power-law fits (solid lines) including fit equations and coefficients of determination R^2 (–): (e) 53–54 HRC (D2)/45–46 HRC (V10 PM-L^2); (f) 56–57 HRC (D2); (g) 59–60 HRC (D2); and (h) 62–63 HRC (D2).

1869344x, 2026, 10, Downloaded from https://onlinelibrary.wiley.com/doi/10.1002/srin.202501039 by Universitatsbibliothek RWTH Aachen University, Wiley Online Library on [05/11/2026]. See the Terms and Conditions (https://onlinelibrary.wiley.com/terms-and-conditions) on Wiley Online Library for rules of use; OA articles are governed by the applicable Creative Commons License

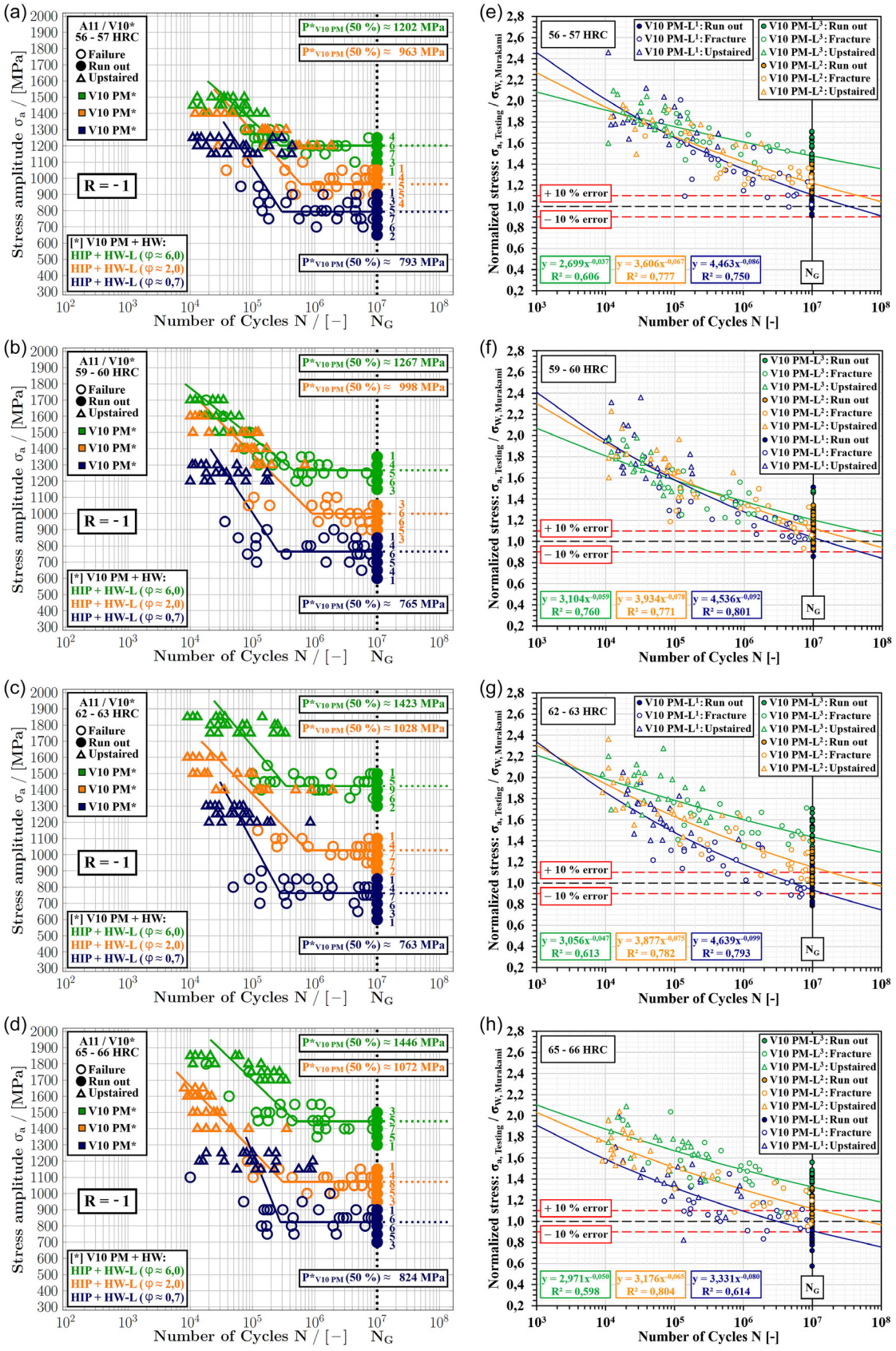

FIGURE 13 | Exp. fatigue data for V10 PM-L[1], V10 PM-L[2], and V10 PM-L[3] (56–66 HRC). The left panels show conventional S–N curves evaluated with SAFD 5, including the median fit line for $\sigma_{A,P=50\%}$: (a) 56–57 HRC; (b) 59–60 HRC; (c) 62–63 HRC; and (d) 65–66 HRC. The right panels show the corresponding normalized S–N curves derived from Equations (10)–(14) according to Murakami [116, 118], with power-law fits (solid lines) including fit equations and coefficients of determination R^2 (–): (e) 56–57 HRC; (f) 59–60 HRC; (g) 62–63 HRC; and (h) 65–66 HRC.

1869344x, 2026, 10, Downloaded from https://onlinelibrary.wiley.com/doi/10.1002/srin.202501039 by Universitatsbibliothek RWTH Aachen University, Wiley Online Library on [05/11/2026]. See the Terms and Conditions (https://onlinelibrary.wiley.com/terms-and-conditions) on Wiley Online Library for rules of use; OA articles are governed by the applicable Creative Commons License

TABLE 9 | Statistical LLF strengths $\sigma_{A,P}$ (MPa) for RBT at $N_G = 10^7$ cycles of the D2 steels as a function of failure probability P (%) and macrohardness (HRC), evaluated with SAFD 5.

Steel	Hardness (HRC)	Fatigue strength $\sigma_{A,P}$ (MPa) for RBT							Scatter band	
		$\sigma_{A,P=1\%}$	$\sigma_{A,P=5\%}$	$\sigma_{A,P=10\%}$	$\sigma_{A,P=50\%}$	$\sigma_{A,P=90\%}$	$\sigma_{A,P=95\%}$	$\sigma_{A,P=99\%}$	Abs. (MPa)	Rel. (%)
D2 HW-L	53–54	394	454	486	600	714	746	806	206	34.3
	56–57	328	410	454	608	762	806	888	280	46.1
	59–60	482	518	537	603	670	689	725	122	20.1
	62–63	443	511	547	675	802	838	906	232	34.3
D2 HW-T	53–54	325	382	412	519	625	655	712	194	37.3
	56–57	401	440	460	532	604	624	663	131	24.6
	59–60	416	440	453	498	544	557	581	83	16.6
	62–63	289	347	378	487	596	627	685	198	40.7
D2 PM-L	53–54	821	863	885	964	1042	1065	1107	143	14.8
	56–57	732	813	856	1008	1160	1203	1284	276	27.4
	59–60	868	911	935	1017	1099	1123	1166	149	14.7
	62–63	656	770	831	1046	1261	1322	1436	390	37.3

TABLE 10 | Statistical LLF strengths $\sigma_{A,P}$ (MPa) for RBT at $N_G = 10^7$ cycles of the V10 steels as a function of failure probability P (%) and macrohardness (HRC), evaluated with SAFD 5.

Steel	Hardness (HRC)	Fatigue strength $\sigma_{A,P}$ (MPa) for RBT							Scatter band	
		$\sigma_{A,P=1\%}$	$\sigma_{A,P=5\%}$	$\sigma_{A,P=10\%}$	$\sigma_{A,P=50\%}$	$\sigma_{A,P=90\%}$	$\sigma_{A,P=95\%}$	$\sigma_{A,P=99\%}$	Abs. (MPa)	Rel. (%)
V10 PM-L[1]	56–57	390	515	581	816	1050	1117	1242	426	52.2
	59–60	452	544	593	765	937	986	1077	313	40.8
	62–63	487	568	611	763	915	959	1040	277	36.2
	65–66	535	619	665	824	983	1028	1113	289	35.1
V10 PM-L[2]	45–46	374	488	550	765	981	1042	1157	392	51.2
	56–57	551	671	736	963	1189	1254	1374	412	42.7
	59–60	633	740	797	998	1199	1256	1363	365	36.6
	62–63	786	857	895	1028	1162	1200	1271	243	23.6
	65–66	729	830	883	1072	1261	1314	1414	343	31.9
V10 PM-L[3]	56–57	971	1039	1075	1202	1330	1366	1434	232	19.3
	59–60	947	1041	1091	1267	1443	1493	1587	320	25.3
	62–63	1203	1267	1302	1423	1545	1579	1644	221	15.5
	65–66	1195	1268	1307	1446	1584	1623	1696	251	17.3

V10 PM-L[3], which exhibits the maximum $\sigma_{A,P=50\%}$ across the studied hardness levels (Tables 10 and S9). V10 PM-L[3] achieves about 47%–87%, 25%–38%, and 19%–36% higher $\sigma_{A,P=50\%}$ than V10 PM-L[1], V10 PM-L[2], and D2 PM-L, respectively (Tables 9, 10, and S9; Figures 12, 13, and S12a–f). D2 PM-L and V10 PM-L[2] perform similarly, with D2 PM-L only about 2%–5% higher in $\sigma_{A,P=50\%}$ (Table S9). Compared with V10 PM-L[1], D2 PM-L and V10 PM-L[2] show about 24%–37% and 18%–35% higher $\sigma_{A,P=50\%}$, respectively (Table S9).

Overall, the four PM-HIP steels exhibit substantially higher LLF strengths under RBT than the D2 IC steel at comparable hardness, and even the intentionally less clean V10 PM-L[1] still exceeds D2 HW-L by about 13%–34% in $\sigma_{A,P=50\%}$ (Tables 9, 10, and S9). For the studied carbide-rich CWS, these differences cannot be attributed to alloy composition or macrohardness (nearly identical compositions and identical HT schedules), but instead reflect manufacturing-induced defect populations and associated microstructural characteristics.

Hardness sensitivities differ strongly among the investigated steels (Figure S12f; Tables 9, 10, and S9). Over the studied hardness ranges, $\sigma_{A,P=50\%}$ increases by about 12.5% for D2 HW-L (53–63 HRC), about 20.3% for V10 PM-L[3] (56–66 HRC), and about 40.1% for V10 PM-L[2] (45–66 HRC). In contrast, D2 PM-L and V10 PM-L[1] show only about 8.5% (53–63 HRC) and 1.0% (56–66 HRC) increases, respectively. A distinct behavior is observed for D2 HW-T: $\sigma_{A,P=50\%}$ increases slightly (about

1869344x, 2026, 10, Downloaded from https://onlinelibrary.wiley.com/doi/10.1002/srin.202501039 by Universitatsbibliothek RWTH Aachen University, Wiley Online Library on [05/11/2026]. See the Terms and Conditions (https://onlinelibrary.wiley.com/terms-and-conditions) on Wiley Online Library for rules of use; OA articles are governed by the applicable Creative Commons License

2.5%) from about 53–57 HRC and then decreases (about 8.5%) from about 57–63 HRC (Figure 12a–d; Tables 9 and S9), consistent with an RHE-type reversal (Sections 1, 3.4, 4.1, and 4.3).

The normalized S–N curves (D2: Figure 12e–h; V10: Figure 13e–h) exhibit acceptable power-law fits across all conditions. Fit accuracies range from $R^2 \approx 0.51$–0.93 for the D2 steels and $R^2 \approx 0.55$–0.80 for the V10 steels. In most cases, R^2 is slightly higher for the D2 IC series ($R^2 \approx 0.69$–0.93) than for the PM-HIP series ($R^2 \approx 0.51$–0.80), with some exceptions (Figures 12e–h and 13e–h). Overall, the conventional and normalized S–N curve representations (Figures 12, 13, and S12; Tables 9, 10, and S9) demonstrate substantial differences among the investigated carbide-rich CWS.

Steel manufacturing (carbide size scale, cleanliness, HW) and subsequent HT (hardness) exert dominant influences on the LLF performance; however, observed hardness trends, anisotropy, and apparent RHE behavior require interpretation in the context of SFSA-based critical-defect statistics (size, shape, location, chemistry) and superimposed surface-integrity effects (from fiCRS), which is addressed in the following subsections (Sections 3.2–3.6).

3.2 | Statistically Evaluated Geometric and Chemical Properties of Crack-Initiating Defects

Crack-initiating (critical) intrinsic defects were identified on fracture surfaces after RBT and quantified using the SFSA workflow. The resulting geometric defect statistics are summarized in Figure 14 as mean values with SD for each steel batch and hardness level: Figure 14a reports the defect size as $\sqrt{area}$ according to Murakami [116, 118], and Figure 14b reports the defect shape via the 2D circularity factor. A detailed summary of the mean defect sizes $\sqrt{area}_{mean}$ shown in Figure 14, together with the corresponding minimum and maximum values ($\sqrt{area}_{min}$ and $\sqrt{area}_{max}$), is provided for each steel batch and hardness level in Table S10.

Overall, the defect–property database shows a consistent size–strength relationship across all steels. The very clean V10 PM-L^3 exhibits the smallest crack-initiating defects and the lowest size scatter, consistent with its highest LLF strengths $\sigma_{A,P=50\%}$ (Tables 9, 10, S9, and S10; Figures 12–14, S11, and S12b–f). D2 PM-L and V10 PM-L^2 show the second-smallest (and very similar) defect size levels with comparable SD, consistent with their similarly high $\sigma_{A,P=50\%}$ values (Tables 9, 10, S9, and S10; Figures 12–14, and S12a–d).

In contrast, V10 PM-L^1 contains markedly larger critical defects than the other PM-HIP grades, resulting in significantly lower LLF strengths $\sigma_{A,P=50\%}$ (Figures 10j–l, 11–14, and S12b–e; Tables 9, 10, S9, and S10). For the D2 IC steel, D2 HW-T exhibits the largest defect sizes (on average and often also in the min. values), consistent with its lowest LLF strengths at all hardness levels, whereas D2 HW-L shows slightly smaller critical defects than D2 HW-T.

Noteworthy, V10 PM-L^1 still achieves higher $\sigma_{A,P=50\%}$ than D2 HW-L/-T, although its mean $\sqrt{area}$ values ($\sqrt{area}_{mean}$) are

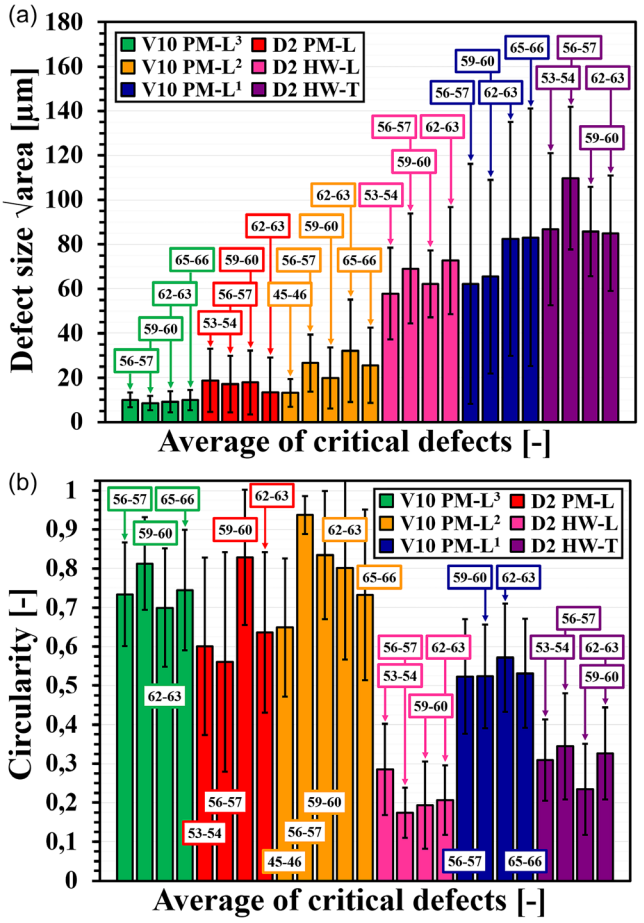

FIGURE 14 | Statistical evaluation of geometric properties of crack-initiating defects/agglomerates determined by SFSA for all D2 and V10 batches tested: (a) defect size $\sqrt{area}$ according to Murakami [116, 118] and (b) 2D circularity factor (Cir). Results are shown as mean values with SD for each batch population (statistical size data is summarized in Table S10; specimen counts are given in Tables S7 and S8).

comparable to—and in some cases exceed—those of D2 HW-L (Figure 14a; Tables S5, S6 and S10). This apparent inconsistency is resolved when considering defect-size scatter and extremes: V10 PM-L^1 exhibits the largest scatter and the largest $\sqrt{area}$ maxima ($\sqrt{area}_{max}$) across the investigated hardness levels (Figure 14a; Table S10), reflecting occasional very large multiphase agglomerates that include oxidic NMIs, coarsened MC carbides/clusters and MnS (Figures 10j–l and 11). Thus, mean defect size alone is not sufficient: V10 PM-L^1 also exhibits smaller $\sqrt{area}$ minima ($\sqrt{area}_{min}$) than D2 HW-L/-T (M_7C_3 carbides), and the breadth of the extreme-value distribution is critical for interpreting LLF behavior and subsequent PSPP correlations.

Defect morphology further differentiates IC and PM-HIP steels. The PM-HIP grades generally show rounder crack initiators (higher Cir), whereas the D2 IC steel shows much lower Cir values because crack initiation occurs at blocky, irregular M_7C_3 carbides (Figures 6a–d,i, and 9a–f; Table 11). Among the PM-HIP steels, V10 PM-L^1 differs from V10 PM-$L^{2/3}$ and D2 PM-L by lower average Cir values and larger shape scatter, consistent with its higher fraction of irregular multiphase agglomerates (Figures 10j–l, 11, and 14b; Table 11). Taken together, the

1869344x, 2026, 10, Downloaded from https://onlinelibrary.wiley.com/doi/10.1002/srin.202501039 by Universitatsbibliothek RWTH Aachen University, Wiley Online Library on [05/11/2026]. See the Terms and Conditions (https://onlinelibrary.wiley.com/terms-and-conditions) on Wiley Online Library for rules of use; OA articles are governed by the applicable Creative Commons License

combined statistics of defect size (mean with SD, minimum and maximum extreme sizes; Figure 14a; Table S10) and morphology (Figure 14b) provide a coherent explanation for the observed differences in $\sigma_{A,P=50\%}$ across steelmaking routes and batches.

In addition to geometry, EDS-based chemical classification was used to assign each crack initiator to generalized defect/agglomerate types. The statistical outcomes (summed over all hardness levels and batches per steel grade) are compiled in Table 11 together with the largest observed extremes ($\sqrt{area}_{max}$) and total sample counts. The classification in Table 11 is based on the EDS results for all critical defects identified by SFSA: the dominant elements detected in each defect were used to assign it to a chemical defect class, followed by statistical evaluation across each steel grade. Summary plots aggregated over all hardness levels are provided in Figure S13a–f.

A clear separation is observed between IC and PM-HIP steels. In D2 HW-L/-T, fatigue cracks initiated exclusively at eutectic M_7C_3 carbides (Cr-based special carbides with solubility for Fe, Mo, and V; Figures 9a–f and S13b,c; Table 11). In D2 PM-L, crack initiation occurred predominantly at oxidic NMIs, occasionally as oxide–MnS agglomerates (often surfaces partially covered), while coarsened M_7C_3 carbide clusters were not observed as crack initiators in D2 PM-L under the present PM-HIP conditions (Figures 9g–h and S13a; Table 11).

Consistently, the SFSA/EDS results show that D2 PM-L crack initiators always contain oxygen and oxide formers (e.g., Al, Si, Mg, Ca), with MnS occasionally present as an agglomerated constituent; however, the dominant defect volumes are oxidic NMI (Figures 9g–h, S13a; Table 11). Owing to the low V content of D2 compared to V10 (<1 wt.%) and the high cooling rates during powder atomization, D2 PM-L contains only very small, near-spherical M_7C_3 carbides with a homogeneous spatial distribution (Figure 6e–h), and coarsened M_7C_3 carbides or clusters were not observed as crack initiators (Figures 9g–h and S13a).

The V-rich PM-HIP grades show more complex crack-initiator populations. V10 PM-L[1] exhibits a broad spectrum of multiphase agglomerates dominated by oxidic NMIs (typical oxide formers such as Al, Si, Mg, Ca, Na, and K; occasionally also ZrO_2), frequently combined with MnS, P-containing constituents (phosphides and/or phosphates), and—in the most detrimental cases—strongly coarsened MC carbides/clusters (Figures 10i–l, 11a–d, S4, S5, and S13d; Table 11). These agglomerates are often very large (Figures 10j–l and 11a–d), particularly when coarsened MC carbides/clusters occur together with MnS (Figures 10j–l and 11d). Smaller crack initiators occur in V10 PM-L[1] when only a smaller, single oxidic NMI or an oxide–P-containing NMI is present (Figure 11b). A subset of V10 PM-L[1] agglomerates consists of oxidic NMIs with MC carbides/clusters where both the NMI fraction and (surrounding) MC clustering/coarsening are less pronounced (Figure 10i).

V10 PM-L[2] shows chemically similar initiator classes (oxides with MnS and/or P-containing constituents; oxide–MC agglomerates; and occasionally MC-only initiators; Figures 10m–n, S10, and S13e; Table 11), but differs in the size and frequency of the largest agglomerates, consistent with its higher LLF strength

TABLE 11 | Statistical summary of crack-initiating defect types (including agglomeration classes) identified by SFSA/EDS for all D2 and V10 steels (summed over macrohardness levels and batches), together with the largest observed extreme sizes/$\sqrt{area}$ values ($\sqrt{area}_{max}$) and total fatigue specimen counts.

Steel	Amount of each critical/crack-initiating defect type (%)							Largest critical defect size $\sqrt{area}_{max}$ (μm)	Total sample counts (–)
	Only oxide	Oxide + MC	Oxide + P	Oxide + MnS	Oxide + MC + MnS	Oxide + P + MnS	Oxide + MC + P + MnS	Only MC or M_7C_3	
D2 HW-L	—	—	—	—	—	—	—	100.0	≈103.5–134.6	245
D2 HW-T	—	—	—	—	—	—	—	100.0	≈137.1–202.5	201
D2 PM-L	75.3	—	—	24.7	—	—	—	—	≈59.0–114.6	190
V10 PM-L[1]	24.3	23.3	8.5	10.6	29.1	—	3.7	0.5	≈240.7–298.4	189
V10 PM-L[2]	14.4	21.0	—	22.6	1.5	30.3	1.0	9.2	≈30.7–109.9	195
V10 PM-L[3]	64.5	—	—	—	—	—	—	35.5	≈17.5–20.2	183

1869344x, 2026, 10, Downloaded from https://onlinelibrary.wiley.com/doi/10.1002/srin.202501039 by Universitatsbibliothek RWTH Aachen University, Wiley Online Library on [05/11/2026]. See the Terms and Conditions (https://onlinelibrary.wiley.com/terms-and-conditions) on Wiley Online Library for rules of use; OA articles are governed by the applicable Creative Commons License

relative to V10 PM-L[1]. In Figure S10a, MnS particles (light gray in BSE) are distinguishable from the oxidic NMI fraction (dark gray to black). The often round/spherical oxidic NMIs are agglomerated or partially mantled by MnS particles (Figures 10n, S10a, and S13e), and EDS spots on the light-gray particles show dominant S with secondary Mn peaks. Oxide–P-containing constituents with or without MnS are also observed in V10 PM-L[2] (Figure S10b,c; Table 11).

As in V10 PM-L[1] (Figure 10i), oxide–MC agglomerates occur in V10 PM-L[2] as well, and slightly coarsened MC carbides without NMI/MnS are also found as crack initiators (Figure S10d; Table 11). Less frequently, MC carbides/clusters may contain Ti or partly TiC (Figure S13d,e), more often in V10 PM-L[1] than in V10 PM-L[2]. Overall, while the chemical agglomeration classes are similar for V10 PM-L[1] and V10 PM-L[2], the size, shape, and frequency of the largest agglomerates differ; because extreme defect sizes are the most relevant FIF, V10 PM-L[2] performs better despite chemically comparable crack-initiator classes.

In contrast, the very clean V10 PM-L[3] steel exhibits only two separated initiator classes—small single oxidic NMIs and slightly coarsened single MC carbides—and no agglomerates involving MnS, P-containing constituents, or strongly coarsened MC clusters (Figures 10o,p, S11a,b, and S13f; Table 11). This is consistent with its smallest $\sqrt{}$area values (min., mean, and max.) and highest $\sigma_{A,P=50\%}$ (Figures 14 and S13f; Tables 11, S5, S6, S9, and S10). The high cleanliness during powder atomization together with the higher HW degree ($\varphi \approx 6.0$) result in a markedly more favorable defect state, most importantly substantially smaller and fewer oxidic NMIs, accompanied by strongly reduced MC coarsening and smaller extreme defect sizes.

These statistically evaluated defect–property results (size, morphology, and chemistry) provide the mechanistic basis for the PSPP correlations and the defect-size-controlled hardness trends (including RHE-related effects) developed and discussed in the subsequent Sections 3.3–3.5.

3.3 | Extreme-Value Distribution Comparison of Critical Defects Obtained by CGA Versus SFSA

Steel cleanliness is commonly defined in terms of the size, number, and spatial distribution of NMI in the microstructure. Depending on steelmaking and secondary metallurgy, NMIs may include oxides, sulfides, borides, phosphides/phosphates, silicates, and mixed agglomerates. Examples of oxidic NMIs and agglomerated defect populations are shown in Figures 9g and 10o,p (oxides), Figures 10i–l (oxide–MC agglomerates), and Figures 9h and 10m,n (oxide–MnS agglomerates). For fatigue-relevant assessment—particularly in hard, defect-containing steels and AM metals—it is well established that estimating the largest defects in a 3D volume from 2D metallographic sectioning is problematic.

As discussed by Beretta et al. [156–159], Murakami et al. [116, 118, 160–165], and Ekengren & Bergström [166, 167], 2D plane observations can substantially underestimate the true extreme-value distribution (e.g., for largest NMIs, pores, shrinkage cavities, or lack-of-fusion defects), because the probability of intersecting the true 3D extremes in random sections is limited. To quantify this effect for the present materials, Figure 15 compares extreme-value distributions for V10 PM-L[1], D2 HW-L, and D2 PM-L derived from datasets obtained by CGA (metallographic plane observations) versus SFSA (fracture-surface observations after RBT). In all cases, the two-parameter Gumbel distribution according to ASTM E2283-08R19 [146] was fitted using only the 24 largest $\sqrt{}$area values from the respective datasets to estimate the location parameter λ_{ML} and the scale parameter δ_{ML}. Extrapolated overall extreme sizes $x_{max,T}$ (µm) as a function of return period T (–) are summarized in Tables S5 and S6 (e.g., for $T =$ 10, 100, and 1,000).

Figure 15a–d compares CGA- and SFSA-based distributions for each steel. Figure 15e–f additionally contrasts SFSA distributions derived from (i) the 24 largest defects pooled across all investigated hardness levels and (ii) the 24 largest defects at a single hardness level (D2 HW-L: 59–60 HRC; D2 PM-L: 53–54 HRC). For V10 PM-L[1], CGA-based distributions derived separately from NMIs and MC carbide clusters are shifted to smaller $\sqrt{}$area values and thus substantially underestimate the extreme defect sizes observed by SFSA (Figure 15a,b). The same tendency is observed for D2 HW-L and D2 PM-L (Figure 15c,d), confirming that 2D plane-based estimates do not reliably capture the largest fatigue-relevant extremes.

For D2 HW-L, it should be noted that typical CGA focuses on NMIs, whereas SFSA identifies crack-initiating M_7C_3 carbides (or all other possible defects) as the relevant critical defects under the present loading and hardness conditions; these large carbides are not captured in standard CGA datasets (only measures NMIs; Figure 15c). In contrast, for V10 PM-L[1], the CGA datasets were separately measured for NMIs and also conspicuously coarsened MC carbide clusters (Figure 15a,b). Figure 15e,f demonstrate that SFSA-derived extreme-value distributions are affected as well by the sample numbers considered, i.e., the resulting distributions are shifted (slightly) toward larger $\sqrt{}$area sizes when considering the largest extremes from all batches at different hardness levels rather than only one batch at a single selected hardness level.

Overall, the comparisons in Figure 15a–d confirm that identifying true extremes is inherently a 3D volume problem: CGA yields local 2D plane extremes, while fatigue testing probabilistically activates the most critical defects within the highly loaded volume (HLV) of the specimen. The resulting fracture surface contains the governing crack initiator and thus provides a volume-sensitive sampling of largest extremes. Consistent with Beretta et al. [156–159] and Murakami et al. [116, 118, 160–165], for fatigue-relevant cleanliness assessment in this work, SFSA-derived critical extremes and their corresponding extreme-value statistics are focused, because these directly represent fatigue-relevant crack initiators (including NMIs, carbide clusters, and agglomerates, which depend on steelmaking route and microstructure).

3.4 | Database-Driven PSPP Correlations for Defect-Size- and Hardness-Dependencies

Based on the fatigue–strength and defect–property database, statistical PSPP correlations were derived to quantify defect-size- and hardness-dependencies, including an RHE-type behavior.

1869344x, 2026, 10, Downloaded from https://onlinelibrary.wiley.com/doi/10.1002/srin.202501039 by Universitatsbibliothek RWTH Aachen University, Wiley Online Library on [05/11/2026]. See the Terms and Conditions (https://onlinelibrary.wiley.com/terms-and-conditions) on Wiley Online Library for rules of use; OA articles are governed by the applicable Creative Commons License

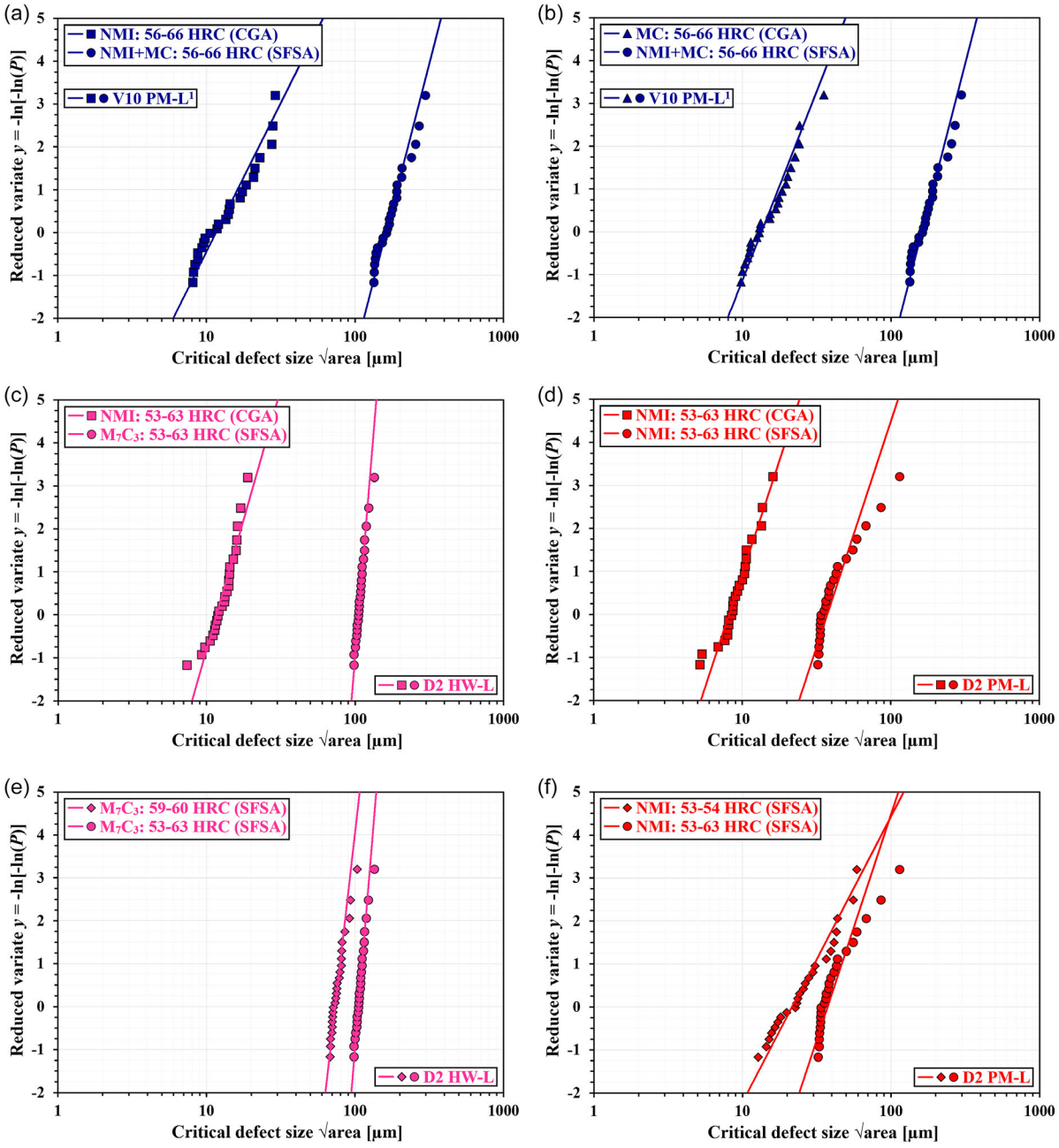

FIGURE 15 | Gumbel extreme-value distributions (ASTM E2283-08R19 [146]) fitted to the 24 largest $\sqrt{}$area values from CGA (metallographic planes) and SFSA (fracture surfaces). V10 PM-L[1] (56–66 HRC): (a) CGA—NMIs versus SFSA—NMI–MC agglomerates; (b) CGA—MC versus SFSA—NMI–MC agglomerates. D2 HW-L (53–63 HRC): (c) CGA—NMIs versus SFSA—M_7C_3; (e) SFSA single hardness (59–60 HRC) versus pooled across hardnesses (all eutectic M_7C_3 carbides). D2 PM-L (53–63 HRC): (d) CGA—NMIs versus SFSA—NMIs; (f) SFSA single hardness (53–54 HRC) versus pooled across hardnesses (all intrinsic NMIs).

Figure 16 presents the first PSPP correlation, which maps the 3D relationship between the local stress at the critical defect, σ_L (MPa), the critical defect size $\sqrt{}$area (µm), and the macrohardness (HRC) set by HT, following the power-law framework proposed by Sohar [71], Berns [141], and Murakami [116, 118] (cf. Figures 4, S2, and S14–S18).

Figure 16 distinguishes surface/contact defects from volume defects and includes power-law fits (solid red lines) with the corresponding fit equations and coefficients of determination R^2. For each hardness level, the left panels (Figure 16a–e) show the correlations for direct and up-staired fractures. The right panels show the corresponding correlations for run-outs; here, the "critical" defect size refers to the defect identified by SFSA after up-stairing and subsequent fracture. The resulting fit accuracies are acceptable given the experimental constraints, ranging from $R^2 \approx 0.51$–0.67 for fractures (Figure 16a–e, left panels) and $R^2 \approx 0.67$–0.79 for run-outs (Figure 16a–e, right panels).

It should be noted that the fracture lifetime $N_{Fracture}$ is not plotted in Figure 16 (for run-outs, $N_G = 10^7$ cycles applies). Moreover, unlike studies using artificially introduced surface defects with

1869344x, 2026, 10, Downloaded from https://onlinelibrary.wiley.com/doi/10.1002/srin.202501039 by Universitatsbibliothek RWTH Aachen University, Wiley Online Library on [05/11/2026]. See the Terms and Conditions (https://onlinelibrary.wiley.com/terms-and-conditions) on Wiley Online Library for rules of use; OA articles are governed by the applicable Creative Commons License

predefined size, shape, location, and applied stress level (e.g., Murakami & Endo [116, 118, 119] or Schönbauer et al. [168–171] reported results for artificial defects), the size and location of real manufacturing-related intrinsic defects are unknown prior to testing and are randomly distributed in the HLV. Consequently, specimens cannot be intentionally "placed" at selected

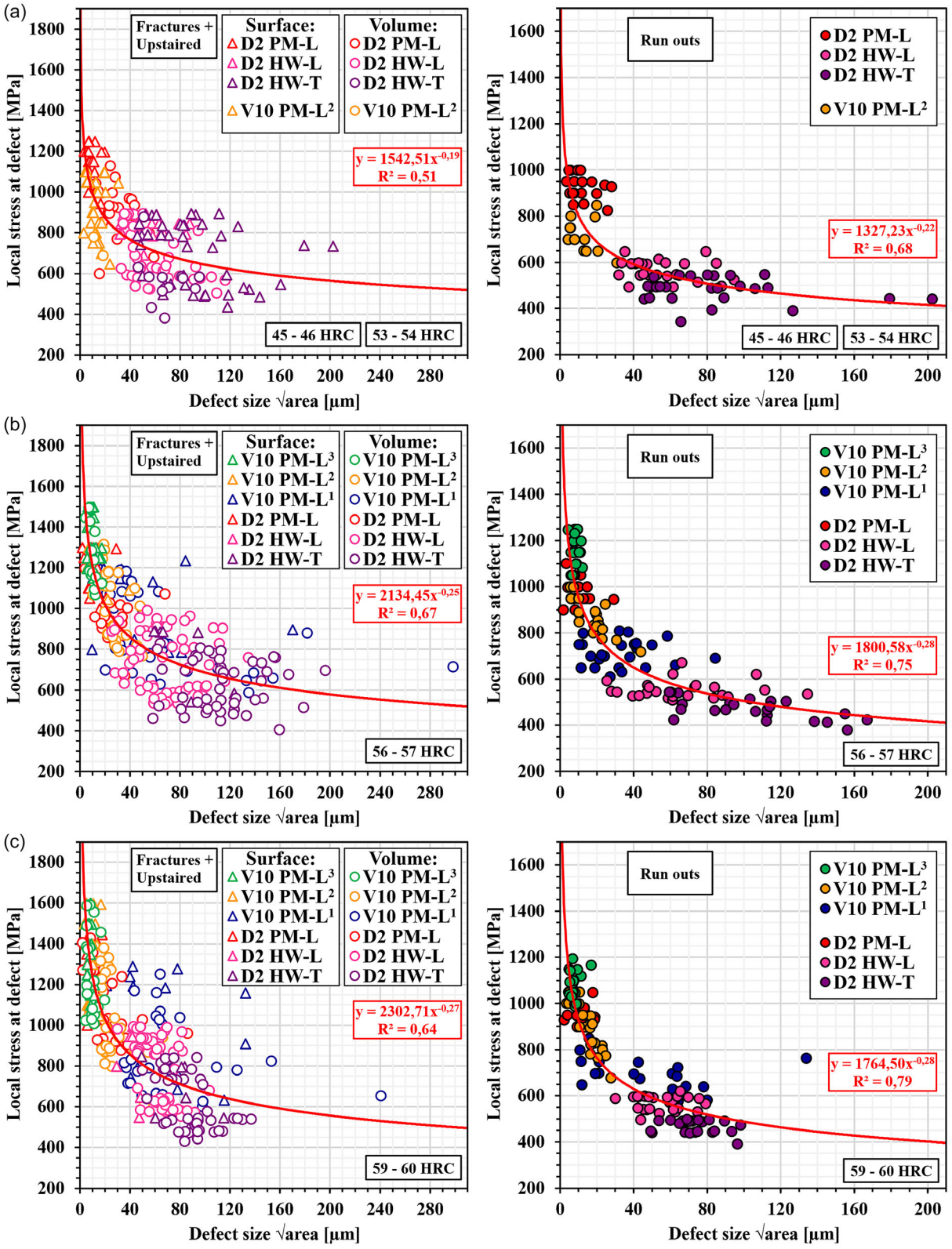

FIGURE 16 | PSPP correlation between local stress at the critical defect, σ_L (MPa), and defect size $\sqrt{}$area (µm) at fixed macrohardness levels for the studied D2 and V10 steels, using power-law fits following Sohar [71], Berns [141], and Murakami [116, 118] (cf. Figures 4, S2, and S14–S18). Left panels: fractures (direct and up-staired); right panels: run-outs. Data are shown for (a) 53–54 HRC (incl. V10 PM-L^2 at 45–46 HRC), (b) 56–57 HRC, (c) 59–60 HRC, (d) 62–63 HRC, and (e) 65–66 HRC (V10 only). Fit equations and R^2 values are included; surface/contact and volume defects are distinguished.

1869344x, 2026, 10, Downloaded from https://onlinelibrary.wiley.com/doi/10.1002/srin.202501039 by Universitatsbibliothek RWTH Aachen University, Wiley Online Library on [05/11/2026]. See the Terms and Conditions (https://onlinelibrary.wiley.com/terms-and-conditions) on Wiley Online Library for rules of use; OA articles are governed by the applicable Creative Commons License

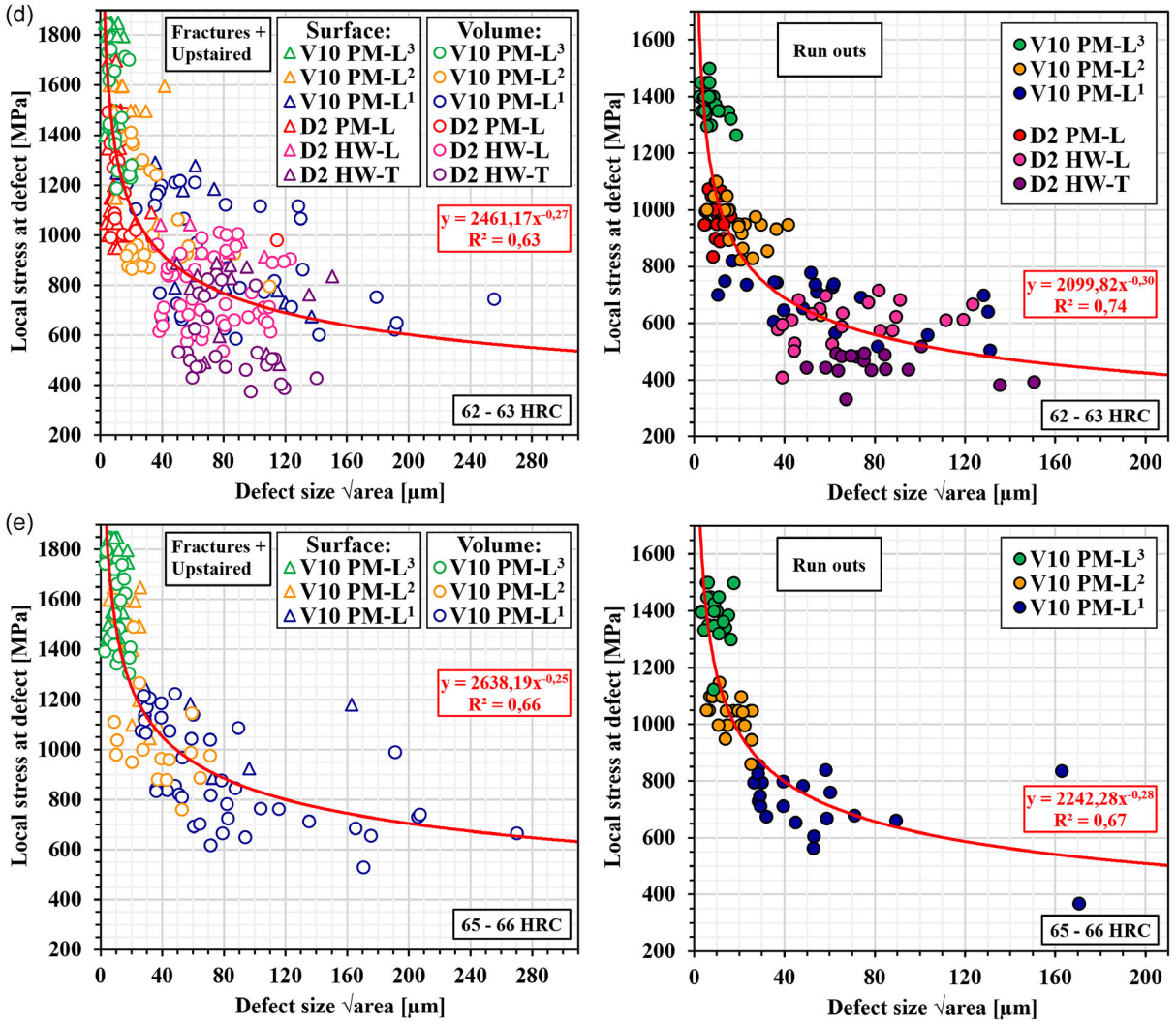

FIGURE 16 | Continued.

stress levels conditional on the contained largest defect to optimize the spread of data points for regression. Therefore, substantially higher R^2 values are not necessarily expected for the PSPP correlation in Figure 16. Nevertheless, Figure 16 demonstrates a clear and quantifiable relationship among $\sqrt{}$area, σ_L, and macrohardness for carbide-rich CWS that can be described appropriately by power-law functions.

A second PSPP correlation is shown in Figure 17 to quantify hardness dependence and potential RHE-type behavior. Figure 17a summarizes the D2 steels and Figure 17b the V10 steels. The statistical mean values $\sigma_{A,P=50\%}$ together with their abs. scatter bands ($P =$ 1%–99%) are plotted versus macrohardness; suitable fit functions are provided for continuous description together with R^2 values. For the D2 steels (Figure 17a), $\sigma_{A,P=50\%}$ increases approximately linearly with hardness for D2 PM-L ($R^2 \approx 0.91$) and D2 HW-L ($R^2 \approx 0.60$) with similar slope but different absolute strength levels; the higher level of D2 PM-L is consistent with its smaller, rounder critical defects (Figure 17a).

In contrast, D2 HW-T ($R^2 \approx 0.80$) shows a clear RHE-type behavior above ~56–57 HRC: $\sigma_{A,P=50\%}$ increases slightly up to 56–57 HRC and then decreases (moderately) with further hardness increase to ~63 HRC. Consistent with its larger critical defect sizes, D2 HW-T remains below D2 HW-L, and the hardness-dependent divergence is reflected in the *AI* of D2 IC, which increases from ~16% at 53–54 HRC to ~39% at 62–63 HRC due to the RHE occurring in D2 HW-T above 56–57 HRC (Figure 17a).

For the V10 steels (Figure 17b), $\sigma_{A,P=50\%}$ likewise shows approximately linear correlations with the macrohardness, but the fit slope depends strongly on PM-HIP grade: V10 PM-L^3 (slope $\approx +28.3$) is steeper than V10 PM-L^2 (slope $\approx +15.4$), whereas V10 PM-L^1 (slope $\approx +1.1$) exhibits the lowest slope and the largest scatter in $\sigma_{A,P=50\%}$ over hardness, resulting in poor fit quality ($R^2 \approx 0.02$). The other PM-HIP steels achieve high fit accuracies ($R^2 \approx 0.91$–0.99). Compared to the PM-HIP steels, D2 HW-L/-T show reduced fit quality (D2 HW-L: $R^2 \approx 0.60$; D2 HW-T: $R^2 \approx 0.80$). The slope of D2 PM-L (slope $\approx +8.8$) in Figure 17a is lower than that of V10 PM-$L^{3/2}$ in Figure 17b.

In Table 12, the critical defect-size data ($\sqrt{}$area$_{max}$) from Tables 11 and S10 and the hardness-fit slopes from Figure 17 are compared with classical reference data for artificial surface defects (equivalent $\sqrt{}$area values from drilled holes and linear

1869344x, 2026, 10, Downloaded from https://onlinelibrary.wiley.com/doi/10.1002/srin.202501039 by Universitatsbibliothek RWTH Aachen University, Wiley Online Library on [05/11/2026]. See the Terms and Conditions (https://onlinelibrary.wiley.com/terms-and-conditions) on Wiley Online Library for rules of use; OA articles are governed by the applicable Creative Commons License

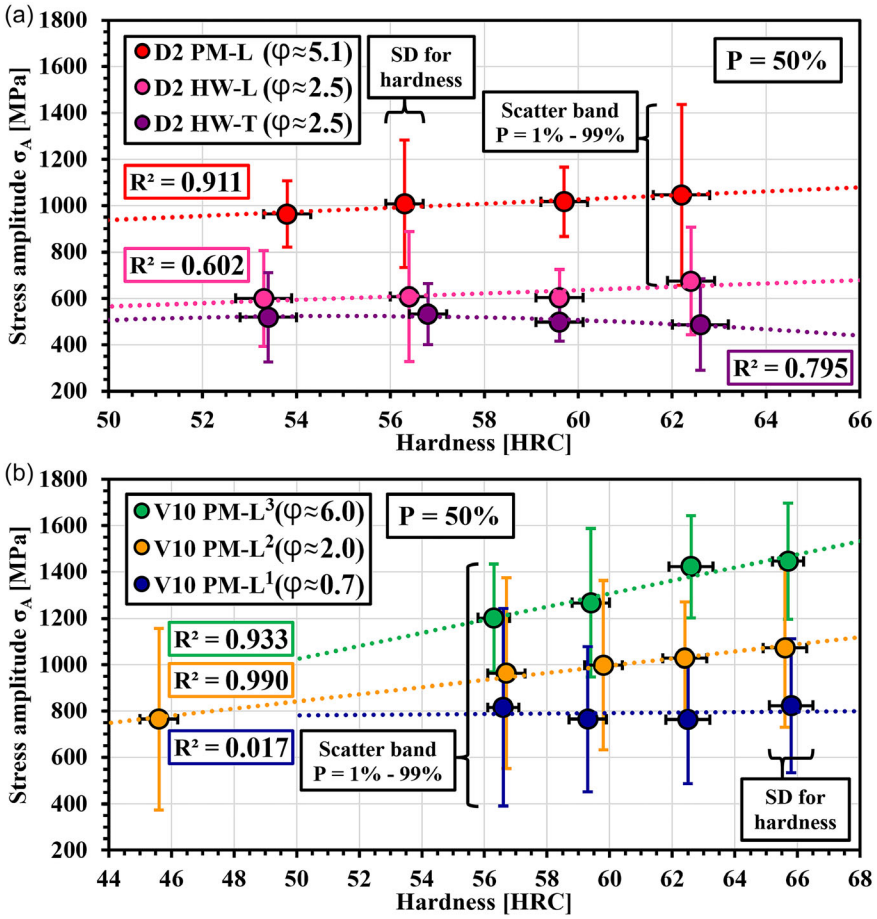

FIGURE 17 | PSPP correlation of $\sigma_{A,P}$ (MPa) versus macrohardness (HRC) with fit accuracies (R^2): (a) D2 PM-L and D2 HW-L/-T (53–63 HRC) and (b) V10 PM-$L^{1/2/3}$ (56–66 HRC), incl. V10 PM-L^2 at 45–46 HRC.

hardness-slope data) reported by Murakami & Endo [116, 118, 119] (cf. Figure 3b). For D2 HW-T, an additional linear fit was evaluated to enable direct comparison with the Murakami & Endo [116, 118, 119] slope data.

For D2 PM-L, D2 HW-L, and D2 HW-T, the slope trends and corresponding $\sqrt{area}_{max}$ values in Table 12 agree well with the Murakami & Endo [116, 118, 119] data for hardened and tempered carbon steels from Figure 3b. D2 PM-L and D2 HW-L show positive hardness effects (slopes ≈ +7.1 and ≈ +8.8), consistent with artificial holes of Ø ≈ 80–150 µm (slope ≈ +7.9). D2 HW-T shows a negative hardness effect (slope ≈ −4.2), consistent with artificial holes of Ø ≈ 260 µm (slope ≈ −4.3). Notably, an RHE-type reversal is observed only for D2 HW-T here; its $\sqrt{area}_{max}$ range and fitted slope align well with the Ø ≈ 260 µm case for which Murakami & Endo [116, 118, 119] reported a pronounced RHE-type reversal (Table 12; Figure 3b).

The positive hardness effects for V10 PM-$L^{3/2}$ (slopes ≈ +28.3 and ≈+15.4; smaller $\sqrt{area}_{max}$; no RHE-type behavior) are qualitatively consistent with the small-defect cases (Ø ≈ 0–40 µm) from Murakami & Endo [116, 118, 119] in Table 12,

TABLE 12 | Comparison of defect-size-dependent hardness effects (fit slopes) and RHE-type behavior for the six investigated D2 and V10 steel conditions with reference trends for artificial surface defects reported by Murakami & Endo [116, 118, 119], incl. corresponding $\sqrt{area}_{max}$ values of critical defects.

Steel	Hardness (HRC)	RHE occurrence		RHE according to Murakami & Endo [116, 118, 119]		
		$\sqrt{area}_{max}$ (µm)	Fit slope (–)	d/h (µm)	Equivalent $\sqrt{area}_{max}$ (µm)	Fit slope (–)
V10 PM-L^3	56–66	≈17.5–20.2	≈+28.3	≈0	≈0.0 (no defect)	≈+13.0
V10 PM-L^2	45–66	≈30.7–109.9	≈+15.4	≈40	≈37.0 (artificial hole)	≈+12.9
D2 PM-L	53–63	≈59.0–114.6	≈+8.8	≈80	≈74.0 (artificial hole)	≈+7.9
D2 HW-L		≈103.5–134.6	≈+7.1	≈120	≈111.0 (artificial hole)	≈+7.9
V10 PM-L^1	56–66	≈240.7–298.4	≈+1.1	≈150	≈138.8 (artificial hole)	≈+7.9
D2 HW-T	53–63	≈137.1–202.5	≈−4.2	≈260	≈240.5 (artificial hole)	≈−4.3

1869344x, 2026, 10, Downloaded from https://onlinelibrary.wiley.com/doi/10.1002/srin.202501039 by Universitatsbibliothek RWTH Aachen University, Wiley Online Library on [05/11/2026]. See the Terms and Conditions (https://onlinelibrary.wiley.com/terms-and-conditions) on Wiley Online Library for rules of use; OA articles are governed by the applicable Creative Commons License

although the fitted slopes for V10 PM-L$^{3/2}$ are noticeably larger than the ∼+12.9–13.0 reported for carbon steels at ∼50–58 HRC (Figure 3b). For V10 PM-L^{1}, $\sqrt{area}_{max}$ is the largest among the PM-HIP steels—exceeding even D2 HW-T—such that an RHE-type reversal would be expected based on the artificial-hole reference data (Ø ≈ 260 µm) in Table 12. However, no RHE-type behavior is observed in Figure 17b: the linear fit yields a slightly positive slope (≈+1.1) over ∼56–66 HRC.

Consequently, Table 12 highlights two open issues for the PM-HIP steels: (i) the comparatively steep positive slopes for V10 PM-L$^{3/2}$ (and also D2 PM-L) relative to the artificial-hole reference data (Ø ≈ 0–80 µm) at comparable $\sqrt{area}_{max}$ and (ii) the absence of an RHE-type reversal for V10 PM-L^{1} despite its $\sqrt{area}_{max}$ being larger than for D2 HW-T. These observations indicate that an additional FIF not yet accounted for in Figures 12–17 and Table 12 contributes significantly to the evaluated fatigue response of the studied carbide-rich CWS.

3.5 | Database-Driven Validation of Murakami's $\sqrt{area}$ Fatigue-Limit Model

The fatigue–strength and defect–property database (Figures 12–17; Tables 9, 10, S9 and S10) was used to apply Murakami's [116, 118] semi-empirical $\sqrt{area}$ model to the investigated IC and PM-HIP steels and to perform database-driven, statistical accuracy assessments. The normalized S–N curves in Figures 12 and 13 were also derived from these model applications. The objective of this validation is to quantify the resulting rel. prediction errors, ξ and ξ_{max}, across steelmaking routes and macrohardness levels, and to assess whether the exp. observed hardness trends—including the RHE-type behavior—are consistent with the defect-size-controlled mechanisms proposed by Garwood et al. [96] and Murakami & Endo [116, 118, 119].

A complete, batch-resolved error summary (ξ, ξ_{max}, and the total number of errors) is provided in Table S11; Table 13 reports condensed summaries for (i) the IC steel conditions, (ii) the PM-HIP steel conditions, and (iii) all steel conditions combined. Because Murakami's [116, 118] model predicts a fatigue limit σ_w (MPa), validation is inherently binary (correct/incorrect) for each specimen. A fracture (incl. up-staired fractures) is predicted correctly if the local stress amplitude at the critical defect, σ_L (MPa), exceeds the model prediction ($\sigma_L > \sigma_w$). Allowing the ±10% tolerance, a fracture is counted as correctly predicted when $\sigma_N \geq 0.9$. A run out (survivor) is predicted correctly if $\sigma_L < \sigma_w$; with ±10% tolerance, $\sigma_N \leq 1.1$. The errors ξ (%) and ξ_{max} (%) are calculated specimen-wise from the deviation between the model prediction and the exp. condition, and the total number (–) of errors is reported as a percentage of the evaluated specimens within each group.

Table 13 shows that for the IC steel conditions, errors ξ larger than ∼10% occur for both fractures and run-outs. The errors are $\xi_{max} \approx 21\% \pm 12\%$ for fractures and $\xi_{max} \approx 20\% \pm 13\%$ for run-outs. The error frequency is ∼26% for both fractures and run-outs, i.e., about one quarter of specimens are classified incorrectly in each group. This behavior is also reflected in the normalized S–N curves (notably for D2 HW-T at higher hardness in Figure 12g,h), where misclassified points lie outside the ±10% bounds (fractures below −10%, i.e., below $\sigma_N = 0.9$, or run-outs at $N_G = 10^7$ above +10%, i.e., above $\sigma_N = 1.1$).

For the PM-HIP steels, the model performs markedly better for fractures but poorly for run-outs. The errors are $\xi_{max} \approx 7\% \pm 7\%$ for fractures (smaller than for the IC steel) and $\xi_{max} \approx 49\% \pm 17\%$ for run-outs (substantially larger). Correspondingly, the error frequency is only ∼3% for fractures but ∼84% for run-outs—i.e., fractures are predicted correctly in most cases, whereas the majority of survivors are misclassified. When pooling all conditions and hardness levels, the final row of Table 13 yields $\xi_{max} \approx 14\% \pm 12\%$ for fractures and $\xi_{max} \approx 42\% \pm 20\%$ for run-outs. The overall error frequency is ∼12% for fractures and ∼64% for run-outs, i.e., the model classifies fractures relatively reliably but fails to predict a large fraction of run-outs, particularly for PM-HIP steels, in the present dataset.

3.6 | Surface Residual Stresses and Depth Profiles Measured by XRD

Exemplary surface RS measurements and RS depth profiles obtained by XRD along the specimen fabrication chain are summarized for the normal-stress components σ_{11} (axial) and σ_{22} (tangential) of the stress tensor (see Equation (8) in Section 2.3) in Figures 18 and 19, respectively. In Figure 18, bar numbers indicate the corresponding fatigue specimen; gray bars denote measurements at position B (opposite to A; cf. Figure 5). Elliptical fitting also yielded non-zero shear-stress components (τ_{12}, τ_{13}, and τ_{23}); however, these were generally smaller (τ_{12}, τ_{13}, $\tau_{23} \approx \pm 10$ to ± 200 MPa) than the normal

TABLE 13 | Database-driven validation of Murakami's [116, 118] $\sqrt{area}$ model using SFSA-derived defect data ($\sqrt{area}$, K, H_V and d_S) and exp. local stresses (σ_L) for the studied D2 and V10 steels. Reported are the rel. error ξ (%), the max. rel. error ξ_{max} (%), and the fraction (%) of misclassified fatigue specimens for fractures (incl. up-staired; IC: $n = 446$; PM-HIP: $n = 757$) and run-outs (IC: $n = 188$; PM-HIP: $n = 353$), summarized over all exp. S–N curves and investigated macrohardness levels.

Steels	Sample count n (–)	Occurring rel. errors ξ (%)		Max. rel. errors ξ_{max} (%)		Misclassification rate (%)	
		Fractures	Run-outs	Fractures	Run outs	Fractures	Run-outs
IC + HW	446	≈11.8 ± 9.6	≈9.8 ± 7.3	≈21.2 ± 11.6	≈20.1 ± 12.7	≈26.5	≈25.5
PM-HIP + HW	757	≈7.6 ± 5.1	≈26.4 ± 16.3	≈7.1 ± 6.5	≈48.8 ± 16.8	≈2.8	≈84.1
Overall	1203	≈11.2 ± 9.2	≈24.1 ± 16.4	≈14.2 ± 11.6	≈42.3 ± 19.9	≈11.6	≈63.8

1869344x, 2026, 10, Downloaded from https://onlinelibrary.wiley.com/doi/10.1002/srin.202501039 by Universitatsbibliothek RWTH Aachen University, Wiley Online Library on [05/11/2026]. See the Terms and Conditions (https://onlinelibrary.wiley.com/terms-and-conditions) on Wiley Online Library for rules of use; OA articles are governed by the applicable Creative Commons License

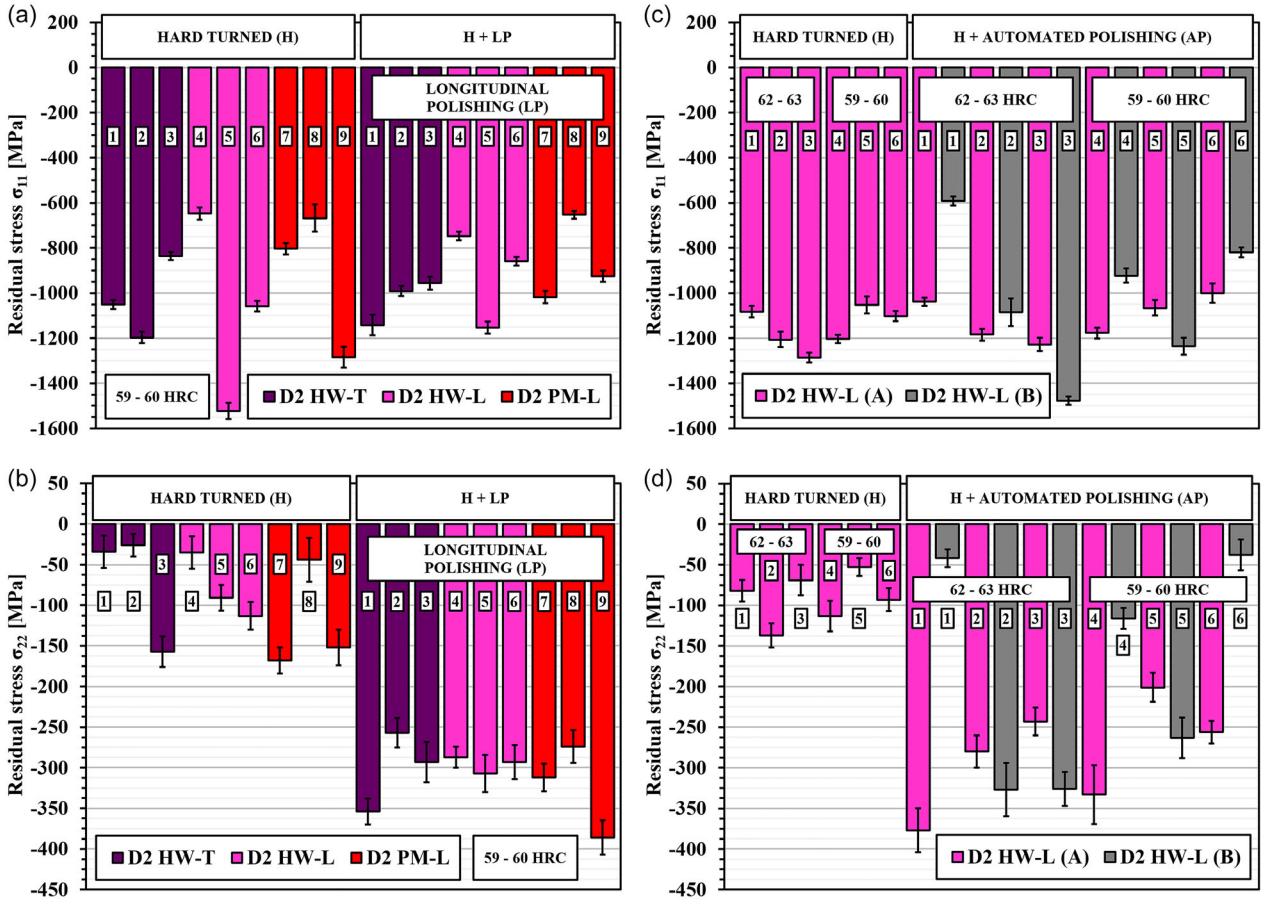

FIGURE 18 | Surface RS of selected fatigue specimens measured at positions A (and B where indicated; cf. Figure 5) using XRD. (a) + (c) σ_{11} (axial direction) and (b) + (d) σ_{22} (tangential direction). Shown are D2 PM-L, D2 HW-L, and D2 HW-T at 59–60 HRC (H vs. H + LP conditions) and D2 HW-L at 59–60 and 62–63 HRC (H vs. H + AP conditions; positions A vs. B).

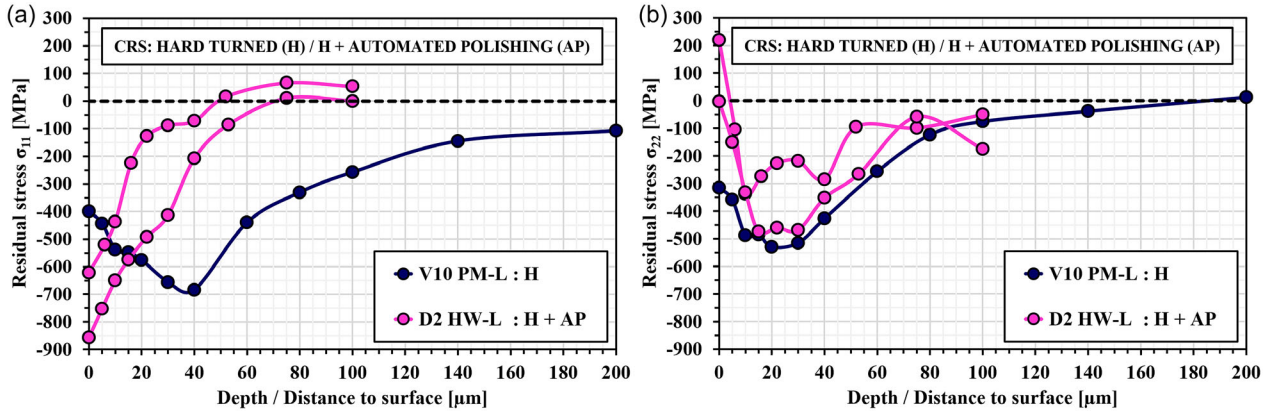

FIGURE 19 | Exemplary RS depth profiles obtained by stepwise electrolytic material removal from the specimen surface combined with XRD. (a) σ_{11} (axial direction) and (b) σ_{22} (tangential direction) for two D2 HW-L specimens (H + AP condition) and one V10 PM-L[1] specimen (H condition) at 59–60 HRC.

stresses ($\sigma_{11} \approx -1{,}500$ to $+100$ MPa; $\sigma_{22} \approx -550$ to $+250$ MPa) and are therefore excluded here. For superposition with bending or axial fatigue loading, σ_{11} (MPa) and σ_{22} (MPa) are the relevant RS components here. XRD phase analysis performed for selected fatigue specimens from D2 PM-L, D2 HW-L/-T, and V10 PM-L[1] showed negligible RA contents (near-zero or within the method uncertainty ~3%–5% for the utilized diffractometer/detector setup), confirming that the systematic HT schedules achieved the intended fully martensitic condition. Therefore, similar to the evaluated shear-stress components, the RA results are not shown here, as they do not add to the interpretation of the fatigue–strength and defect–property results; S–N curves, defect characteristics from SFSA, and fiRS values are substantially more relevant for the present assessment.

1869344x, 2026, 10, Downloaded from https://onlinelibrary.wiley.com/doi/10.1002/srin.202501039 by Universitatsbibliothek RWTH Aachen University, Wiley Online Library on [05/11/2026]. See the Terms and Conditions (https://onlinelibrary.wiley.com/terms-and-conditions) on Wiley Online Library for rules of use; OA articles are governed by the applicable Creative Commons License

Figure 18a,b compares σ_{11} and σ_{22} at 59–60 HRC for D2 PM-L, D2 HW-L, and D2 HW-T in the hard-turned condition (H) and after additional LP (H + LP). After hard turning, all three D2 steels exhibit pronounced surface CRS in the axial direction, with σ_{11} typically in the range of about −600 to −1,500 MPa and substantial specimen-to-specimen scatter. In the tangential direction, hard turning also produces CRS, but at markedly lower magnitudes ($\sigma_{22} \approx$ −25 to −150 MPa). Within the present dataset, the different carbide structures of D2 PM-L versus D2 HW-L/-T do not produce a clear difference in the resulting σ_{11} and σ_{22} levels after hard turning.

Comparing H with H + LP conditions shows that LP can modify the surface-near CRS state. For σ_{11}, the effect of LP is specimen-dependent, with σ_{11} values being (slightly) reduced or increased in individual cases. In contrast, LP consistently increases tangential CRS: σ_{22} shifts from about −25 to −150 MPa (H condition) to about −250 to −400 MPa (H + LP condition). This indicates that manual LP introduces substantial additional tangential CRS, largely independent of the specific D2 carbide structure (Figure 18a,b).

Figure 18c,d further shows σ_{11} and σ_{22} for D2 HW-L at 59–60 HRC and 62–63 HRC, including measurements at positions A versus B and the effect of AP (H + AP condition). AP also increases tangential CRS (typically $\sigma_{22} \approx$ −200 to −350 MPa), while σ_{11} remains similar to the hard-turned condition or decreases slightly. Compared with LP, the influence of AP on σ_{11} appears less pronounced. The A/B comparison indicates that machining- and polishing-induced RS are not necessarily uniform around the specimen circumference; σ_{11} and σ_{22} at position B can deviate substantially from the corresponding values at A.

Figure 19 compares σ_{11} and σ_{22} depth profiles for two D2 HW-L specimens (H + AP condition) with one V10 PM-L[1] specimen (H condition) at 59–60 HRC. For V10 PM-L[1] after hard turning, the CRS maxima occur below the surface: σ_{11} reaches about −700 MPa at $d_S \approx 40$ µm and σ_{22} about −550 MPa at $d_S \approx 20$ µm, whereas the surface values are smaller ($\sigma_{11} \approx$ −400 MPa; $\sigma_{22} \approx$ −300 MPa). The CRS decay to near-zero at about $d_S \approx 200$ µm for both components, indicating a comparatively deep machining-affected layer (Figure 19).

For D2 HW-L after H + AP, σ_{11} shows its maximum at the surface ($\sigma_{11} \approx$ −850 MPa and $\sigma_{11} \approx$ −625 MPa for the two specimens) and decreases to near-zero (or slightly into TRS) at $d_S \approx 70$ µm and $d_S \approx 50$ µm, respectively. For σ_{22}, the surface values are near-zero or slightly tensile, while subsurface CRS maxima are observed at shallow depths ($\sigma_{22} \approx$ −500 MPa at $d_S \approx$ 15–20 µm and $\sigma_{22} \approx$ −350 MPa at $d_S \approx 10$ µm). The σ_{22} profiles then decrease toward near-zero at about $d_S \approx$ 60–80 µm. Overall, fiRS form multiaxial, quasi-static stress states that depend on direction (σ_{11} vs. σ_{22}), vary between specimens and processing/machining conditions, and can also vary around the specimen circumference (A vs. B) and with depth (Figure 19). The implications of fiRS characteristics for the fatigue results and the observed hardness/RHE trends are addressed in the subsequent discussion (Section 4.4).

4 | Discussion

The present findings are interpreted in the context of prior literature. For PSPP chains of carbide-rich CWS, the defect-size- and hardness-dependent database established here captures, with quantitatively robust statistics, how steelmaking routes—including HW and HT—govern differences in statistical LLF strength via the extreme-value distribution of intrinsic defects. The database further underscores that sufficiently large experimental statistics (sample and batch sizes, fracture-surface observations, etc.) and systematic specimen-fabrication schemes (HT schedules, machining/polishing, hardness testing, etc.) are indispensable for deriving justified statistical PSPP correlations and for enabling reliable fatigue-oriented design approaches for defective, carbide-rich (ultra-)high-strength steels.

4.1 | Manufacturing-Dependent Defect Size as Dominant Fatigue-Influencing Factor

Across all investigated carbide-rich CWS, the ranking of statistically evaluated LLF strengths is explained most consistently by the manufacturing-controlled extreme-value distribution of intrinsic defects, expressed here by $\sqrt{\text{area}}$ (i.e., $\sqrt{\text{area}}_{\text{min}}$, $\sqrt{\text{area}}_{\text{mean}}$, and $\sqrt{\text{area}}_{\text{max}}$ of extreme defects; Figure 14a; Table S10). The two D2 IC conditions (D2 HW-L/-T) exhibit substantially lower LLF strengths over 53–63 HRC than the PM-HIP steels because their crack initiators are much larger eutectic M_7C_3 carbides, which—especially in the transverse direction—occur more frequently in the HLV and exhibit irregular, blocky morphologies. Conversely, the cleaner PM-HIP steels (V10 PM-L[3], V10 PM-L[2], and D2 PM-L) achieve clearly higher LLF strengths over 45/53/56–63/66 HRC because their crack-initiating defects are significantly smaller and show lower size scatter than in the less clean V10 PM-L[1] condition.

From a mechanistic viewpoint, this defect-size dominance is consistent with Murakami's [116, 118] mechanics-of-small-cracks framework and prior findings for hard, defect-containing steels [11, 66, 71–80, 86–93, 97–112, 116, 118, 119, 126–128, 139, 140, 147, 160–165]. Murakami [116, 118] emphasizes that defect morphology primarily affects finite-life behavior (N_{Fracture}) through changes in the effective mode-I SIF range ΔK_I at the defect–matrix interface (e.g., sharp edges of primary/eutectic carbides) at a given local stress amplitude. By contrast, near the fatigue limit of hard steels the controlling condition is the existence of nonpropagating cracks (or nondamaging defects; cf. Figures 4 and S14–S18) governed by a small-crack mode-I threshold $\Delta K_{\text{th,SC}}$. Consequently, under LLF conditions the largest defect/crack size present is the primary microstructural descriptor, whereas the original defect shape becomes less important because the emanating small-crack tip is effectively maximally sharp [116, 118]. This interpretation is consistent with the present observation that LLF strength differences track $\sqrt{\text{area}}$ extreme-value statistics more robustly than 2D/3D shape descriptors such as circularity, roundness, and/or sphericity.

To illustrate defect-size dominance as the primary FIF for carbide-rich CWS, Figure 20 shows two-parameter Gumbel distributions according to ASTM E2283-08R19 [146] fitted using the

1869344x, 2026, 10, Downloaded from https://onlinelibrary.wiley.com/doi/10.1002/srin.202501039 by Universitatsbibliothek RWTH Aachen University, Wiley Online Library on [05/11/2026]. See the Terms and Conditions (https://onlinelibrary.wiley.com/terms-and-conditions) on Wiley Online Library for rules of use; OA articles are governed by the applicable Creative Commons License

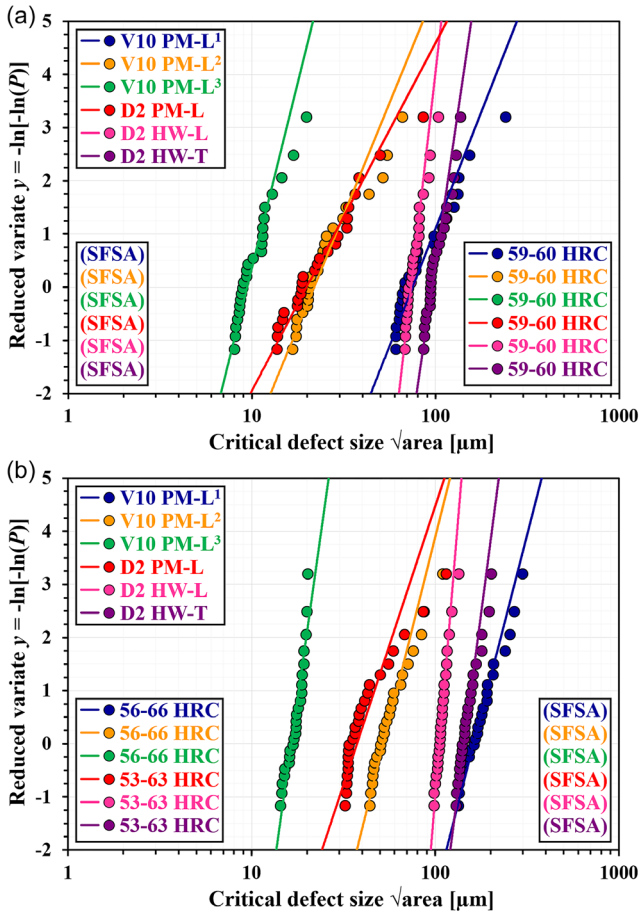

FIGURE 20 | Comparison of extreme-value distributions of six carbide-rich CWS configurations derived according to ASTM E2283-08R19 [146] from SFSA datasets (fatigue fracture-surface observations) at (a) 59–60 HRC and (b) the investigated hardness ranges (53–63 HRC for D2 steels; 56–66 HRC for V10 steels).

24 largest $\sqrt{\text{area}}$ values from the respective SFSA datasets (fracture-surface observations). Figure 20a compares distributions at 59–60 HRC (single hardness level), whereas Figure 20b pools data across the investigated hardness ranges (53–63 HRC for D2; 56–66 HRC for V10). Comparative extreme-value plots for each single hardness are provided in Figure S19a–d.

Figure 20a,b (and Figure S19a–d) show that LLF performance (Figures 12–17; Tables 9 and 10) is consistently tracked by the $\sqrt{\text{area}}$ extreme-value statistics, both (i) within a single hardness level and (ii) when pooling across the full hardness ranges. At 59–60 HRC (Figure 20a), the ordering follows LLF-strength ranking: V10 PM-L^3 (smallest extremes), D2 PM-L and V10 PM-L^2 (similar extremes), V10 PM-L^1 (broadest scatter), followed by D2 HW-L, and finally D2 HW-T. Notably, the V10 PM-L^1 fit line crosses those of D2 HW-L/-T, indicating that V10 PM-L^1 can contain both smaller and larger extremes than the D2 IC steel, whose crack initiators are exclusively M_7C_3 carbides. This reflects the pronounced microstructural scatter in V10 PM-L^1 related to its manufacturing route and also contributes to its moderately higher $\sigma_{A,P=50\%}$ compared with D2 HW-L/-T (cf. Tables 9 and 10).

When pooling across hardness (Figure 20b), the ordering remains broadly consistent with LLF trends and separates D2 PM-L and V10 PM-L^2 more clearly: V10 PM-L^3 (smallest extremes), D2 PM-L (many of the largest extremes remain smaller than in V10 PM-L^2), then V10 PM-L^2, followed by D2 HW-L and D2 HW-T. In contrast, V10 PM-L^1 becomes the right-most (largest) distribution when considering the overall 24 largest extremes across all batches because V10 PM-L^1 contains the largest $\sqrt{\text{area}}_{\max}$ values in the defect–property database (i.e., the most detrimental oxidic NMI/agglomerates). Thus, V10 PM-L^1 remains the only persistent discrepancy: while being PM-HIP, it contains the largest $\sqrt{\text{area}}_{\max}$ values—exceeding even D2 HW-T—due to intentionally reduced cleanliness during atomization, uncontrolled powder handling, additional melt sulfurization (FeS), and a strongly reduced HW degree ($\varphi \approx 0.7$).

These manufacturing conditions promote: (i) very large oxidic NMIs and increased inclusion frequency (Figures 10i–l, 11, and S4), (ii) MC carbide coarsening/clustering (Figure S5; linked to high counts of smaller and larger oxidic NMIs; cf. Figures S4, S5, and S13d), and (iii) large multiphase agglomerates combining oxides with MnS and/or P-containing constituents (phosphides and/or phosphates), as well as (strongly) coarsened MC clusters. The susceptibility to MC coarsening—also present in V10 PM-L$^{2/3}$ (cf. Figures 11d, S10d, S11a, and S11c) but at much lower extent—is consistent with the V-rich, high-carbon alloy concept of V10 and its high carbide fraction. By contrast, D2 (low V content; lower carbide fraction; Cr-based M_7C_3 and no primary MC formation) does not exhibit analogous MC carbide coarsening.

Although D2 PM-L and V10 PM-L^2 can also exhibit agglomerated defect types (D2 PM-L mainly oxide–MnS; V10 PM-L^2 chemically similar agglomerates to V10 PM-L^1; cf. Table 11, Figures S10, S13a, and S13d,e), the size, frequency, and spatial distribution of the largest agglomerates differ markedly, which is decisive for $\sqrt{\text{area}}_{\max}$ and the resulting LLF strengths.

Consistent with its highest LLF strengths (Figures 12–17) and its smallest extremes (Figure 20), the chemically equivalent grade V10 PM-L^3 shows no agglomerates or coarsened clusters as critical defects (cf. Figures 10i–p, 11, S11, S13a, and S13d–f), despite occasional very slight MC coarsening. As emphasized by Picas [2, 120], Jung [11], Marsoner et al. [13, 140, 147], Jesner [14], Beretta et al. [156–159, 172], and Murakami et al. [116, 118, 119, 160–165], this implies that fatigue–strength improvements should target the dominant microstructural FIF, i.e., defect-size extremes, through microstructural refinement of carbide structure and NMI populations.

In this context, statistical fatigue testing combined with fracture–surface analysis and systematic variation of specimen fabrication enables statistically reliable classification and interpretation via extreme-value analysis, consistent with Beretta et al. [156–159, 172] and Murakami et al. [116, 118, 119, 160–165]. The broader significance of these methodologies, and of extreme-value analysis as a powerful tool for understanding manufacturing influences (including AM) on fatigue, has also been confirmed more recently by Tomaszewski & Papuga [173], Sepati et al. [174], and Buiter et al. [175]. Overall, the PM-HIP subsets in Figure 20 are fully consistent with LLF performance. By contrast, the comparisons between V10 PM-L^1 and D2 HW-L/-T in Figure 20 suggest that at least one additional relevant FIF—beyond $\sqrt{\text{area}}$ and hardness—contributes to the

1869344x, 2026, 10, Downloaded from https://onlinelibrary.wiley.com/doi/10.1002/srin.202501039 by Universitatsbibliothek RWTH Aachen University, Wiley Online Library on [05/11/2026]. See the Terms and Conditions (https://onlinelibrary.wiley.com/terms-and-conditions) on Wiley Online Library for rules of use; OA articles are governed by the applicable Creative Commons License

observed LLF behavior. This is addressed in the following subsections (Sections 4.3–4.4).

4.2 | Steelmaking and Process Cleanliness as a Root cause of Intrinsic Defect Populations

Since the industrial introduction of PM-HIP tool steels in the 1970s, NMI-related cleanliness has been recognized as a key limitation—particularly for high-alloy grades with very high carbide contents—and manufacturers have continuously optimized atomization and downstream processing to improve steel cleanliness. Typical oxidic macroinclusions (e.g., Al-, Si-, Mg-, and Ca-based) originate mainly from slags (and/or scrap-derived oxides) and can be entrained by melt turbulences during teeming and stream feeding into the atomizer, thereby becoming incorporated into the powder. Additional sources of high-melting macroinclusions in atomization systems are washouts from refractory linings (often Al- and/or Mg-based) and from atomization nozzles (e.g., Zr-based components).

Overall, the present results support the established view that the manufacturing route determines which microstructural constituents become fatigue-critical in hard and carbide-rich steels [11, 66, 71–80, 86–93, 97–112, 116, 118, 119, 126–128, 139, 140, 147, 160–165]. If the largest carbides exceed all other intrinsic defects in size, they tend to dominate LLF performance; if carbide growth is suppressed—e.g., by higher cooling rates in remelting routes or, most effectively, during powder atomization—carbides become smaller than the NMI extremes, and the fatigue-critical population commonly shifts toward the largest macroinclusions and/or agglomerates [11, 66, 71–80, 86–93, 97–112, 116, 118, 119, 126–128, 139, 140, 147, 160–165]. This transition is particularly relevant for PM-HIP steels: atomization cooling rates reduce primary/eutectic carbide sizes to the micrometer scale, such that—depending on cleanliness—NMIs and agglomerates become lifetime-limiting under fatigue. Similar qualitative process–microstructure–fatigue relationships in carbide-rich IC and PM-HIP tool steels have been documented repeatedly by Jung [11], Beiss [66], Sohar et al. [71–80], Berns et al. [86, 87, 141], Broeckmann et al. [88], Bergström et al. [89], Yao et al. [109–112], Murakami et al. [116, 118, 119, 160–165], Schönbauer et al. [168–171], and Shiozawa et al. [176–180]. Additional supporting studies across grades, routes, and testing conditions are compiled in refs. [2, 13, 14, 30, 31, 56, 90–93, 97–108, 117, 120–128, 139, 140, 147, 156–158, 181–183].

Beyond defect size, defect types are likewise manufacturing-controlled and depend on plant technology, process cleanliness, and alloy concept. From a chemical-origin perspective, most large oxidic and heterogeneous NMIs identified here are best interpreted as exogeneous impurities introduced during steelmaking/secondary metallurgy (slag/scrap-related oxide entrainment; also refractory washouts). Endogenous constituents such as MnS (and, depending on alloy concept, coarsened MC carbides) can precipitate during solidification/cooling—particularly for V10 PM-L[1] with intentional sulfurization for improved machinability—thereby enabling larger oxide–MnS, oxide–MC, and oxide–MC–MnS agglomerates through clustering phenomena (cf. Figures 9h, 10i–n, 11, and S10–S13; agglomeration in V10 PM-L[1], V10 PM-L[2], and D2 PM-L; MC coarsening in V10 PM-L[1/2/3], most pronounced in V10 PM-L[1]).

For fatigue–strength assessment, the exact chemical origin/classification is secondary: Murakami's [116, 118] $\sqrt{\text{area}}$ model contains no explicit terms for defect chemistry or morphology, reflecting its small-crack, fracture-mechanics basis and practical applicability. Accordingly, within the present dataset, the dominant driver of LLF-strength differences is the manufacturing-dependent defect state (size extremes, scatter, and agglomeration propensity), not the average matrix composition or total carbide fraction. This is evident for the V10 PM-HIP grades: they are macroscopically compositionally similar and underwent identical HT schedules, yet show large differences in LLF strength; similarly, D2 IC and D2 PM-HIP differ primarily by manufacturing route (cf. Figures 12–17, S12, and S13; Tables 9–11, S9, and S10).

At the same time, for targeted process improvements—especially for powders, PM-HIP, and PM-AM steels with/without HIP—chemical classification and likely origins of critical defects are highly valuable. In PM-HIP steels, carbide growth is largely suppressed by atomization cooling rates, so that (depending on the cleanliness level) NMI size and agglomeration propensity dominate fatigue. Against this background, the present results motivate a pragmatic cleanliness-based classification for PM-HIP steels:

- **Low cleanliness** (large extremes; frequent agglomeration/clustering and pronounced MC coarsening): **V10 PM-L[1].** Reduced atomization cleanliness, uncontrolled powder handling, and very low HW degree ($\varphi \approx 0.7$) promote large and frequent oxidic macroinclusions and pronounced coarsening of primary MC carbides. Additional sulfurization increases endogenous MnS precipitation, facilitating large heterogeneous oxide–MnS and oxide–MC–MnS agglomerates. Refractory washout provides an additional source of high-melting oxides; sporadic ZrO_2 inclusions are plausibly linked to zirconia-based nozzle/lining components. P-containing constituents detected in some oxide-rich agglomerates may originate from refractory repair materials using phosphoric-acid-based binders; because EDS cannot unambiguously distinguish phosphides from phosphates here, the term "P-containing constituents" is retained. Overall, the combination of high inclusion counts/surfaces and elevated sulfur promotes large multiphase agglomerates and heavily coarsened MC clusters, consistent with comparatively low LLF strengths and the very weak hardness dependence of V10 PM-L[1]. Low melt cleanliness may promote local carbide coarsening by heterogeneous nucleation on inclusion surfaces (oxidic NMIs contained in the liquid phase may act like foreign surfaces). This coupling between high inclusion populations and enhanced local coarsening of primary carbide phases is treated here as a plausible interpretation rather than a proven causal chain. Mechanistic details are most probably very complex, also depend on local thermodynamics/kinetics, and are not resolved in the present study.

- **Medium cleanliness** (moderate extremes; reduced agglomeration/clustering and MC coarsening): **D2 PM-L** and **V10 PM-L[2].** With roughly standard industrial

1869344x, 2026, 10, Downloaded from https://onlinelibrary.wiley.com/doi/10.1002/srin.202501039 by Universitatsbibliothek RWTH Aachen University, Wiley Online Library on [05/11/2026]. See the Terms and Conditions (https://onlinelibrary.wiley.com/terms-and-conditions) on Wiley Online Library for rules of use; OA articles are governed by the applicable Creative Commons License

cleanliness and different HW degrees (V10 PM-L^2: $\varphi \approx 2.0$; D2 PM-L: $\varphi \approx 5.1$), these grades lack the extremely large NMIs/agglomerates characteristic of V10 PM-L^1 and therefore achieve markedly higher statistical LLF strengths and a steeper positive hardness effect on $\sigma_{A,P=50\%}$ (fit slope).

- **High cleanliness** (small extremes; agglomeration/clustering largely absent; only very slight MC coarsening): **V10 PM-L^3.** High process cleanliness combined with high HW degree ($\varphi \approx 6.0$) yields the smallest defect extremes. For high-carbide alloys, cleaner atomization/powder handling and reduced sulfurization are essential to avoid pronounced agglomeration and strong primary-carbide coarsening; consequently, V10 PM-L^3 exhibits the highest LLF strengths and the strongest positive hardness effect on $\sigma_{A,P=50\%}$ (fit slope) in the present dataset.

Importantly, SFSA combined with EDS not only provides statistically meaningful geometric defect descriptors; it also functions as a practical defect/NMI tracing tool by linking critical defect chemistry qualitatively to likely process origins. Very recent and analytically advanced inclusion-tracing studies (including rare-earth (RE) tracing using Ce/La) by Mayerhofer [125], Sammer et al. [184], Musi et al. [185], Truschner et al. [186], Schickbichler et al. [187], and Thiele et al. [188–191] likewise report heterogeneous and multiphase NMIs (oxide/sulfide/oxide–sulfide/nitride–sulfide) consistent with the complex crack-initiator chemistries observed here by SEM–EDS. Reported examples include SiO_2–Al_2O_3, AlN/TiN, (Ca/Zr, Mg, Mn)S, (Al, Ca, Mg, Mn)OS, (Al, Mg)NS, MA spinels containing Al–Mg–O, and mixed systems such as MnS–TiN, MnS–Al_2O_3, MnS–(Al, Ca, Si)O, Al_2O_3–TiO_x, and multiphase (Ca, Si, Al, Mg) oxides [125, 184–191]. This supports the present SEM–EDS findings of heterogeneous oxidic, sulfidic, and P-containing crack initiators in carbide-rich CWS. Such chemical attribution can further support targeted improvements in PM-HIP steelmaking and powder handling (cf. RE-based NMI tracing/isotope-vaccination concepts) [125, 184–191].

Overall, this process-rooted interpretation—defect-size dominated, with chemistry as a diagnostic for origins—provides the basis for the subsequent discussion of the derived PSPP correlations, defect-size-controlled hardness trends (fit slopes; including RHE-type behavior), and the role of surface integrity effects on the statistical LLF strength $\sigma_{A,P=50\%}$. Having established defect-size extremes as the dominant manufacturing-controlled driver of LLF strength, the following discusses how these defect populations modulate hardness sensitivity and govern the emergence of RHE-type behavior.

4.3 | Defect-Size-Dependent Hardness Trends and RHE-Type Behavior

This subsection first discusses consistent and inconsistent cases relative to the drilled-hole reference data of Murakami & Endo [116, 118, 119] summarized in Table 12 and then outlines the mechanistic basis for positive hardness trends and the RHE threshold. This mechanistic basis is subsequently used to connect the inconsistent cases to the likely role of an additional FIF that superimposes defect-size and hardness effects.

The hardness sensitivity of the LLF strength and the emergence of RHE-type behavior are discussed using the comparative summary in Table 12, which links (i) the linear hardness-fit slopes derived from the present datasets (Figure 17; real manufacturing-related intrinsic defects over ~45/53/56–63/66 HRC) to (ii) the reference slopes reported by Murakami & Endo [116, 118, 119] for drilled surface holes in hardened and tempered carbon steel (Figure 3b; ~50–58 HRC), together with the associated extreme-size metrics (present $\sqrt{\text{area}}_{max}$ vs. equivalent $\sqrt{\text{area}}$ of drilled holes). Overall, the hardness trends measured for the present IC and PM-HIP steels are broadly consistent with the defect-size-controlled framework proposed by Garwood et al. [96] and Murakami & Endo [116, 118, 119] (cf. Figures 3, 17, and 20; Table 12).

In the present dataset, RHE-type reversal is observed unambiguously only for D2 HW-T (Figure 17a): its extreme defect sizes $\sqrt{\text{area}}_{max}$ and its negative hardness-fit slope agree closely with the large-hole reference case of Murakami & Endo [116, 118, 119] (slopes ≈ –4.2 vs. –4.3; Table 12). This observation is also in line with the broader evidence that decreasing fatigue strength at high hardness can occur in carbide-rich tool steels when sufficiently large extremes govern crack initiation (e.g., Marsoner et al. [140]; cf. Figure S1a–d and Table S4).

Conversely, the positive hardness-fit slopes obtained for D2 PM-L and D2 HW-L are consistent with the intermediate defect-size reference regime: their slopes (≈ + 7.1 and ≈ + 8.8) match well with Murakami & Endo's [116, 118, 119] drilled-hole cases in the range $d \approx 80$–150 µm (slope ≈ + 7.9; Table 12). These agreements support the interpretation that, for carbide-rich CWS, the sign and magnitude of the hardness trend can be rationalized primarily by the extreme-value defect size controlling LLF behavior. For the cleaner PM-HIP grades V10 PM-L^3 and V10 PM-L^2, the evaluated $\sqrt{\text{area}}_{max}$ values are broadly consistent with the small-to-intermediate drilled-hole regimes (Table 12), roughly corresponding to $d \approx 0$–40 µm for V10 PM-L^3 and $d \approx 40$–120 µm for V10 PM-L^2. However, their exp. hardness-fit slopes are markedly steeper than the Murakami & Endo [116, 118, 119] reference slopes at comparable defect sizes (≈ + 28.3 vs. ≈ + 13.0 for V10 PM-L^3; ≈ + 15.4 vs. + 7.9–12.9 for V10 PM-L^2; Table 12).

A second, even more striking inconsistency occurs for V10 PM-L^1. Based on its extreme defect sizes, an RHE-type reversal would be expected: $\sqrt{\text{area}}_{max}$ is in the range ≈ 240.7–298.4 µm, comparable to (and even exceeding) the drilled-hole case $d \approx 260$ µm (equivalent $\sqrt{\text{area}} \approx 240.5$ µm; slope ≈ –4.3; Table 12). Accordingly, V10 PM-L^1 would be expected to show a negative hardness-fit slope and a pronounced reversal—potentially even more pronounced than D2 HW-T. Instead, V10 PM-L^1 shows no RHE-type reversal and exhibits a slightly positive fit slope (≈ + 1.1; Table 12). At the same time, the general tendency that steels with smaller $\sqrt{\text{area}}_{max}$ (e.g., V10 PM-L$^{3/2}$ and D2 PM-L) show steeper positive hardness trends than steels with larger extremes (e.g., D2 HW-L and V10 PM-L^1) is qualitatively consistent with the defect-size-controlled hardness sensitivity. The unresolved point is that, quantitatively, the PM-HIP slopes are either too steep (V10 PM-L$^{3/2}$, D2 PM-L) or exhibit

1869344x, 2026, 10, Downloaded from https://onlinelibrary.wiley.com/doi/10.1002/srin.202501039 by Universitatsbibliothek RWTH Aachen University, Wiley Online Library on [05/11/2026]. See the Terms and Conditions (https://onlinelibrary.wiley.com/terms-and-conditions) on Wiley Online Library for rules of use; OA articles are governed by the applicable Creative Commons License

the wrong sign (V10 PM-L[1]) relative to the drilled-hole reference at comparable $\sqrt{\text{area}}_{max}$.

The positive hardness dependence of $\sigma_{A,P=50\%}$ can be rationalized within a fracture-mechanics framework for short cracks (SC; Figure 21) and the Kitagawa–Takahashi [193] diagram/concept: increasing matrix hardness increases $\Delta K_{th,SC}$ (only for SCs but not for LCs) and the resistance to microplasticity, thus can shift crack initiation and early small-crack propagation in hard steels to higher stress amplitudes. Chapetti et al. [192] proposed a relationship between the threshold SIF ranges for SCs and LCs, $\Delta K_{th,SC}$ and $\Delta K_{th,LC}$, as a function of effective crack size (expressed via $\sqrt{\text{area}}$) and matrix hardness; this concept is reproduced in Figure 21. In this framework, $\Delta K_{th,SC}$ depends on crack size and increases with matrix hardness, whereas $\Delta K_{th,LC}$ approaches a size-independent threshold in the long-crack regime and tends to decrease with increasing hardness (Figure 21), consistent with increased notch sensitivity and reduced long-crack growth resistance at higher hardness in many hard steels [118, 192, 193].

Within the Berns [141]-type schematic picture (Figure 4), an RHE-type reversal is expected once the characteristic defect size (d_1) exceeds the tolerable/critical threshold for a given hardness (reversal point at $d_1 = d_t = d_c$). In the present dataset, D2 HW-T clearly exceeds this threshold in the investigated hardness range, and the reversal is experimentally observed. By contrast, the absence of an RHE-type reversal for V10 PM-L[3/2] and D2 PM-L is consistent with their smaller extreme defects. Taken together, the comparisons to the drilled-hole reference indicate that defect size ($\sqrt{\text{area}}_{max}$) and hardness alone cannot fully explain the PM-HIP hardness slopes, particularly (i) the unusually steep positive slopes of V10 PM-L[3/2] (and D2 PM-L) and (ii) the missing RHE-type reversal for V10 PM-L[1] despite its very large $\sqrt{\text{area}}_{max}$. Therefore, at least one additional FIF must superimpose the defect-size–hardness relationship in the present experimental results.

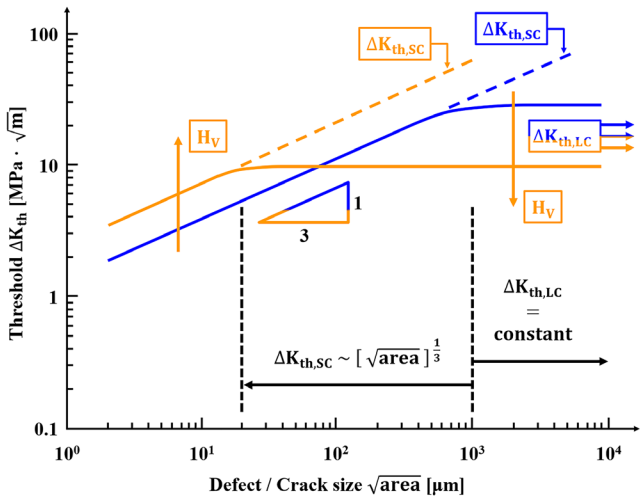

FIGURE 21 | Influence of effective defect/crack size (expressed as $\sqrt{\text{area}}$) and matrix hardness on the threshold SIF ranges $\Delta K_{th,SC}$ and $\Delta K_{th,LC}$ (MPa · $\sqrt{\text{m}}$) for small and long cracks, as proposed by Chapetti et al. [192]. Reprinted and adapted (modified replot) with permission [192]. Copyright 2003, Elsevier B.V.

As shown in Section 3.6, substantial surface-near CRS are introduced by hard turning and surface polishing. It is therefore plausible that fiCRS significantly affect the observed hardness trends and the apparent presence/absence of RHE-type behavior in experimental fatigue testing—an effect that is examined in the next subsection (Section 4.4).

4.4 | Role of Finishing-Induced Compressive Residual Stresses: Surface Shielding Effect and Consequences for $\sqrt{\text{Area}}$-Model Validation

As shown in Section 3.6, substantial—and in some cases deep-ranging—CRS remain in the fatigue specimens after finish-machining (hard turning with PCBN) and subsequent surface polishing (LP/AP). Comparable states of fiRS, including pronounced specimen-to-specimen scatter, subsurface CRS maxima, and depth-dependent sign changes, have been reported for hard, high-strength steels. A broader compilation of literature findings on fiRS generation and their likely fatigue implications is provided in Table S12 and Figures S20–S25 [71, 72, 76, 78, 98, 136–138, 140, 147–150, 176–180, 194–201]. Because the fatigue-relevant profiles here are predominantly compressive, the following discussion focusses on fiCRS.

Outeiro [150] reported surface-near fiRS in axial and circumferential directions for hard milling and orthogonal turning of AISI H13, AISI 52100, and AISI D2 (IC + HW), consistent with findings by Jomaa et al. [149] and Caruso et al. [148] (modified replots in Figures S20 and S21). Across these studies, the fiRS magnitude and penetration depth depend primarily on machining parameters and cutting tool state, notably:

- Cutting speed V_C, feed rate f, chip thickness h, tool wear state and cooling conditions;
- Tool material (PCBN vs. SCC), edge geometry, rake/clearance angle, flank wear land width;
- Material state (hardness, hard-phase fraction) and white/dark layer formation.

A key conclusion from Outeiro [150] is that increasing cutting speed, higher hardness/hard-phase fraction, and progressive tool wear generally increase the surface CRS level $\sigma_{CRS,d_S=0}$, increase/shift the maximum $\sigma_{CRS,max}$, and move the zero-crossing depth $d_{S,\sigma_{CRS}\approx 0}$ deeper into the material (Figures S20 and S21). The resulting sign at the surface (CRS vs. TRS) and the depth progression reflect coupled contributions of heterogeneous plastic deformation and heat generation/transport [150]. The scatter observed in the present fiRS results (Figures 18 and 19) is consistent with this process sensitivity: in serial machining, parameters are not perfectly constant, tool edges evolve from new to worn, and manual LP is intrinsically operator-dependent; AP is more reproducible but still introduces batch-to-batch and specimen-to-specimen variability, partly inherited from scatter in the preceding hard-turning step. These effects plausibly explain the observed scatter, circumferential nonuniformity (A vs. B), and differences in depth-profile shape between steels/conditions in Section 3.6 (Figures 18 and 19). Reported fatigue effects of fiCRS in hard steels are mixed; this is expected and discrepancies

1869344x, 2026, 10, Downloaded from https://onlinelibrary.wiley.com/doi/10.1002/srin.202501039 by Universitatsbibliothek RWTH Aachen University, Wiley Online Library on [05/11/2026]. See the Terms and Conditions (https://onlinelibrary.wiley.com/terms-and-conditions) on Wiley Online Library for rules of use; OA articles are governed by the applicable Creative Commons License

are understandable because the response depends on loading mode (axial vs. bending), the defect population, and the concrete CRS profile present (surface value, subsurface maximum depth, and decay length). Examples include:

- Large beneficial shifts under axial loading: Sohar et al. [71, 72] reported an ≈32% strength shift in UHCF axial loading ($N_G = 10^{10}$) for D2 IC when comparing high versus very low fiCRS, associated with a crack-mode shift and suppression of internal mechanisms (incl. the disappearance of granular bright facet (GBF)-related V-modes reported by Shiozawa et al. [176, 177]).
- Moderate beneficial shifts after surface treatment: Scholl et al. [98] reported ≈6%–16% increases in HCF strength under RBT ($N_G = 10^7$) for D2 and M2/M3 steels after diffusion-layer plasma nitriding (PN) and concluded that CRS effects also depended on defect populations and probabilistic activation in the HLV, and thus (slightly) differed for PM-HIP versus IC steels.
- Conflicting outcomes after nitriding-type treatments: Hirano et al. [194] reported an ≈23% increase in LLF strength and mode shifts for a carbide-rich HSS, whereas Farrahi & Ghadbeigi [195] reported decreases of about 8%–30% after nitrocarburizing (NC) and about 50% after gas nitriding (GN) for single-stage-tempered AISI D3 steel at 50 HRC.
- Duplex S–N behavior largely preserved in bending: Shimatani et al. [196–198] and Shiozawa et al. [176–180] reported duplex S–N curves under RBT ($N_G = 10^9$) for both high/deep fiCRS and low fiCRS; they argued that CRS mainly affected the surface-dominated branch—particularly when internal defects were very small/rare (i.e., high cleanliness)—while internal V-modes dominated the VHCF tail and were less sensitive unless fiCRS were extremely deep [176–180, 196–198].

Under RBT, the stress amplitude is strongly nonuniform across the cross-section. The local tensile amplitude at a defect depends on its distance from the surface edge fiber (Figures S22 and S23). When surface-near CRS are superimposed on this bending stress field, the effective tensile amplitude at surface/contact defects can be reduced markedly, while deeper defects experience less reduction depending on the CRS progression and penetration depth (Figures S22 and S23). Consequently, fiCRS can:

- Suppress surface-controlled (S/C) initiation (designated and understood as surface shielding),
- Promote internal (V) fatigue crack initiation when sufficiently large internal defects exist, and
- Shift the dominant crack-initiation site depending on (i) CRS magnitude and CRS penetration depth, (ii) defect-size extremes and their spatial distribution, and (iii) the applied stress level.

This surface shielding effect (SSE) is expected to be more pronounced under bending/torsion than under axial loading, consistent with reports that CRS mainly shift the surface-controlled branch in duplex S–N behavior under bending, while internal modes are less affected unless CRS are exceptionally deep [176–180, 196–198]. In the present work, the semi-quantitative SSE illustrations in Figure 22a–f together with the schematic illustrations in Figures S22 and S23 summarize how, for identical nominal stresses, different CRS profiles can change which defect position (S/C vs. V) is most likely to activate depending on the relative defect sizes d_1–d_4 and their locations. This supports the interpretation that fiCRS can shift apparent LLF strength and alter crack-initiation statistics under RBT, consistent with fatigue-life shifts at higher CRS reported for notched steels after carburizing vs. carbonitriding by Parrish [136] (Figure S24a) and above-mentioned LLF strength shifts [71, 72, 98].

Sections 4.1–4.3 showed that defect size ($\sqrt{\text{area}_{max}}$) and hardness alone cannot fully explain (i) the unusually steep positive hardness slopes for V10 PM-L$^{3/2}$ (and D2 PM-L) and (ii) the missing RHE-type reversal for V10 PM-L^1 despite very large $\sqrt{\text{area}_{max}}$. The measured fiRS profiles provide a plausible additional FIF:

- CRS can elevate the apparent LLF strength by reducing the effective tensile amplitude at near-surface defects (particularly relevant under RBT for run-outs of PM-HIP steels).
- If CRS magnitude and/or CRS depth range vary with hardness and finishing route, the apparent hardness slope data can be steepened (consistent with Outeiro's [150] parameter sensitivities reported for orthogonal hard turning).
- For high-defect-amount and large-defect-size microstructures, CRS can attenuate or mask an RHE-type reversal by shifting the activated defect population toward deeper sites and changing which extremes dominate crack initiation (relevant for V10 PM-L^1).

This interpretation is consistent with the fiRS results in Section 3.6: (i) large specimen-to-specimen scatter observed, (ii) circumferential nonuniformity (A vs. B), and (iii) distinct depth-profile shapes depending on steel condition (hardness; carbide fraction) and finishing route, despite similarly low SR obtained after polishing. Further support for SSE comes from the database-driven validation of Murakami's [116, 118] $\sqrt{\text{area}}$ fatigue-limit model (Section 3.5; Tables 13 and S11). Because the model does not include CRS or SSE explicitly, systematic misclassification patterns can indicate unmodeled surface-integrity effects:

- PM-HIP configurations (V10 and D2 PM-L): fractures are predicted very well ($\xi_{max} \approx 7\% \pm 7\%$), consistent with the nominal ±10% accuracy band, but run-outs are predicted poorly ($\xi_{max} \approx 49\% \pm 17\%$; misclassification rate ≈84%). This asymmetry is consistent with survivors being shifted to higher apparent endurance by CRS/SSE—i.e., the effective σ_L at critical defects is reduced by CRS not represented in the model.
- IC configurations (D2 HW-L/-T): fracture-side errors are larger ($\xi_{max} \approx 21\% \pm 12\%$), and ≈26% of both fractures and run-outs are misclassified. A substantial part of fracture-side mismatches is associated with D2 HW-T at higher hardness, where an RHE-type reversal occurs; this is expected because the $\sqrt{\text{area}}$ model does not capture RHE explicitly, and implementing a defect-size-dependent,

1869344x, 2026, 10, Downloaded from https://onlinelibrary.wiley.com/doi/10.1002/srin.202501039 by Universitatsbibliothek RWTH Aachen University, Wiley Online Library on [05/11/2026]. See the Terms and Conditions (https://onlinelibrary.wiley.com/terms-and-conditions) on Wiley Online Library for rules of use; OA articles are governed by the applicable Creative Commons License

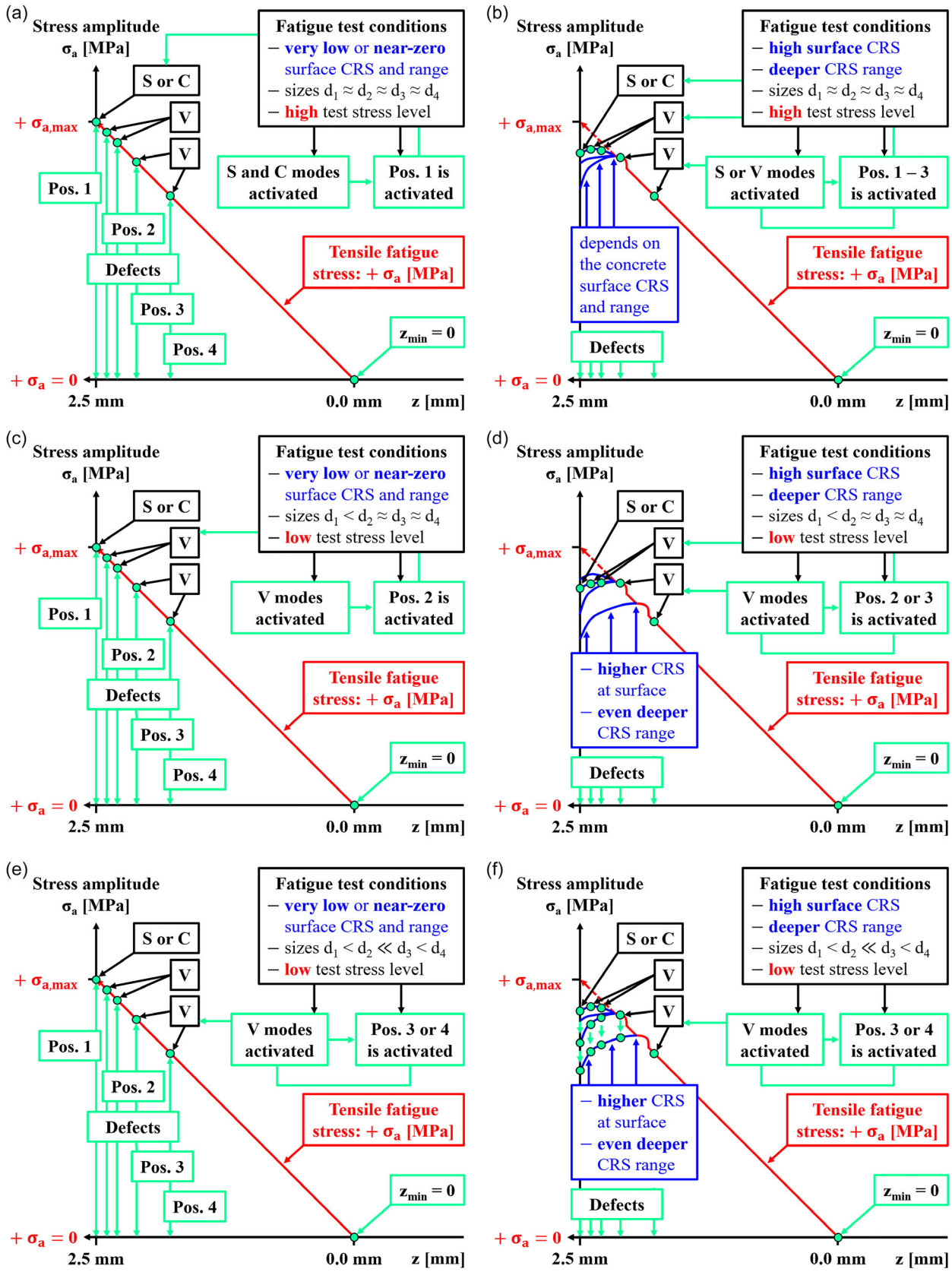

FIGURE 22 | Conceptual illustration of surface shielding effect (SSE) under RBT due to fiCRS (see also the schematic illustrations for the specimen cross-section under RBT in Figures S22 and S23 with corresponding explanations). Superposition of a bending stress gradient with an idealized CRS depth profile preferentially reduces the effective tensile amplitude at surface/contact defects, thereby biasing crack initiation toward deeper V defects depending on defect size/localization and CRS magnitude, progression, and penetration depth.

1869344x, 2026, 10, Downloaded from https://onlinelibrary.wiley.com/doi/10.1002/srin.202501039 by Universitatsbibliothek RWTH Aachen University, Wiley Online Library on [05/11/2026]. See the Terms and Conditions (https://onlinelibrary.wiley.com/terms-and-conditions) on Wiley Online Library for rules of use; OA articles are governed by the applicable Creative Commons License

material-specific RHE would reduce the model's simplicity and practical applicability [116, 118]. Run-out mismatches can also be attributed to SSE from superimposed CRS, but since the amount of potentially-critical carbide defects in deeper volume is much higher for IC steels (probability for encountering other defects), the shifts due to SSE appear less pronounced/different than for PM-HIP steels [98].

Overall, the validation pattern is consistent with two superimposed limitations: (i) RHE-type behavior is not included in the $\sqrt{\text{area}}$ model, and (ii) finishing-induced CRS/SSE can strongly bias run-out behavior under bending, particularly for PM-HIP steels whose critical defects are smaller and less densely distributed in the HLV than the carbide populations in IC steels (cf. Figures 6, S3, and 9–11). A quantitative correction of the fatigue data for fiCRS is not justified here because (i) RS depth profiles were measured only for selected specimens, (ii) RS vary circumferentially and between specimens, and (iii) RS relax under cyclic loading (are metastable states), with relaxation depending on stress amplitude, cycle count, and initial CRS magnitude [136, 137, 196–198]. Relevant literature replots on CRS relaxation originally from Wiegand & Tolasch [202], as later reproduced by Parrish [136, 137], and originally from Shimatani et al. [196–198] are given in Figures S24b and S25a,b. Without specimen-wise RS histories (including relaxation), it is not defensible to back-calculate near-zero-RS LLF strengths or to correct individual misclassified points in the $\sqrt{\text{area}}$ model validation.

For IC steels, applying Murakami's [116, 118] effective projected area, $\sqrt{\text{area}_{\text{eff}}}$, for irregularly shaped carbides ($\sqrt{\text{area}_{\text{eff}}} \geq \sqrt{\text{area}}$; Figures S4 and S5) could probably improve prediction for some misclassified fractures, as also noted particularly for AM materials without HIP by Murakami [116, 118]. However, for PM-HIP run-outs the dominant issue is that points lie above the model prediction band $\sigma_N \approx 1.0 \pm 0.1$ (apparent endurance elevated), so substituting $\sqrt{\text{area}_{\text{eff}}}$ would not resolve the run-out misclassifications shown in the normalized S–N curves.

Two practical conclusions follow: Firstly, surface integrity must be treated as a primary design/test variable for fatigue assessment of carbide-rich CWS. Secondly, for engineering-reproducible fatigue testing and model validation, controlled and verifiable surface states are needed, ideally including (i) a near-zero/low RS reference state and (ii) defined CRS profiles representative of relevant finishing/surface treatments (e.g., hard machining, polishing, nitriding, microshot peening), verified by standardized XRD surface measurements and selected depth profiles. From an experimental standpoint, this motivates time- and cost-efficient automated finishing/polishing routes that reproducibly achieve a desired RS state (either removing machining CRS completely without reintroducing new CRS, or generating a specifically controlled, reproducible CRS profile). Automated drag finishing can be promising, but requires process development and validation (material removal depth vs. time, suitable media selection, accompanying XRD and SR checks, and fiRS reproducibility assessment).

Taken together, normalized S–N curves (Figures 12 and 13), $\sqrt{\text{area}}$ fatigue-model validation results (Tables 13 and S11), and semi-quantitative SSE schematics (Figures 22, S22, and S23) suggest that CRS/SSE shifts of the order reported in the literature (≈6%–32% [71, 72, 98] in some cases) are plausible for the present RBT datasets. Such shifts provide a coherent explanation for the two key inconsistencies highlighted in Table 12: (i) hardness-fit slopes for V10 PM-L$^{3/2}$ and D2 PM-L exceeding drilled-hole reference trends from Murakami & Endo [116, 118, 119], and (ii) the apparent suppressions of RHE-type behavior in V10 PM-L^{1} despite very large $\sqrt{\text{area}_{\text{max}}}$.

4.5 | Fatigue-Oriented Design of Hard, Wear-Resistant Tools for Cold-Work Applications

Sections 3.1–3.6 and 4.1–4.4 address the experimental-data and mechanistic-knowledge gaps for carbide-rich CWS in the high-hardness regime by providing a statistically robust fatigue–defect database and quantitative PSPP correlations with systematic variation of steelmaking route, microstructure, HT, and intrinsic defect populations. Within this framework, an RHE-type reversal proposed by Garwood et al. [96] and Murakami [116, 118] (Figure 3a,b) was experimentally confirmed for at least one real manufacturing-related defect population at comparable $\sqrt{\text{area}_{\text{max}}}$, and the PSPP correlation in Figure 16 indicates that the schematic 3D concept by Berns [141] (Figure 4) is transferable to hardness- and defect-size-controlled fatigue behavior in hard, carbide-rich steels. Murakami's [116, 118] $\sqrt{\text{area}}$ model was assessed using normalized S–N curves (Figures 12 and 13) and database-driven error validation.

Overall, the $\sqrt{\text{area}}$ model is a physically well-founded, fracture-mechanics-based framework that is suitable as a basis for fatigue-oriented assessment/design of highly wear-resistant cold-work tools. Deviations and misclassifications observed here can be considered consistent with two limitations outside the model's original scope: (i) no explicit representation of defect-size-dependent RHE-type reversals and (ii) no consideration of SSE caused by fiCRS. However, the $\sqrt{\text{area}}$ model can serve in practice not only as a design tool for defect-controlled fatigue assessment, but also as a diagnostic indicator for non-ideal fatigue test or surface-integrity conditions—e.g., specimen distortion/misalignment causing unintended bending components, or fiCRS shifting apparent endurance via SSE.

A remaining practical limitation is that the relaxation mechanisms of fiCRS are still not fully resolved, as noted by Sohar et al. [72] and Shimatani et al. [196–198]. A plausible interpretation is microplasticity and microcrack formation/arrest at non-critical microstructural sites (e.g., quenched-in microcracks in hard martensitic matrices that become nonpropagating), consistent with Murakami's [116, 118] small-crack framework. In that sense, early small-crack evolution toward arrest may contribute to CRS relaxation without macroscopically visible plasticity. From an engineering-design perspective, fatigue-oriented design with carbide-rich CWS should explicitly consider:

- Manufacturing route and defect extremes as primary design inputs: For hard, defect-containing steels, defect-size extremes ($\sqrt{\text{area}_{\text{max}}}$; extreme-value distribution) govern LLF behavior. Design allowables should therefore be tied to cleanliness/defect-extreme characterization rather than nominal composition or NMI metrics alone [116, 118, 141].

1869344x, 2026, 10, Downloaded from https://onlinelibrary.wiley.com/doi/10.1002/srin.202501039 by Universitatsbibliothek RWTH Aachen University, Wiley Online Library on [05/11/2026]. See the Terms and Conditions (https://onlinelibrary.wiley.com/terms-and-conditions) on Wiley Online Library for rules of use; OA articles are governed by the applicable Creative Commons License

- Anisotropy and notch sensitivity: HW (e.g., forging/rolling) can generate microstructural and mechanical anisotropy, which must be reflected in design allowables and orientation-specific assessment (cf. Alatarvas et al. [203], Yang et al. [204], Wollenweber et al. [205], Sundin & Reis [206], and Chychko et al. [207]). Notch effects are practically unavoidable and should be treated explicitly (cf. Jung [11]).
- Potential absence of a practical fatigue limit in the gigacycle regime: Hard (ultra-)high-strength steels—including carbide-rich CWS—often exhibit type IV S–N behavior and can fail beyond conventional HCF/VHCF, as documented up to 10^9–10^{10} cycles (cf. Sohar et al. [71–80], Bergström et al. [89], Shiozawa et al. [176–180], and Furuya et al. [208–210]). The nonpropagating condition for small cracks/defects is hardness-dependent, and tolerable/critical defect sizes (d_t, d_c) decrease with increasing hardness (cf. Figures 4 and S14–S18) [116, 118, 141].
- Design is typically finite-life, not infinite-life regime: Cold-work tools usually operate in LCF–HCF ranges ($\sim 10^3$–$10^{6/7}$), whereas V/UHCF is uncommon for expensive high-alloy tooling steels and their high service loading in practical applications. Consequently, fatigue design commonly targets N_{Fracture} rather than a strict endurance limit.
- Wear–fatigue interactions are unavoidable: Cold-work tools ultimately require overhaul/replacement due to wear-induced surface degradation (surface quality and dimensional accuracy). Design should couple abrasion-dominated wear resistance (carbide fraction/morphology) with fatigue safety against premature fracture, recognizing that wear-induced surface degradation interacts with fatigue (surface defects and RS states).
- Surface integrity as a design variable (not a test artifact): fiCRS can increase apparent endurance via SSE and can mask RHE-type reversals; design/qualification should either control surface integrity to a defined state or include it as an explicit factor (e.g., near-zero RS reference vs. representative RS-treated condition resulting from production and surface finishing).

A practical direction for future work is the development and validation of a probabilistic fatigue-oriented design concept for wear-resistant cold-work tools in the high-hardness regime that integrates (i) defect extreme-value statistics, (ii) hardness dependence including defect-size-controlled reversals, and (iii) anisotropy/notch/temperature effects—aligned with current (probabilistic) cyclic design efforts for PM/AM materials in refs. [211–217].

5 | Conclusion

For high-alloy, carbide-rich CWS, the database-driven results lead to the following conclusions:

1. Dominant FIF: defect-size extremes. LLF performance is governed primarily by the extreme-value distribution of intrinsic crack-initiating defects expressed by Murakami's [116, 118] $\sqrt{\mathrm{area}}$ parameter (especially $\sqrt{\mathrm{area}_{\mathrm{max}}}$), which is controlled mainly by steelmaking and subsequent HW (forging/rolling) and must be minimized to increase fatigue strength.

2. IC steels: carbide sizes control LLF strength. For ingot-cast steels, the dominant crack initiators are eutectic and/or primary carbides; hence, LLF strength is governed primarily by the effective carbide size scale (cf. Figure S2), which can be reduced by increased hot-working degree φ and/or remelting techniques (and associated microstructural refinement).

3. PM-HIP steels: cleanliness and suppression of clustering/agglomeration are decisive. For PM-HIP routes, steel cleanliness (with emphasis on macroinclusion extremes from slag entrainments and scrap) together with the carbide size scale—especially avoiding carbide coarsening, clustering, and multiphase agglomerates—constitute the controlling FIFs.

4. Hardness trends and RHE-type behavior: The derived hardness (PSPP) correlations confirm the generally positive hardness influence on LLF strength for small-to-intermediate defect sizes, but also demonstrate an RHE-type reversal once sufficiently large defect extremes govern crack initiation (verified here for large and sharp-edged eutectic M_7C_3 carbide defects contained in the microstructure of D2 IC).

5. Surface integrity is not neutral: Substantial fabrication- and finishing-induced near-surface (compressive) residual stresses (fiCRS) remain after specimen fabrication; their magnitudes can vary between individual fatigue specimens and bias apparent fatigue trends and RHE-type reversal with hardness.

6. Consistency with Murakami & Endo [119] and interpretation of outliers: The fitted hardness slopes, the occurrence of the RHE, and the associated critical defect sizes are consistent with the defect-size-dependent trends reported by Murakami & Endo [119]. Cases exhibiting steeper-than-expected positive slopes can be plausibly explained by superimposed near-surface fiCRS, which increase the apparent endurance limit through surface shielding effects. This interpretation is further supported by run-out outliers in the normalized S–N curves.

7. Pathway to superior fatigue performance at high hardness/carbide content: Superior LLF performance at high hardness and high carbide content is achievable when PM-HIP steelmaking with very high cleanliness (clean atomization and powder handling, minimized sulfurization) is combined with increased hot-working degree φ, thereby suppressing pronounced carbide coarsening/clustering and multiphase defect agglomerates.

8. Quantitative cleanliness targets for high fatigue strength under RBT: To achieve HCF/LLF strength levels above $\sim$1,000 MPa in RBT with PM-HIP steels, cleanliness

1869344x, 2026, 10, Downloaded from https://onlinelibrary.wiley.com/doi/10.1002/srin.202501039 by Universitatsbibliothek RWTH Aachen University , Wiley Online Library on [05/11/2026]. See the Terms and Conditions (https://onlinelibrary.wiley.com/terms-and-conditions) on Wiley Online Library for rules of use; OA articles are governed by the applicable Creative Commons License

control is required such that intrinsic defect extremes satisfy about $\sqrt{area}_{max} \leq 60\ \mu m$ (D2 PM-L; cf. Tables 9, 12, S9, and S10). For still higher strength levels, defect extremes should be reduced toward about $\sqrt{area}_{max} \leq 20\ \mu m$ (V10 PM-L[3]; cf. Tables 10, 12, S9, and S10).

9. Economic relevance of super-clean PM-HIP grades: Super-clean, carbide-rich PM-HIP grades can be economically advantageous in massive cold-forming applications because high cleanliness combined with fatigue-oriented tool design—based on statistically validated fatigue and defect data as established here—can improve tool life and process reliability despite higher material cost. Reduced premature fatigue failures, downtime, and maintenance effort may therefore outweigh the material cost premium (cf. Jung [11] regarding productivity and cost-efficiency considerations). Realizing these gains requires reliable service-loading data, representative FEM-based tool-stress analysis, and statistically robust cyclic material parameters.

Acknowledgments

The authors gratefully acknowledge the support of Dr.-Ing. A. Barani and Dr.-Ing. A. Das (ZAPP Precision Metals GmbH, Unna), Dr.-Ing. S. Sundin (Erasteel SAS, Söderfors), Dipl.-Ing. M. Gürcan and Dipl.-Ing. S. Hausherr (Deutsche Edelstahlwerke Specialty Steel GmbH, Witten), Prof. Dr.-Ing. C. Escher and Dipl.-Ing. M. Tradt (Dörrenberg Edelstahl GmbH, Engelskirchen), Dr. I. Jung and Dr. A. Schürmann (voestalpine High Performance Metals Deutschland GmbH, Düsseldorf), Dr.-Ing. C. Turk and Dr.-Ing. G. Jesner (voestalpine Böhler Edelstahl GmbH, Kapfenberg), Dr.-Ing. G. Walkowiak and Dipl.-Ing. U. Schwahn (Bodycote Heat Treatment GmbH, Esslingen), M. Sc. L. Dettmann and Dipl.-Ing. N. Petri (OTEC Präzisionsfinish GmbH, Straubenhardt), and Dr.-Ing. H. Hill, M. Sc. J. Conrads, and M. Sc. P. Kluge (Deutsche Edelstahlwerke Specialty Steel GmbH, Krefeld) for providing material supplies, heat treatments with hardness testing, automated polishing/drag finishing, and for valuable technical discussions throughout this work. We are particularly grateful to Univ.-Prof. Dr.-Ing. P. Beiss (RWTH Aachen University, IWM) for his inspiring support and the intensive discussions of the results. Furthermore, we sincerely thank S.-J. Abraham, C. Schlieker, N. Vandenwyngaert, Dipl.-Ing. F. Klubberg and Dr.-Ing. K. Burkamp (RWTH Aachen University, IWM), as well as T. Tix, M. Bollenbach, D. Magel, and C. May (RWTH Aachen University, MTI) for their continuous assistance and dedicated efforts.

Open Access funding enabled and organized by Projekt DEAL.

Author Contributions

Lennart Mirko Scholl: conceptualization (lead), data curation (lead), formal analysis (lead), funding acquisition (lead), investigation (lead), methodology (lead), software (lead), project administration (lead), resources (lead), supervision (equal), validation (lead), visualization (lead), writing – original draft (lead), writing – review & editing (equal). **Frederik Tegeder**: conceptualization (supporting), data curation (supporting), formal analysis (supporting), investigation (supporting), methodology (supporting), software (supporting), project administration (supporting), writing – review & editing (supporting). **Dhirendar Chauhan**: data curation (supporting), investigation (supporting), methodology (supporting), software (supporting), validation (supporting), writing – review & editing (supporting). **Bengt Hallstedt**: conceptualization (supporting), formal analysis (supporting), methodology (supporting), supervision (supporting), visualization (supporting), writing – review & editing (supporting). **Tobias Hajeck**: conceptualization (supporting), software (supporting), project administration (supporting), supervision (supporting), visualization (supporting), writing – review & editing (supporting). **Alexander Bezold**: conceptualization (supporting), funding acquisition (supporting), project administration (supporting), supervision (equal), writing – review & editing (equal). **Christoph Broeckmann**: conceptualization (supporting), funding acquisition (supporting), supervision (equal), writing – review & editing (equal).

Funding

The research projects IGF-No. 20356N/FOSTA P 1322 and IGF-No. 01IF22271N/FOSTA P 1608 from the "Research Association for Steel Application e. V." (FOSTA), Düsseldorf, Germany were supported and publicly funded by the Federal Ministry of Economic Affairs and Climate Action (BMWK), Berlin/Bonn, Germany through the project management sponsor/Projektträger "Deutsches Zentrum für Luft- und Raumfahrt e. V." (DLR), Bonn, Germany as part of the program for promoting Industrial Cooperative Research (IGF) on the basis of a decision by the German Bundestag.

Conflicts of Interest

The authors declare no conflicts of interest.

Data Availability Statement

Additional supporting figures, tables, and data are provided in the attached Supporting Information (SI) document, including supplementary statistical evaluations, metallographic analysis, EDS results, and overviews of the abbreviations, symbols, and units used in the manuscript. Further experimental data are available from the authors upon reasonable request.

References

1. M. S. Kenevisi, F. S. Gobber, P. Fino, et al., "Tool Steels and Their Additive Manufacturing for Fabrication and Repair via PBF and DED Processes: Techniques, Challenges, and Applications," *Materials & Design* 258 (2025): 114639, https://doi.org/10.1016/j.matdes.2025.114639.

2. I. Picas, "Mechanical Behaviour of Tools for Shearing Ultra High-Strength Steels: Influence of the Microstructure on Fracture and Fatigue Micro-Mechanisms of Tool Steels and Evaluation of Micro-Mechanical Damage in Tools," (PhD thesis (doctoral diss.), Departament de Ciència dels Materials i Enginyeria Metallúrgica, Universitat Politècnica de Catalunya, 2012).

3. M. R. Krishnadev and S. C. Jain, "Improved Productivity through Failure Analysis: Case Studies in Precision Forging of Aerospace Components," *Engineering Failure Analysis* 14, no. 6 (2007): 1053–1064, https://doi.org/10.1016/j.engfailanal.2006.11.056.

4. M. Dubar, L. Dubar, A. Dubois, A. Verleene, and J. Oudin, "Wear Criteria of Cold Forging Tools," *Surface Engineering* 17, no. 2 (2001): 119–122, https://doi.org/10.1179/026708401101517692.

5. M. Boniardi, F. D'Errico, and C. Tagliabue, "Influence of Carburizing and Nitriding on Failure of Gears – A Case Study," *Engineering Failure Analysis* 13, no. 3 (2006): 312–339, https://doi.org/10.1016/j.engfailanal.2005.02.021.

6. S. Y. Luo, "Effect of the Geometry and the Surface Treatment of Punching Tools on the Tool Life and Wear Conditions in the Piercing of Thick Steel Plate," *Journal of Materials Processing Technology* 88, no. 1–3 (1999): 122–133, https://doi.org/10.1016/S0924-0136(98)00375-6.

7. T. O. Pedersen, "On the Local Damage Development in Cold-Forging Tools," in Transactions of the 14th International Conference on Structural Mechanics in Reactor Technology/SMiRT: 17–22, 1997.

8. Y. Nagao, M. Knoerr, and T. Altan, "Improvement of Tool Life in Cold Forging of Complex Automotive Parts," *Journal of Materials Processing Technology* 46, no. 1–2 (1994): 73–85, https://doi.org/10.1016/0924-0136(94)90103-1.

1869344x, 2026, 10, Downloaded from https://onlinelibrary.wiley.com/doi/10.1002/srin.202501039 by Universitatsbibliothek RWTH Aachen University, Wiley Online Library on [05/11/2026]. See the Terms and Conditions (https://onlinelibrary.wiley.com/terms-and-conditions) on Wiley Online Library for rules of use; OA articles are governed by the applicable Creative Commons License

9. M. P. Pereira, J. L. Duncan, W. Yan, and B. F. Rolfe, "Contact Pressure Evolution at the Die Radius in Sheet Metal Stamping," *Journal of Materials Processing Technology* 209, no. 7 (2009): 3532–3541, https://doi.org/10.1016/j.jmatprotec.2008.08.010.

10. B. Högman, "Blanking of Ultra High-Strength Steel Sheet," in Proceedings of the 6th International Tooling Conference, pub. J. Bergström (Karlstad University, 2002), 203–216.

11. I. Jung, "Ermüdungsfestigkeit Hochlegierter Werkzeugstähle," *HTM Journal of Heat Treatment and Materials* 65, no. 5 (2010): 278–284, https://doi.org/10.3139/105.110074.

12. W. Reiss, "Bruch und Verschleiß von Umformwerkzeugen," *VDI-Zeitschrift* 130, no. 1 (1988): 56–62.

13. S. Marsoner, "Gefügeeinfluss auf statische und zyklische Eigenschaften von PM-Werkzeugstahl," (PhD thesis (doctoral diss.), Faculty of Materials Science, Montanuniversität Leoben, 2002).

14. G. Jesner, "Ermüdungsverhalten von hochfesten PM-Werkzeugstählen für die Kaltmassivumformung," (PhD thesis (doctoral diss.), Faculty of Materials Science, Montanuniversität Leoben, 2007).

15. B. Freitas, V. Richhariya, M. Silva, A. Vaz, S. F. Lopes, and Ó. Carvalho, "A Review of Hybrid Manufacturing: Integrating Subtractive and Additive Manufacturing," *Materials* 18, no. 18 (2025): 4249, https://doi.org/10.3390/ma18184249.

16. N. P. V. Sebbe, F. Fernandes, V. F. C. Sousa, and F. J. G. Silva, "Hybrid Manufacturing Processes Used in the Production of Complex Parts: A Comprehensive Review," *Metals* 12, no. 11 (2022): 1874, https://doi.org/10.3390/met12111874.

17. W. Grzesik, "Hybrid Additive and Subtractive Manufacturing Processes and Systems: A Review," *Journal of Machine Engineering* 18, no. 4 (2018): 5–24, https://doi.org/10.5604/01.3001.0012.7629.

18. M. Merklein, D. Junker, A. Schaub, and F. Neubauer, "Hybrid Additive Manufacturing Technologies – An Analysis regarding Potentials and Applications," *Physics Procedia* 83 (2016): 549–559, https://doi.org/10.1016/j.phpro.2016.08.057.

19. J. Anwar, E. Bassini, P. Fino, et al., "A Review on near Net Shape Hot Isostatic Pressing of Metallic Materials: For Industrial Applications," *Journal of Materials Research and Technology* 42 (2026): 3663–3684, https://doi.org/10.1016/j.jmrt.2026.03.210.

20. F. Großwendt, A. Strauch, J. Lentz, et al., "A Novel Approach on Rapid Alloy Development of Tool Steels for Laser Powder Bed Fusion by In Situ Alloying," *Advanced Engineering Materials* 27, no. 14 (2025): 2402253, https://doi.org/10.1002/adem.202402253.

21. P. Widomski, M. Kaszuba, D. Dobras, D. Terefinko, and M. Kolodzinski, "Comparative Study of Different Additive Manufacturing Methods for H13 Tool Steel," *Materials* 18, no. 23 (2025): 5299, https://doi.org/10.3390/ma18235299.

22. T. Kelliger, M. Meurer, and T. Bergs, "Potentials of Additive Manufacturing for Cutting Tools: A Review of Scientific and Industrial Applications," *Metals* 14, no. 9 (2024): 982, https://doi.org/10.3390/met14090982.

23. S. Bergmüller, L. Kaserer, L. Fuchs, et al., "Crack-Free In Situ Heat-Treated High-Alloy Tool Steel Processed via Laser Powder Bed Fusion: Microstructure and Mechanical Properties," *Heliyon* 8, no. 8 (2022): e10171, https://doi.org/10.1016/j.heliyon.2022.e10171.

24. E. Iakovakis, M. J. Roy, M. Gee, and A. Matthews, "Evaluation of Wear Mechanisms in Additive Manufactured Carbide-Rich Tool Steels," *Wear* 462–463 (2020): 203449, https://doi.org/10.1016/j.wear.2020.203449.

25. S. Choi, H. Kim, J. Sung, D. Lee, and J. Seo, "Properties of Tool Steels Printed by Direct Energy Deposition Process on S45C Base Metal," *Materials* 13, no. 22 (2020): 5068, https://doi.org/10.3390/ma13225068.

26. K. Geenen, A. Röttger, F. Feld, and W. Theisen, "Microstructure, Mechanical, and Tribological Properties of M3:2 High-Speed Steel Processed by Selective Laser Melting, Hot-Isostatic Pressing, and Casting," *Additive Manufacturing* 28 (2019): 585–599, https://doi.org/10.1016/j.addma.2019.05.028.

27. J. Saewe, C. Gayer, L. Jauer, J. Kunz, and C. Broeckmann, "Feasibility Investigation for Laser Powder Bed Fusion of High-Speed Steels," in Proceedings of the Euro PM2018 Congress & Exhibition (European Powder Metallurgy Association, 2020).

28. J. Saewe, "Untersuchungen der Verarbeitbarkeit des Schnellarbeitsstahls HS6-5-3-8 mittels Laser Powder Bed Fusion," (PhD thesis (doctoral diss.), Faculty of Mechanical Engineering, RWTH Aachen University, 2022).

29. M. Franke-Jurisch, M. Mirz, T. Wenz, A. Kirchner, B. Klöden, and T. Weißgärber, "PBF-EB of Fe-Cr-V Alloy for Wear Applications," *Materials* 15, no. 5 (2022): 1679, https://doi.org/10.3390/ma15051679.

30. F. Tegeder, L. M. Scholl, S. Wieland, et al., "Fatigue Strength in Additive Toolmaking: A Study of Metal Binder Jetting and Electron Beam Melting for Processing Carbide-Rich Cold-Work Tool Steels," in Proceedings of the 13th International Tooling Conference (Austrian Society for Metallurgy and Materials, 2025), 166–178.

31. F. Tegeder, L. M. Scholl, S. Wieland, et al., "Fatigue Strength in Additive Toolmaking: A Study of Metal Binder Jetting and Electron Beam Melting for Processing Carbide-Rich Cold-Work Tool Steels," *Steel Research International* (2026): 202500658, https://doi.org/10.1002/srin.202500658.

32. J. Kunz, J. Saewe, S. Herzog, A. Kaletsch, J. H. Schleifenbaum, and C. Broeckmann, "Mechanical Properties of High-Speed Steel AISI M50 Produced by Laser Powder Bed Fusion," *Steel Research International* 91, no. 5 (2020): 1900562, https://doi.org/10.1002/srin.201900562.

33. J. Kunz, M. L. Köhler, S. Herzog, A. Kaletsch, and C. Broeckmann, "Influence of an Increasing Alloying Content on the Microstructure of a High-Speed Steel in the Laser-Powder Bed Fusion Process," *Steel Research International* 92, no. 12 (2021): 2100438, https://doi.org/10.1002/srin.202100438.

34. J. Kunz, S. Herzog, A. Kaletsch, and C. Broeckmann, "Influence of Initial Defect Density on Mechanical Properties of AISI H13 Hot-Work Tool Steel Produced by Laser Powder Bed Fusion and Hot Isostatic Pressing," *Powder Metallurgy* 65, no. 1 (2022): 1–12, https://doi.org/10.1080/00325899.2021.1934634.

35. S. Qin, Y. Bo, S. Herzog, B. Hallstedt, A. Kaletsch, and C. Broeckmann, "Influence of Process Parameters on Porosity and Hot Cracking of AISI H13 Fabricated by Laser Powder Bed Fusion," *Powders* 1, no. 3 (2022): 184–193, https://doi.org/10.3390/powders1030012.

36. S. Qin, S. Herzog, A. Kaletsch, and C. Broeckmann, "Improving the Fatigue Strength of Laser Powder Bed-Fused AISI M3:2 by Hot Isostatic Pressing," *Steel Research International* 94, no. 4 (2023): 2200435, https://doi.org/10.1002/srin.202200435.

37. S. Qin, J. Saewe, J. Kunz, et al., "Influence of Preheating Temperature on Microstructure Evolution and Hardness of High-Speed Steel AISI M50 Processed by Laser Powder Bed Fusion," *Steel Research International* 94, no. 6 (2023): 2200784, https://doi.org/10.1002/srin.202200784.

38. I. Raffeis, F. Adjei-Kyeremeh, S. Ewald, J. H. Schleifenbaum, and A. Bührig-Polaczek, "A Combination of Alloy Modification and Heat Treatment Strategies toward Enhancing the Properties of LPBF Processed Hot Working Tool Steels (HWTS)," *Journal of Manufacturing and Materials Processing* 6, no. 3 (2022): 63, https://doi.org/10.3390/jmmp6030063.

39. F. Lei, T. Wen, F. Yang, et al., "Microstructures and Mechanical Properties of H13 Tool Steel Fabricated by Selective Laser Melting," *Materials* 15, no. 7 (2022): 2686, https://doi.org/10.3390/ma15072686.

40. J. Platl, H. Leitner, C. Turk, A. G. Demir, B. Previtali, and R. Schnitzer, "Defects in a Laser Powder Bed Fused Tool Steel," *Advanced Engineering Materials* 23, no. 12 (2021): 2000833, https://doi.org/10.1002/adem.202000833.

1869344x, 2026, 10, Downloaded from https://onlinelibrary.wiley.com/doi/10.1002/srin.202501039 by Universitatsbibliothek RWTH Aachen University, Wiley Online Library on [05/11/2026]. See the Terms and Conditions (https://onlinelibrary.wiley.com/terms-and-conditions) on Wiley Online Library for rules of use; OA articles are governed by the applicable Creative Commons License

41. X. Peng, S. Wu, W. Qian, et al., "The Potency of Defects on Fatigue of Additively Manufactured Metals," *International Journal of Mechanical Sciences* 221 (2022): 107185, https://doi.org/10.1016/j.ijmecsci.2022.107185.

42. F. Weber, A. Würth, A. Wagner, et al., "Innovative Evaluation Methods for Accelerated Provision and Assessment of Fatigue Data Using Mathematical Methods," *International Journal of Fatigue* 203 (2026): 109350, https://doi.org/10.1016/j.ijfatigue.2025.109350.

43. F. Weber, A. Wagner, J. Koziol, F. Weber, C. Broeckmann, and P. Starke, "Consideration of Statistical Approaches Within the Accelerated Assessment of Fatigue Properties of Metallic Materials," *Metals* 15, no. 2 (2025): 191, https://doi.org/10.3390/met15020191.

44. F. Weber, F. Weber, T. Sedlatschek, A. Bezold, C. Broeckmann, and P. Starke, "Microstructure-Specific Lifetime Prediction Method for Heavy-Section Castings Based on Non-Destructive Measurements during Fatigue Testing," *International Journal of Metalcasting* (2025), https://doi.org/10.1007/s40962-025-01816-z.

45. F. Weber, J. A. Ziman, J. Koziol, S. R. Raghuraman, and P. Starke, "Use of NDT-Related Methods for a Response-Related Evaluation Regarding the Fatigue Behaviour of Metallic Materials," in Proceedings of the DGZfP Annual Conference 2025, Research and Review Journal of Nondestructive Testing/ReJNDT (2025), https://doi.org/10.58286/31940.

46. S. R. Raghuraman, J. A. Ziman, F. Weber, et al., "Fatigue Assessment of Quenched and Tempered Steels Based on Temperature and Micro-Magnetic Measurements," in Proceedings of the DGZfP Annual Conference 2025, Research and Review Journal of Nondestructive Testing/ReJNDT (2025), https://doi.org/10.58286/31938.

47. F. Weber, M. Maul, F. Juner, and P. Starke, "A Nonlinear Lifetime Prediction Method for Un- and Low-Alloyed Steels by Damage Determination Based on Non-Destructive Measurement Techniques," *Fatigue & Fracture of Engineering Materials & Structures* 47, no. 5 (2024): 1566–1583, https://doi.org/10.1111/ffe.14252.

48. F. Weber and P. Starke, "MiDAcLife – Ein neues Lebensdauerprognoseverfahren basierend auf der Kombination zerstörungsfreier Messverfahren und (nicht)linearer Schadensakkumulationsansätze," in Proceedings of the DGZfP Annual Conference 2024, Research and Review Journal of Nondestructive Testing/ReJNDT (2024), https://doi.org/10.58286/29499.

49. H. Wu, J. A. Ziman, S. R. Raghuraman, J.-E. Nebel, F. Weber, and P. Starke, "Short-Time Fatigue Life Estimation for Heat Treated Low Carbon Steels by Applying Electrical Resistance and Magnetic Barkhausen Noise," *Materials* 16, no. 1 (2023): 32, https://doi.org/10.3390/ma16010032.

50. F. Weber, J. Koziol, and P. Starke, "StressLife: A Short-Time Approach for the Determination of a Trend S–N Curve in and beyond the HCF Regime for the Steels 20MnMoNi5-5 and SAE 1045," *Materials* 16, no. 11 (2023): 3914, https://doi.org/10.3390/ma16113914.

51. J. Krummenacker and J. Hausmann, "Determination of Fatigue Damage Initiation in Short Fiber-Reinforced Thermoplastic through Acoustic Emission Analysis," *Journal of Composites Science* 5, no. 8 (2021): 221, https://doi.org/10.3390/jcs5080221.

52. A. Sorich, M. Smaga, and D. Eifler, "Fatigue Monitoring of Austenitic Steels with Electromagnetic Acoustic Transducers (EMATs)," *Materials Performance and Characterization* 4, no. 2 (2015): 263–274, https://doi.org/10.1520/MPC20140017.

53. I. Altpeter, R. Tschuncky, K. Hällen, et al., "Early Detection of Damage in Thermo-Cyclically Loaded Austenitic Materials," in *Electromagnetic Nondestructive Evaluation* Vol. 15 (IOS Press, 2012), https://doi.org/10.3233/978-1-60750-968-4-130.

54. P. Starke, F. Walther, and D. Eifler, "PHYBAL: A Short-Time Procedure for a Reliable Fatigue Life Calculation," *Advanced Engineering Materials* 12, no. 4 (2010): 276–282, https://doi.org/10.1002/adem.200900344.

55. J. H. Constable and C. Sahay, "Electrical Resistance as an Indicator of Fatigue," *IEEE Transactions on Components, Hybrids, and Manufacturing Technologies* 15, no. 6 (1992): 1138–1145, https://doi.org/10.1109/33.206940.

56. L. Gertlowski, O. Schenk, S. Müller, S. Benito, S. Weber, and C. Broeckmann, "Accelerated Fatigue Testing of High-Speed Steel," *Fatigue & Fracture of Engineering Materials & Structures* 49, no. 6 (2026): 2156–2166, https://doi.org/10.1111/ffe.70247.

57. H. Zhang, X. Zhang, D. A. Venero, et al., "Exploring the Tempering Behaviour of Additively Manufactured High-Alloy Tool Steel Using Synchrotron X-Ray and Neutron Techniques," *Additive Manufacturing* 123 (2026): 105219, https://doi.org/10.1016/j.addma.2026.105219.

58. F. Alvarez-Antolin and A. González-Pociño, "Effect of Heat Treatment on the Microstructure and Mechanical Properties of Vanadis 60 Steel: A Statistical Design Approach," *Solids* 6, no. 3 (2025): 46, https://doi.org/10.3390/solids6030046.

59. H. Zhang, H. Peng, P. A. J. Bagot, et al., "Insights into Primary Carbide and Nanoparticles in an Additively Manufactured High-Alloy Steel," *Acta Materialia* 270 (2024): 119834, https://doi.org/10.1016/j.actamat.2024.119834.

60. S. Karagöz, "Elektronenmikroskopische Untersuchung an Schnellarbeitsstählen: Einfluss des Gefüges auf die Zähigkeitseigenschaften sowie Einfluss von Niobzusätzen auf die Ausbildung und Zusammensetzung der Carbidphasen," (PhD thesis (doctoral diss.), Faculty of Materials Science, Montanuniversität Leoben, 1982), +Z298184806.

61. S. Karagöz, "Bildband (Anhang) – Elektronenmikroskopische Untersuchung an Schnellarbeitsstählen: Einfluss des Gefüges auf die Zähigkeitseigenschaften sowie Einfluss von Niobzusätzen auf die Ausbildung und Zusammensetzung der Carbidphasen," (PhD thesis (doctoral diss.), Faculty of Materials Science, Montanuniversität Leoben, 1982), +Z298184806.

62. W. Theisen, "Gefügebestandteile und -arten," in *Hartlegierungen und Hartverbundwerkstoffe – Gefüge, Eigenschaften, Bearbeitung, Anwendungen*, pub. H. Berns (Springer-Verlag Berlin, 1998), 27–39, https://doi.org/10.1007/978-3-642-51505-7.

63. J. Kleff, S. Franko, and M. Lührig, "Eigenschaften der Gefügebestandteile," in *Hartlegierungen und Hartverbundwerkstoffe – Gefüge, Eigenschaften, Bearbeitung, Anwendungen*, pub. H. Berns (Springer-Verlag Berlin, 1998), 53–69, https://doi.org/10.1007/978-3-642-51505-7.

64. C. Broeckmann, "Mechanische Eigenschaften," in *Hartlegierungen und Hartverbundwerkstoffe – Gefüge, Eigenschaften, Bearbeitung, Anwendungen*, pub. H. Berns (Springer-Verlag Berlin, 1998), 125–154, https://doi.org/10.1007/978-3-642-51505-7.

65. J. Lentz, "Werkstofftechnische Charakterisierung untereutektischer Legierungen im System Fe-C-B-X," (PhD thesis (doctoral diss.), Faculty of Mechanical Engineering, Ruhr-Universität Bochum, 2018), 978-3-943063-31-8.

66. P. Beiss, "Properties of Powder Metallurgy Tool Steels," in *ASM Handbook, Vol. 7: Powder Metallurgy*, 1st ed., eds. P. Samal and J. Newkirk (ASM International, 2015), 491–514, https://doi.org/10.31399/asm.hb.v07.a0006127.

67. P. Beiss, "Heat Treatment of Secondary-Hardening High-Alloy Tool Steels," in *ASM Handbook, Vol. 7: Powder Metallurgy*, 1st ed., eds. P. Samal and J. Newkirk (ASM International, 2015), 515–523, https://doi.org/10.31399/asm.hb.v07.a0006128.

68. P. Beiss, "Effects of Alloying on Powder Metallurgy Tool Steels," in *ASM Handbook, Vol. 7: Powder Metallurgy*, 1st ed., eds. P. Samal and J. Newkirk (ASM International, 2015), 524–529, https://doi.org/10.31399/asm.hb.v07.a0006129.

69. P. Beiss, "Chemical Composition of Powder Metallurgy High-Alloy Tool Steels," in *ASM Handbook, Vol. 7: Powder Metallurgy*, 1st ed.,

1869344x, 2026, 10, Downloaded from https://onlinelibrary.wiley.com/doi/10.1002/srin.202501039 by Universitatsbibliothek RWTH Aachen University, Wiley Online Library on [05/11/2026]. See the Terms and Conditions (https://onlinelibrary.wiley.com/terms-and-conditions) on Wiley Online Library for rules of use; OA articles are governed by the applicable Creative Commons License

eds. P. Samal and J. Newkirk (ASM International, 2015), 530–532, https://doi.org/10.31399/asm.hb.v07.a0006130.

70. P. Beiss, "Microstructure of Powder Metallurgy Tool Steels," in *ASM Handbook, Vol. 7: Powder Metallurgy*, 1st ed., eds. P. Samal and J. Newkirk (ASM International, 2015), 533–535, https://doi.org/10.31399/asm.hb.v07.a0006131.

71. C. R. Sohar, "Lifetime Controlling Defects in Tool Steels," (PhD thesis (doctoral diss.), Faculty of Technical Chemistry, Institute of Chemical Technologies and Analytics (CTA), Vienna University of Technology, 2011), https://doi.org/10.1007/978-3-642-21646-6.

72. C. R. Sohar, A. Betzwar-Kotas, C. Gierl, B. Weiss, and H. Danninger, "Influence of Surface Residual Stresses on Gigacycle Fatigue Response of High Chromium Cold Work Tool Steel," *Materials Science & Engineering Technology* 39, no. 3 (2008): 248–257, https://doi.org/10.1002/mawe.200700216.

73. C. R. Sohar, A. Betzwar-Kotas, C. Gierl, H. Danninger, and B. Weiss, "Gigacycle Fatigue Response of Tool Steels Produced by Powder Metallurgy Compared to Ingot Metallurgy Tool Steels," *International Journal of Materials Research* 101, no. 9 (2010): 1140–1150, https://doi.org/10.3139/146.110395.

74. C. R. Sohar, A. Betzwar-Kotas, C. Gierl, B. Weiss, and H. Danninger, "Anisotropy Effects on Gigacycle Fatigue Behaviour of High Cr Alloyed Cold Work Tool Steel," *Kovové Materiály–Metallic Materials* 46, no. 4 (2008): 197–207.

75. C. R. Sohar, A. Betzwar-Kotas, C. Gierl, B. Weiss, and H. Danninger, "Gigacycle Fatigue Fractography of Cold Work Tool Steels Produced by PM Compared to Ingot Metallurgy," *Powder Metallurgy Progress* 8, no. 3 (2008): 190–195.

76. C. R. Sohar, A. Betzwar-Kotas, C. Gierl, B. Weiss, and H. Danninger, "Gigacycle Fatigue Behavior of a High Chromium Alloyed Cold Work Tool Steel," *International Journal of Fatigue* 30, no. 7 (2008): 1137–1149, https://doi.org/10.1016/j.ijfatigue.2007.09.012.

77. C. R. Sohar, A. Betzwar-Kotas, C. Gierl, B. Weiss, and H. Danninger, "Fatigue Behaviour of M2 and M42 High Speed Steel up to the Gigacycle Regime," *Kovové Materiály–Metallic Materials* 47, no. 3 (2009): 147–158.

78. C. R. Sohar, A. Betzwar-Kotas, C. Gierl, B. Weiss, and H. Danninger, "Fractographic Evaluation of Gigacycle Fatigue Crack Nucleation and Propagation of a High Cr Alloyed Cold Work Tool Steel," *International Journal of Fatigue* 30, no. 12 (2008): 2191–2199, https://doi.org/10.1016/j.ijfatigue.2008.05.013.

79. C. R. Sohar, A. Betzwar-Kotas, C. Gierl, B. Weiss, and H. Danninger, "PM Tool Steels Push the Edge in Fatigue Tests," *Metal Powder Report* 64, no. 2 (2009): 12–17, https://doi.org/10.1016/S0026-0657(09)70013-X.

80. H. Danninger, C. R. Sohar, C. Gierl, A. Betzwar-Kotas, and B. Weiss, "Gigacycle Fatigue Response of PM versus Ingot Metallurgy Tool Steels," *Materials Science Forum* 672 (2011): 23–30, https://doi.org/10.4028/www.scientific.net/MSF.672.23.

81. German Institute for Standardization e. V. (DIN), Subcom. NA 021-00-19-04 UA, "DIN EN ISO 4957:2018-11 – Tool Steels," (DIN Media GmbH, 2018), https://doi.org/10.31030/2842661.

82. R. Rennert, E. Kullig, M. Vormwald, A. Esderts, and M. Luke, "FKM Guideline – Calculated Strength Verification for Machine Components Made of Steel, Cast Iron and Aluminum Materials," 7th ed., Forschungskuratorium Maschinenbau e. V. (FKM), (VDMA Verlag, 2020), 978-3-8163-0743-3.

83. R. Rennert, M. Vormwald, and A. Esderts, "FKM-Guideline "Analytical Strength Assessment" – Background and Current Developments," *International Journal of Fatigue* 182 (2024): 108165, https://doi.org/10.1016/j.ijfatigue.2024.108165.

84. U. Kletzin, R. Reich, M. Oechsner, A. Spies, and B. Pyttel, "FKM Guideline – Calculated Strength Verification for Springs and Spring Elements," 2nd ed., Forschungskuratorium Maschinenbau e. V. (FKM), (VDMA Verlag, 2023), 978-3-8163-0741-9.

85. ASTM International, Subcom. A01.29, "ASTM A681-24 – Standard Specification for Tool Steels Alloy," in *Book of Standards Vol. 01.05* (ASTM International, 2024), https://doi.org/10.1520/A0681-24.

86. H. Berns and W. Trojahn, "Einfluss der Wärmebehandlung auf das Ermüdungsverhalten ledeburitischer Kaltarbeitsstähle," *VDI-Zeitschrift* 127, no. 22 (1985): 889–892.

87. H. Berns, J. Lueg, W. Trojahn, R. Wähling, and H. Wisell, "The Fatigue Behaviour of Conventional and Powder Metallurgical High-Speed Steels," *Powder Metallurgy International* 19, no. 4 (1987): 22–26.

88. C. Broeckmann, A. Packeisen, and W. Theisen, "Fatigue of Carbide-Rich Materials," in Proceedings of the 7th International Tooling Conference, Vol. 1 (Associazione Italiana di Metallurgia, 2006), 3–12, 888-2020-19-3.

89. J. Bergström, C. Burman, V. Kazymyrovych, and J. Ekengren, "Fatigue Properties of Tool Steels – Particular Focus on Very High Cycle Fatigue," in Proceedings of the 9th International Tooling Conference (Austrian Society for Metallurgy and Materials, 2012), 349–355, 978-3-901-38452-3/-9.

90. L. M. Scholl, A. Bezold, and C. Broeckmann, "Toward the Application of Multiaxial Failure Criteria: Mean Stress Sensitivity of Carbide-Rich, High-Alloy PM-HIP Tool Steels Under Axial and Torsional Cyclic Loading," *Steel Research International* (2026): 2501036, https://doi.org/10.1002/srin.202501036.

91. L. M. Scholl, A. Bezold, and C. Broeckmann, "Influences of Manufacturing-Related Microstructural Variations on Fatigue in Carbide-Rich Tool Steels," *Steel Research International* 94, no. 4 (2023): 2200578, https://doi.org/10.1002/srin.202200578.

92. F. Javadzadeh Kalahroudi, D. Nikas, G. Maistro, and M. T. Grehk, "High Cycle Fatigue Properties of PM-HIPed High-Nitrogen Tool Steel: Effect of Surface Condition," *Fatigue & Fracture of Engineering Materials & Structures* 49, no. 6 (2026): 2097–2115, https://doi.org/10.1111/ffe.70238.

93. F. Javadzadeh Kalahroudi, F. Lin, P. Krakhmalev, and M. T. Grehk, "Microstructure and Fatigue Behavior of PM-HIPed Ni-Based Superalloys and Martensitic Tool Steels: A Review," *Metals* 14, no. 10 (2024): 1159, https://doi.org/10.3390/met14101159.

94. J. W. Pegues, M. D. Roach, and N. Shamsaei, "Additive Manufacturing of Fatigue Resistant Austenitic Stainless Steels by Understanding Process–Structure–Property Relationships," *Materials Research Letters* 8, no. 1 (2020): 8–15, https://doi.org/10.1080/21663831.2019.1678202.

95. S. Benito, J. Boes, M. Matsuo, S. Weber, and W. Theisen, "Uncovering Process–Structure Relationships Associated to the Hot Isostatic Pressing of the High-Speed Steel PMHS 3-3-4 through Novel Microstructural Characterization Methods," *Materials & Design* 208 (2021): 109925, https://doi.org/10.1016/j.matdes.2021.109925.

96. M. F. Garwood, H. H. Zurburg, and M. A. Erickson, "Correlation of Laboratory Tests and Service Performance," in *Interpretation of Tests and Correlation with Service* (ASM International, 1951), 1–77.

97. L. M. Scholl, A. Bezold, and C. Broeckmann, "Influences of Manufacturing-Related Microstructural Variations on Fatigue in Carbide-Rich Tool Steels," in Proceeding of the 12th International Tooling Conference (Austrian Society for Metallurgy and Materials, 2022), 244–252, 978-3-200-08359-2.

98. L. M. Scholl, A. Bezold, and C. Broeckmann, "Influence of Plasma Nitriding on the Fatigue Strength of Carbide-Rich Tool Steels," in Proceedings of the 12th International Tooling Conference (Austrian Society for Metallurgy and Materials, 2022), 368–376, 978-3-200-08359-2.

99. L. M. Scholl, F. Tegeder, A. Bezold, and C. Broeckmann, "Influence of Cleanliness, Carbide Size and Hardness on HCF Strength and Fatigue Mechanisms in Carbide-Rich Cold-Work Tool Steels," in Proceedings of the 13th International Tooling Conference (Austrian Society for Metallurgy and Materials, 2025), 179–194.

1869344x, 2026, 10, Downloaded from https://onlinelibrary.wiley.com/doi/10.1002/srin.202501039 by Universitatsbibliothek RWTH Aachen University, Wiley Online Library on [05/11/2026]. See the Terms and Conditions (https://onlinelibrary.wiley.com/terms-and-conditions) on Wiley Online Library for rules of use; OA articles are governed by the applicable Creative Commons License

100. L. M. Scholl, A. Bezold, and C. Broeckmann, "The Significance of Process Cleanliness and Carbide Structure for Fatigue Strength of Carbide-Rich PM-HIP Cold-Work Tool Steels," in Proceedings of the 14th International Conference on HIP (Technologie Marketing AG, 2025), 1–9.

101. M. Randelius, R. Sandström, and A. Melander, "Fatigue Strength of Conventionally Cast Tool Steels and Its Dependence of Carbide Microstructure," *Steel Research International* 83, no. 1 (2012): 83–90, https://doi.org/10.1002/srin.201100219.

102. K. Shimizu, Y. Tachi, Y. Haruna, S. Nichikawa, and N. Umano, "Characteristics of New Developed PM High-Speed Steel with High Toughness and Corrosion Resistance," in Proceedings of the 8th International Tooling Conference (Austrian Society for Metallurgy and Materials, 2009), 391–397, 978-3-8107930-58.

103. K. Shiozawa and T. Sakai, "Databook on Fatigue Strength of Metallic Materials," Vol. 1, The Society of Materials Science Japan (JSMS), (Elsevier, 1996), 0-444-82514-2.

104. K. Fukaura, Y. Yokoyama, D. Yokoi, N. Tsujii, and K. Ono, "Fatigue of Cold-Work Tool Steels: Effect of Heat Treatment and Carbide Morphology on Fatigue Crack Formation, Life, and Fracture Surface Observations," *Metallurgical and Materials Transactions A* 35 (2004): 1289–1300, https://doi.org/10.1007/s11661-004-0303-5.

105. Y. Natsume, T. Muramatsu, and T. Miyamoto, "Effect of Carbide Crack on Fatigue Strength of Alloy-Tool Steel Under Cold Working," *Proceedings of the Japan Society of Mechanical Engineers (JSME) Annual Conference* 900, no. 86 (1990): 323–325.

106. L. M. Scholl, F. Tegeder, A. Bezold, and C. Broeckmann, "Fatigue-Oriented Design of High-Strength Tools Made of Carbide-Rich PM Tool Steels Under Multiaxial Cyclic Loading," in Proceedings of the 6th European Steel Technology and Application Days (ESTAD) Conference (Technologie Marketing AG, 2023), 1–9.

107. L. M. Scholl, F. Tegeder, A. Bezold, and C. Broeckmann, "Mean Stress Sensitivity for Carbide-Rich PM Tool Steels Under Axial and Torsional Loading," in Proceedings of the 13th International Tooling Conference (Austrian Society for Metallurgy and Materials, 2025), 195–207.

108. L. M. Scholl, F. Tegeder, A. Bezold, and C. Broeckmann, "Influence of Carbide Size, Cleanliness and Hardness on the Fatigue Strength of Carbide-Rich Cold-Work Tool Steels," in Proceedings of the 41st DVM Tagung Werkstoffprüfung, pub. M. Wächter and J. Langer (DVM/DGM 2023), 86–93, https://doi.org/10.48447/WP-2023-261.

109. J. Yao, X. H. Qu, X. B. He, and L. Zhang, "Effect of Inclusion Size on the High Cycle Fatigue Strength and Failure Mode of a High V Alloyed Powder Metallurgy Tool Steel," *International Journal of Minerals, Metallurgy, and Materials* 19, no. 7 (2012): 608–614, https://doi.org/10.1007/s12613-012-0602-6.

110. J. Yao, X. H. Qu, X. B. He, and L. Zhang, "Fractographic Evaluation of High Cycle Fatigue Strength of a High V Alloyed Powder Metallurgy Tool Steel," *Powder Metallurgy* 55, no. 2 (2012): 95–100, https://doi.org/10.1179/1743290111Y.0000000024.

111. J. Yao, X. H. Qu, Rafi-ud-din, X. B. He, and L. Zhang, "Effect of Inclusion on High Cycle Fatigue Response of a Powder Metallurgy Tool Steel," *Journal of Central South University* 19 (2012): 1773–1779, https://doi.org/10.1007/s11771-012-1206-z.

112. J. Yao, X. H. Qu, X. B. He, and L. Zhang, "Inclusion-Controlled High Cycle Fatigue Behavior of a High V Alloyed Powder Metallurgy Cold-Working Tool Steel," *Material Science and Engineering: A* 528, no. 12 (2011): 4180–4186, https://doi.org/10.1016/j.msea.2011.02.016.

113. German Institute for Standardization e. V. (DIN), Subcom. NA 062-01-41 AA, "DIN EN ISO 18265:2014-02 – Metallic Materials – Conversion of Hardness Values," (DIN Media GmbH, 2014), https://doi.org/10.31030/2008740.

114. M. Luke, T. Straub, I. Varfolomeev, et al., "Methoden zur Berechnung der Schwingfestigkeit von Bauteilen aus höchstfesten Stählen," in Proceedings of the 8th Tagung Neue Entwicklungen für die Bauteilfestigkeitsnachweise (DVM/DGM, 2022), https://doi.org/10.48447/FKM-2022-006.

115. M. Luke, A. Kleemann, Y. Yadegari, et al., "Hochfeste Stähle – Entwicklung einer validierten Methodik zur Berechnung der Schwingfestigkeit von Bauteilen aus höchstfesten Stählen," 1st ed., Forschungskuratorium Maschinenbau e. V. (FKM), (VDMA Verlag, 2021), Report FKM-No. 610, booklet 340.

116. Y. Murakami, "Effects of Nonmetallic Inclusions on Fatigue Strength," in *Metal Fatigue: Effects of Small Defects and Nonmetallic Inclusions*, 2nd ed., pub. M. Deans (Academic Press/Elsevier Limited, 2019), 95–150, https://doi.org/10.1016/B978-0-12-813876-2.00006-6.

117. L. M. Scholl, A. Bezold, and C. Broeckmann, "Development of a Hardness- and Microstructure-Dependent Correlation of Quasi-Static and Fatigue Strength of Carbide-Rich High-Speed Steels," in Proceedings of the 41st DVM Tagung Werkstoffprüfung, pub. M. Wächter and J. Langer (DVM/DGM, 2023), 204–211, https://doi.org/10.48447/WP-2023-262.

118. Y. Murakami, "Metal Fatigue: Effects of Small Defects and Nonmetallic Inclusions," 2nd ed., pub. M. Deans (Academic Press/Elsevier Limited, 2019), 978-0-12-813876-2.

119. Y. Murakami and T. Endo, "The Effects of Small Defects on the Fatigue Strength of Hard Steels," in Proceedings of the International Fatigue Congress (Fatigue '81), eds. F. Sherrat and J. B. Sturgeon (Westbury House/IPC Science and Technology Press, 1981), 431–440.

120. I. Picas, N. Cuadrado, D. Casellas, A. Goez, and L. Llanes, "Microstructural Effects on the Fatigue Crack Nucleation in Cold Work Tool Steels," *Procedia Engineering* 2, no. 1 (2010): 1777–1785, https://doi.org/10.1016/j.proeng.2010.03.191.

121. U. Zerbst, M. Madia, C. Klinger, B. Bettge, and Y. Murakami, "Defects as a Root cause of Fatigue Failure of Metallic Components. I: Basic Aspects," *Engineering Failure Analysis* 97 (2019): 777–792, https://doi.org/10.1016/j.engfailanal.2019.01.055.

122. U. Zerbst, M. Madia, C. Klinger, B. Bettge, and Y. Murakami, "Defects as a Root cause of Fatigue Failure of Metallic Components. II: Non-Metallic Inclusions," *Engineering Failure Analysis* 98 (2019): 228–239, https://doi.org/10.1016/j.engfailanal.2019.01.054.

123. U. Zerbst, M. Madia, C. Klinger, B. Bettge, and Y. Murakami, "Defects as a Root cause of Fatigue Failure of Metallic Components. III: Cavities, Dents, Corrosion Pits, Scratches," *Engineering Failure Analysis* 97 (2019): 759–776, https://doi.org/10.1016/j.engfailanal.2019.01.034.

124. U. Zerbst, M. Madia, G. Bruno, and K. Hilgenberg, "Towards a Methodology for Component Design of Metallic AM Parts Subjected to Cyclic Loading," *Metals* 11, no. 5 (2021): 709, https://doi.org/10.3390/met11050709.

125. A. Mayerhofer, "Enhanced Characterization of Non-Metallic Inclusions for (sub)Micro steel Cleanness Evaluations," (PhD thesis (doctoral diss.), Faculty of Materials Science, Chair of Ferrous Metallurgy, Montanuniversität Leoben, 2021).

126. V. Kazymyrovych, "Very High Cycle Fatigue of Tool Steels," (PhD thesis (doctoral diss.), Faculty of Technology and Science, Department of Materials Engineering, Karlstad University, 2010), 978-91-7063-312-6.

127. K. Chantziara, J. Bergström, D. Nikas, and M. T. Grehk, "Microstructure, Defects and Fatigue Response of High Strength Tool Steels," in Proceedings of the 13th International Tooling Conference (Austrian Society for Metallurgy and Materials, 2025), 208–217.

128. K. Chantziara, J. Bergström, D. Nikas, and M. T. Grehk, "Microstructure, Defects and Fatigue Response of High Strength Tool Steels," *Steel Research International* (2026): 2500730, https://doi.org/10.1002/srin.202500730.

129. M. L. Scheck, "Legierungsentwicklung von karbidreichen Werkzeugstählen aus Pulvermischungen für die laser- und

1869344x, 2026, 10, Downloaded from https://onlinelibrary.wiley.com/doi/10.1002/srin.202501039 by Universitatsbibliothek RWTH Aachen University, Wiley Online Library on [05/11/2026]. See the Terms and Conditions (https://onlinelibrary.wiley.com/terms-and-conditions) on Wiley Online Library for rules of use; OA articles are governed by the applicable Creative Commons License

pulverbettbasierte additive Fertigung," (PhD thesis (doctoral diss.), Faculty of Mechanical Engineering, RWTH Aachen University, 2025).

130. M. L. Scheck, M. Norda, S. Herzog, A. Kaletsch, F. Petzoldt, and C. Broeckmann, "Particle-Reinforced Tool Steels Through Powder Additivation in Laser-Based Powder Bed Fusion," in Proceedings of the Euro PM2023 Congress & Exhibition (European Powder Metallurgy Association, 2024), https://doi.org/10.59499/EP235764739.

131. M. L. Köhler, M. Norda, S. Herzog, A. Kaletsch, F. Petzoldt, and C. Broeckmann, "Towards Carbide-Rich Tool Steels in PBF-LB/M: TiC Additivation of AISI H13," *Additive Manufacturing Letters* 6 (2023): 100143, https://doi.org/10.1016/j.addlet.2023.100143.

132. M. L. Köhler, F. Ali, S. Herzog, P. Suwanpinij, A. Kaletsch, and C. Broeckmann, "Influence of Cr_3C_2 Additions to AISI H13 Tool Steel in the LPBF Process," *Steel Research International* 93, no. 1 (2022): 2100454, https://doi.org/10.1002/srin.202100454.

133. M. L. Köhler, F. Radtke, M. Norda, et al., "Resistance against Abrasive Wear and Corrosion of Laser Powder Bed Alloyed High Chromium Tool Steels," *Steel Research International* 94, no. 4 (2023): 2200455, https://doi.org/10.1002/srin.202200455.

134. F. Meyer, F. Kolodzy, M. L. Scheck, et al., "Novel Pectin Binder for Satelliting Carbides to H13 Tool Steel for PBF-LP Processing," *Materials* 16, no. 10 (2023): 3649, https://doi.org/10.3390/ma16103649.

135. O. Bürgi, A. Kaletsch, and C. Broeckmann, "In Situ Alloying of H13 Tool Steel with TiC via PBF-LB/M," *Steel Research International* (2026): 202500659, https://doi.org/10.1002/srin.202500659.

136. G. Parrish, "Carburizing: Microstructures and Properties," 1st ed., (ASM International, 1999), 978-1-61503-222-8.

137. G. Parrish, "The Influence of Microstructure on the Properties of Case-Carburised Components – Part 6: Core Properties and Case Depth," *Journal Heat Treatment of Metals* 2 (1977): 45–54.

138. G. Parrish, "The Influence of Microstructure on the Properties of Case-Carburised Components – Part 8: Post Hardening Treatments – Mechanical," *Journal Heat Treatment of Metals* 4 (1977): 107–116.

139. A. Randak, A. Stanz, and W. Verderber, "Eigenschaften Von Nach Sonderschmelzverfahren Hergestellten Werkzeug- Und Wälzlagerstählen," *Stahl & Eisen* 92, no. 20 (1972): 981–993.

140. S. Marsoner, R. Ebner, W. Liebfahrt, and F. Jeglitsch, "Fatigue Properties of High-Strength Ledeburitic PM Tool Steels," *HTM Journal of Heat Treatment and Materials* 57, no. 4 (2002): 283–289.

141. H. Berns, original author, "Schematic σ_B–d–HV Relationship for the Quasi-Static Bending Strength of Hard, Defective Steels," Unpublished Lecture and Teaching Materials, Chair of Materials Technology (LWT), Faculty of Mechanical Engineering (Ruhr-Universität Bochum, 1998).

142. German Institute for Standardization e. V. (DIN), Subcom. NA 062-01-31 GA, "DIN EN 10247:2017-09 – Micrographic Examination of the Non-Metallic Inclusion Content of Steels Using Standard Pictures," (DIN Media GmbH, 2017), https://doi.org/10.31030/2690587.

143. Japanese Industrial Standards Committee (JIS), Technical Committee on Metal and Inorganic Materials, "JIS G 0555:2023-08-21 – Microscopic Testing Method for the Non-Metallic Inclusions in Steel" Japanese Standards Association, 2023, 77.040.99/77.080.20.

144. ASTM International, Subcom. E04.09, "ASTM E45-25 – Standard Test Methods for Determining the Inclusion Content of Steel," in *Book of Standards Vol. 03.01* (ASTM International, 2025), https://doi.org/10.1520/E0045-25.

145. ASTM International, Subcom. E04.11, "ASTM E2142-08R23 – Standard Test Methods for Rating and Classifying Inclusions in Steel Using the Scanning Electron Microscope," in *Book of Standards Vol. 03.01* (ASTM International, originally 2008/reapproved 2023), https://doi.org/10.1520/E2142-08R23.

146. ASTM International, Subcom. E04.09, "ASTM E2283-08R19 – Standard Practice for Extreme Value Analysis of Nonmetallic Inclusions in Steel and Other Microstructural Features," in *Book of Standards Vol. 03.01* (ASTM International, originally 2008/reapproved 2019), https://doi.org/10.1520/E2283-08R19.

147. S. Marsoner, R. Ebner, and W. Liebfahrt, "Influence of Inclusion Content and Residual Stresses on S-N Curves of PM Tool Steels," *BHM Berg- Und hüttenmännische Monatshefte* 148, no. 5 (2003): 176–181.

148. S. Caruso, D. Umbrello, J. C. Outeiro, L. Filice, and F. Micari, "An Experimental Investigation of Residual Stresses in Hard Machining of AISI 52100 Steel," *Procedia Engineering* 19 (2011): 67–72, https://doi.org/10.1016/j.proeng.2011.11.081.

149. W. Jomaa, V. Songmene, and P. Bocher, "An Investigation of Machining-Induced Residual Stresses and Microstructure of Induction-Hardened AISI 4340 Steel," *Materials and Manufacturing Processes* 31, no. 7 (2016): 838–844, https://doi.org/10.1080/10426914.2015.1070431.

150. J. C. Outeiro, "Residual Stresses in Machining," in *Mechanics of Materials in Modern Manufacturing Methods and Processing Techniques*, ed. V. V. Silberschmidt and pub. M. Deans (Elsevier Ltd., 2020), 297–360, 978-0-12-818232-1, https://doi.org/10.1016/B978-0-12-818232-1.00011-4.

151. German Institute for Standardization e. V. (DIN), Subcom. NA 023-05-20 AA, "DIN EN 15305:2009-01 – Non-Destructive Testing – Test Method for Residual Stress Analysis by X-Ray Diffraction," (DIN Media GmbH, 2009), https://doi.org/10.31030/1425472.

152. German Institute for Standardization e. V. (DIN), Subcom. NA 062-01-45 AA, "DIN 50113:2018-12 – Testing of Metallic Materials – Rotating Bar Bending Fatigue Test," (DIN Media GmbH, 2018), https://dx.doi.org/10.31030/2874331.

153. German Institute for Standardization e. V. (DIN), Subcom. NA 062-01-45 AA, "DIN 50100:2022-12 – Load Controlled Fatigue Testing – Execution and Evaluation of Cyclic Tests at Constant Load Amplitudes on Metallic Specimens and Components," (DIN Media GmbH, 2022), https://dx.doi.org/10.31030/3337109.

154. F. Klubberg, M. Hempen, and P. Beiss, "Statistically Evaluated Fatigue Tests – Possible Applications of the PC Software SAFD – Statistical Analysis of Fatigue Data," *Materials Testing* 41 (1999): 362–367.

155. E. Rossow, "Eine Einfache Rechenschiebernäherung," *Zeitschrift für Wirtschaftlichen Fabrikbetrieb* 59, no. 12 (1964): 596–600, https://doi.org/10.1515/zwf-1964-591212.

156. S. Beretta and Y. Murakami, "Statistical Analysis of Defects for Fatigue Strength Prediction and Quality Control of Materials," *Fatigue & Fracture of Engineering Materials & Structures* 21, no. 9 (1998): 1049–1065, https://doi.org/10.1046/j.1460-2695.1998.00104.x.

157. S. Beretta and S. Romano, "A Comparison of Fatigue Strength Sensitivity to Defects for Materials Manufactured by AM or Traditional Processes," *International Journal of Fatigue* 94, no. 2 (2017): 178–191, https://doi.org/10.1016/j.ijfatigue.2016.06.020.

158. S. Beretta, "More than 25 years of Extreme Value Statistics for Defects: Fundamentals, Historical Developments, Recent Applications," *International Journal of Fatigue* 151 (2021): 106407, https://doi.org/10.1016/j.ijfatigue.2021.106407.

159. S. Beretta, L. Patriarca, M. Gargourimotlagh, et al., "A Benchmark Activity on the Fatigue Life Assessment of AlSi10Mg Components Manufactured by L-PBF," *Materials & Design* 218 (2022): 110713, https://doi.org/10.1016/j.matdes.2022.110713.

160. Y. Murakami, "Inclusion Rating by Statistics of Extreme Values and Its Application to Fatigue Strength Prediction and Quality Control of Materials," *Journal of Research of the National Institute of Standards and Technology* 99, no. 4 (1994): 345–351, https://doi.org/10.6028/jres.099.032.

1869344x, 2026, 10, Downloaded from https://onlinelibrary.wiley.com/doi/10.1002/srin.202501039 by Universitatsbibliothek RWTH Aachen University, Wiley Online Library on [05/11/2026]. See the Terms and Conditions (https://onlinelibrary.wiley.com/terms-and-conditions) on Wiley Online Library for rules of use; OA articles are governed by the applicable Creative Commons License

161. Y. Murakami, "Material Defects as the Basis of Fatigue Design," *International Journal of Fatigue* 41 (2012): 2–10, https://doi.org/10.1016/j.ijfatigue.2011.12.001.

162. Y. Murakami and Y. Yamashita, "Prediction of Life and Scatter of Fatigue Failure Originated at Nonmetallic Inclusions," *Procedia Engineering* 74 (2014): 6–11, ICMFM17, https://doi.org/10.1016/j.proeng.2014.06.214.

163. Y. Yamashita and Y. Murakami, "Small Crack Growth Model from Low to Very High Cycle Fatigue Regime for Internal Fatigue Failure of High Strength Steel," *International Journal of Fatigue* 93, no. 2 (2016): 406–414, https://doi.org/10.1016/j.ijfatigue.2016.04.016.

164. Y. Murakami, H. Masuo, Y. Tanaka, and M. Nakatani, "Defect Analysis for Additively Manufactured Materials in Fatigue from the Viewpoint of Quality Control and Statistics of Extremes," *Procedia Structural Integrity* 19 (2019): 113–122, Fatigue Design 2019, https://doi.org/10.1016/j.prostr.2019.12.014.

165. Y. Murakami, T. Takagi, K. Wada, and H. Matsunaga, "Essential Structure of S-N Curve: Prediction of Fatigue Life and Fatigue Limit of Defective Materials and Nature of Scatter," *International Journal of Fatigue* 146 (2021): 106138, https://doi.org/10.1016/j.ijfatigue.2020.106138.

166. J. Ekengren and J. Bergström, "Detecting Large Inclusions in Steels: Evaluating Methods," *Steel Research International* 80, no. 11 (2009): 854–858, https://doi.org/10.2374/SRI09SP079.

167. J. Ekengren and J. Bergström, "Extreme Value Distributions of Inclusions in Six Steels," *Extremes* 15 (2012): 257–265, https://doi.org/10.1007/s10687-011-0139-5.

168. B. M. Schönbauer, S. Gosh, U. Karr, et al., "Mean-Stress Sensitivity of an Ultrahigh-Strength Steel Under Uniaxial and Torsional High and Very High Cycle Fatigue Loading," *Fatigue & Fracture of Engineering Materials & Structures* 45, no. 11 (2022): 3361–3377, https://doi.org/10.1111/ffe.13767.

169. B. M. Schönbauer, S. Gosh, J. Kömi, T. Frondelius, and H. Mayer, "Influence of Small Defects and Nonmetallic Inclusions on the High and Very High Cycle Fatigue Strength of an Ultrahigh-Strength Steel," *Fatigue & Fracture of Engineering Materials & Structures* 44, no. 11 (2021): 2990–3007, https://doi.org/10.1111/ffe.13534.

170. B. M. Schönbauer and H. Mayer, "Effect of Small Defects on the Fatigue Strength of Martensitic Stainless Steels," *International Journal of Fatigue* 127 (2019): 362–375, https://doi.org/10.1016/j.ijfatigue.2019.06.021.

171. B. M. Schönbauer, K. Yanase, and M. Endo, "Influences of Small Defects on Torsional Fatigue Limit of 17-4PH Stainless Steel," *International Journal of Fatigue* 100 (2017): 540–548, https://doi.org/10.1016/j.ijfatigue.2016.12.021.

172. S. Beretta, "Application of Multiaxial Fatigue Criteria to Materials Containing Defects," *Fatigue & Fracture of Engineering Materials & Structures* 26, no. 6 (2003): 551–559, https://doi.org/10.1046/j.1460-2695.2003.00666.x.

173. T. Tomaszewski and J. Papuga, "Predicting the Size-Dependent Fatigue Strength Distributions in Additively Manufactured AlSi10Mg Alloy Specimens Using Extreme Value Statistics," *Fatigue & Fracture of Engineering Materials & Structures* 49, no. 8 (2026): 3198–3217, https://doi.org/10.1111/ffe.70310.

174. M. Sepati, G. Minerva, L. Patriarca, et al., "Experience of Defect Tolerant Design for Additively Manufactured Components in High Performance Cars," *Procedia Structural Integrity* 76 (2026): 138–144, https://doi.org/10.1016/j.prostr.2025.12.297.

175. L. Buiter, A. Yadollahi, and J. C. Newman Jr., "Fatigue-Life Prediction of Additively Manufactured Material: Effects of Defect Spacing and Multi-Site Damage," *Fatigue & Fracture of Engineering Materials & Structures* 48, no. 11 (2025): 4860–4878, https://doi.org/10.1111/ffe.70067.

176. K. Shiozawa, Y. Morii, S. Nishino, and L. Lu, "Subsurface Crack Initiation and Propagation Mechanism in High-Strength Steel in a Very High Cycle Fatigue Regime," *International Journal of Fatigue* 28, no. 11 (2006): 1521–1532, https://doi.org/10.1016/j.ijfatigue.2005.08.015.

177. K. Shiozawa, Y. Shimatani, T. Nakada, T. Yoshimoto, and M. Koshi, "Very High Cycle Fatigue Properties of High-Speed Steel Developed by Basis on Internal Failure Mechanism," *Transactions of the Japan Society of Mechanical Engineers (JSME) A* 76, no. 772 (2010): 1689–1697.

178. L. Lu and K. Shiozawa, "Effect of Surface Treatment on Super-Long-Life Fatigue Behavior in High-Speed Tool Steel JIS SKH51," *Transactions of the Japan Society of Mechanical Engineers (JSME) A* 69, no. 684 (2003): 1195–1202.

179. K. Shiozawa and L. Lu, "Very High Cycle Fatigue Behaviour of Shot-Peened High-Carbon-Chromium Bearing Steel," *Fatigue & Fracture of Engineering Materials & Structures* 25, no. 8-9 (2002): 813–822, https://doi.org/10.1046/j.1460-2695.2002.00567.x.

180. K. Shiozawa and L. Lu, "Internal Fatigue Failure Mechanism of High Strength Steels in Gigacycle Regime," *Key Engineering Materials* 378-379 (2008): 65–80, https://doi.org/10.4028/www.scientific.net/kem.378-379.65.

181. W. Li, H. Deng, Z. Sun, Z. Zhang, L. Lu, and T. Sakai, "Subsurface Inclusion-Induced Crack Nucleation and Growth Behaviors of High Strength Steels Under Very High Cycle Fatigue: Characterization and Microstructure-Based Modeling," *Materials Science & Engineering: A* 641 (2015): 10–20, https://doi.org/10.1016/j.msea.2015.06.037.

182. T. Makino, "The Effect of Inclusion Geometry According to Forging Ratio and Metal Flow Direction on Very-High-Cycle Fatigue Properties of Steel Bars," *International Journal of Fatigue* 30, no. 8 (2008): 1409–1418, https://doi.org/10.1016/j.ijfatigue.2007.10.009.

183. A. L. Vasconcellos da Costa e Silva, "The Effects of Non-Metallic Inclusions on Properties Relevant to the Performance of Steel in Structural and Mechanical Applications," *Journal of Materials Research and Technology* 8, no. 2 (2019): 2408–2422, https://doi.org/10.1016/j.jmrt.2019.01.009.

184. B. Sammer, K. Thiele, S. Ilie, R. Rössler, H. Kreuzer, and S. K. Michelic, "Evolution of Non-Metallic Inclusions in Non-Oriented Electrical Steel: Industrial Observations and Laboratory Test Results," *Metallurgical Research & Technology* 123, no. 2 (2026): 207, https://doi.org/10.1051/metal/2025146.

185. R. Musi, M. Schickbichler, M. Burtscher, S. K. Michelic, and K. Thiele, "Steel Cleanliness Evaluation: Framework for Inclusion Characterization by Means of Automated and Manual SEM/EDS Analysis and Computational Thermodynamics," *The Iron and Steel Institute of Japan (ISIJ) International* 65, no. 13 (2025): 2213–2225, https://doi.org/10.2355/isijinternational.ISIJINT-2025-260.

186. C. Truschner, K. Thiele, S. Ilie, R. Rössler, A. Jungreithmeier, and S. K. Michelic, "Tracing of Deoxidation Products in Ti-Stabilized Interstitial Free Steels by La and Ce on an Industrial and Laboratory Scale," *Steel Research International* 95, no. 3 (2024): 2300665, https://doi.org/10.1002/srin.202300665.

187. M. Schickbichler, K. Thiele, and S. K. Michelic, "Evaluation of Differences between Sequential Chemical and Electrolytical Extraction of Rare Earth (RE)-Containing Inclusions," *BHM Berg- und Hüttenmännische Monatshefte* 169, no. 3 (2024): 119–123, https://doi.org/10.1007/s00501-024-01435-x.

188. K. Thiele, S. Wagner, J. Irrgeher, T. Prohaska, and S. K. Michelic, "Tracing Non-Metallic Inclusions in Steel with Low Levels of Enriched Magnesium Stable Isotopes: A Novel Approach," *Materials Characterization* 221 (2025): 114759, https://doi.org/10.1016/j.matchar.2025.114759.

189. K. Thiele, S. Ilie, R. Roessler, et al., "Different Approaches to Trace the Source of Non-Metallic Inclusions in Steel," *Association for Iron &*

1869344x, 2026, 10, Downloaded from https://onlinelibrary.wiley.com/doi/10.1002/srin.202501039 by Universitatsbibliothek RWTH Aachen University, Wiley Online Library on [05/11/2026]. See the Terms and Conditions (https://onlinelibrary.wiley.com/terms-and-conditions) on Wiley Online Library for rules of use; OA articles are governed by the applicable Creative Commons License

Steel Technology (AIST) Transactions, Iron & Steel Technology 20, no. 7 (2023): 132–138, https://doi.org/10.33313/TR/0723.

190. K. Thiele, R. Musi, S. R. Babu, and S. K. Michelic, "Optimization of the Two- and Three-Dimensional Characterization of Rare Earth-Traced Deoxidation Products," *Advanced Engineering Materials* 25, no. 11 (2023): 2201748, https://doi.org/10.1002/adem.202201748.

191. K. Thiele, "Tracing of Non-Metallic Inclusions in Steel by Applying Modern Analytical Techniques," (PhD thesis (doctoral diss.), Faculty of Materials Science, Chair of Ferrous Metallurgy, Montanuniversität Leoben, 2024).

192. M. D. Chapetti, T. Tagawa, and T. T. Miyata, "Ultra-Long Cycle Fatigue of High-Strength Carbon Steels Part II: Estimation of Fatigue Limit for Failure from Internal Inclusions," *Materials Science and Engineering: A* 356, no. 1-2 (2003): 236–244, https://doi.org/10.1016/S0921-5093(03)00136-9.

193. H. Kitagawa and S. Takahashi, "Applicability of Fracture Mechanics to Very Small Cracks or the Cracks in the Early Stage," in Proceedings of the 2nd International Conference on Mechanical Behavior of Materials (ASM International, 1976), 627–631.

194. T. Hirano, Y. Shimatani, K. Shiozawa, T. Yoshimoto, and M. Koshi, "Effect of Nitriding on Very High Cycle Fatigue Properties of Developed High Speed Steel," *Transactions of the Japan Society of Mechanical Engineers (JSME) A* 77, no. 775 (2011): 427–437.

195. G. H. Farrahi and H. Ghadbeigi, "An Investigation into the Effect of Various Surface Treatments on Fatigue Life of a Tool Steel," *Journal of Materials Processing Technology* 174, no. 1–3 (2006): 318–324, https://doi.org/10.1016/j.jmatprotec.2006.01.014.

196. Y. Shimatani, K. Shiozawa, T. Nakada, and T. Yoshimoto, "Effect of Surface Residual Stress and Inclusion Size on Very High Cycle Fatigue Properties of High-Speed Tool Steel," *Transactions of the Japan Society of Mechanical Engineers (JSME) A* 75, no. 759 (2009): 1598–1607.

197. Y. Shimatani, K. Shiozawa, T. Nakada, and T. Yoshimoto, "Effect of Surface Residual Stress and Inclusion Size on Fatigue Failure Mode of Matrix HSS in Very High Cycle Regime," *Procedia Engineering* 2, no. 1 (2010): 873–882, https://doi.org/10.1016/j.proeng.2010.03.094.

198. Y. Shimatani, K. Shiozawa, T. Nakada, T. Yoshimoto, and L. Lu, "The Effect of the Residual Stresses Generated by Surface Finishing Methods on the Very High Cycle Fatigue Behavior of Matrix HSS," *International Journal of Fatigue* 33, no. 2 (2011): 122–131, https://doi.org/10.1016/j.ijfatigue.2010.07.009.

199. Y. Harada, K. Fukauara, and S. Kohamada, "Effects of Microshot Peening on Surface Characteristics of High-Speed Tool Steel," *Journal of Materials Processing Technology* 201, no. 1–3 (2008): 319–324, https://doi.org/10.1016/j.jmatprotec.2007.11.247.

200. F. Meurling, A. Melander, M. Tidesten, and L. Westin, "Influence of Carbide and Inclusion Contents on the Fatigue Properties of High-Speed Steels and Tool Steels," *International Journal of Fatigue* 23, no. 3 (2001): 215–224, https://doi.org/10.1016/S0142-1123(00)00087-6.

201. F. Meurling, "Influence of Carbide Distribution, Inclusion Content and Surface Machining Processes on the Fatigue Properties of Powder Metallurgically Produced High-Speed Steels and Tool Steels for Cold Work Applications," Report IM-1999-017 (Swedish Institute for Metals Research/Institutet för Metallforskning, 1999).

202. H. Wiegand and G. Tolasch, "Dauerfestigkeitsverhalten einsatzgehärteter Proben," *HTM Härterei-Technische Mitteilungen* 22, no. 4 (1967): 330–338.

203. T. Alatarvas, T. Antola, and T. Fabritius, "Utilizing Inclusion Data in Characterization of Oxide-Sulfide Stringers in Hot-Rolled Plates," *IOP Conference Series: Materials Science and Engineering* 529 (2019): 012066, https://doi.org/10.1088/1757-899X/529/1/012066.

204. Y. Yang, D. Zhan, G. Qiu, X. Li, Z. Jiang, and H. Zhang, "Inclusion Evolution in Solid Steel during Rolling Deformation: A Review," *Journal of Materials Research and Technology* 18 (2022): 5103–5115, https://doi.org/10.1016/j.jmrt.2022.05.018.

205. M. A. Wollenweber, T. Reclik, C. Reinhart, et al., "Ductile Damage at MnS Inclusions in 16MnCrS5 Steel - Influence of the Phase Environment," *Materials Science & Engineering: A* 965 (2026): 150251, https://doi.org/10.1016/j.msea.2026.150251.

206. S. Sundin and N. Reis, "Effect of Cleanliness on Fatigue Resistance of PM-HSS," in Proceedings of the 12th International Tooling Conference (Austrian Society for Metallurgy and Materials, 2022), 185–192.

207. A. Chychko, N. Reis, S. Sundin, J. André, V. Sehlstedt, and J. Siljamäki, "Investigation of Large Rare Inclusions with Combination of Ultrasonic and Fatigue Tests," in Proceedings of the 10th International Conference on Clean Steel (Hungarian Mining and Metallurgical Society/OMBKE, 2018), 1–6.

208. Y. Furuya, "A New Model for Predicting the Gigacycle Fatigue Strength of High-Strength Steels," *Materials Science & Engineering: A* 743 (2019): 445–452, https://doi.org/10.1016/j.msea.2018.11.109.

209. Y. Furuya, H. Hirukawa, and E. Takeuchi, "Gigacycle Fatigue in High Strength Steels," *Science and Technology of Advanced Materials (STAM)* 20, no. 1 (2019): 643–656, https://doi.org/10.1080/14686996.2019.1610904.

210. Y. Furuya, "10^{11} Gigacycle Fatigue Properties of High-Strength Steels," *The Iron and Steel Institute of Japan (ISIJ) International* 61, no. 1 (2021): 396–400, https://doi.org/10.2355/isijinternational.ISIJINT-2020-212.

211. L. Rusnati, G. Minerva, L. Patriarca, S. Miccoli, and S. Beretta, "Comparison of Methods for the Determination of Fatigue Critical Flaw Size and Implementation for Probabilistic Fatigue Assessment," *International Journal of Fatigue* 203 (2026): 109252, https://doi.org/10.1016/j.ijfatigue.2025.109252.

212. S. Fliegener, J. Rosenberger, M. Luke, et al., "Digital Methods for the Fatigue Assessment of Engineering Steels," *Advanced Engineering Materials* 27, no. 8 (2025): 2400992, https://doi.org/10.1002/adem.202400992.

213. T. Hajeck, K. Burkamp, P. Beiss, A. Bezold, and C. Broeckmann, "Synthetic S–N Curves for Sintered Steels Based on Density, Hardness, and Local Stress Parameters: A Data Analysis," *Powder Metallurgy* (2026), https://doi.org/10.1177/00325899261442076.

214. R. Motte and W. de Waele, "An Overview of Estimations for the High-Cycle Fatigue Strength of Conventionally Manufactured Steels Based on Other Mechanical Properties," *Metals* 14, no. 1 (2024): 85, https://doi.org/10.3390/met14010085.

215. P. Yadegari, H. T. Beier, M. Vormwald, and A. Kleemann, "Estimation of the Fatigue Strength of Ultra-High Strength Steels," *Procedia Structural Integrity* 37 (2022): 500–507, https://doi.org/10.1016/j.prostr.2022.01.115.

216. B. Torries, A. Imandoust, S. Beretta, S. Shao, and N. Shamsaei, "Overview of Microstructure- and Defect-Sensitive Fatigue Modeling of Additively Manufactured Materials," *JOM The Journal of the Minerals, Metals & Materials Society (TMS)* 70 (2018): 1853–1862, https://doi.org/10.1007/s11837-018-2987-9.

217. N. Gubeljak, J. Predan, B. Senčič, and M. D. Chapetti, "Effect of Residual Stresses and Inclusion Size on Fatigue Resistance of Parabolic Steel Springs," *Materials Testing* 56, no. 4 (2014): 312–317, https://doi.org/10.3139/120.110567.

Supporting Information

Additional supporting information can be found online in the Supporting Information section.

1869344x, 2026, 10, Downloaded from https://onlinelibrary.wiley.com/doi/10.1002/srin.202501039 by Universitatsbibliothek RWTH Aachen University, Wiley Online Library on [05/11/2026]. See the Terms and Conditions (https://onlinelibrary.wiley.com/terms-and-conditions) on Wiley Online Library for rules of use; OA articles are governed by the applicable Creative Commons License